Study of Multihadronic Events Using Decay Electrons

A DISSERTATION

Presented in Partial Fulfillment of Requirements
for the Degree of Doctor of Philosophy
in the Graduate School of Osaka University

Nobuyuki Kanda
Osaka University

1993

Marke

Den unerforschlich tief geheimnisvollen Grund, wer macht der Welt ihn kund?

ああ、計り知れない深さの神秘な淵の底を

世に暴いて見せるとは、それはいったい、誰の仕業だ。

TRISTAN

O König, das kann ich dir nicht sagen;

王よ、それにはお答えいたしかねます。

und was du frägst, das kannst du nie erfahren.

しかしお尋ねのことは、他の誰からもやはりお聞きにはなれますまい。

from *'TRISTAN und ISOLDE'* (Act II scene 3) by Richard Wagner

Abstract

We have studied heavy quark (b,c) productions in e^+e^- annihilation using decay electrons from them.

Electron identification in multi-hadronic events has been made successfully with upgraded VENUS detector, which was equipped with a transiton radiation detector (TRD) in 1991. Obtained hadron reduction with TRD and a lead glass calorimeter (LG) is estimated to be $\sim 10^{-3}$ at 70% detection efficiency of the electron.

The cross section, charge asymmetry of pair production of b and c quarks have been measured from the study of prompt electrons. Results agree well with standard model predictions. Our measured values are as follows.

cross section;

$$\sigma_b = 15.4\ ^{+3.5}_{-3.7}(\text{stat.})\ \pm 0.4(\text{sys.})\ [\text{pb}]$$

$$\sigma c = 42.2\ ^{+10.9}_{-10.0}(\text{stat.})\ ^{+5.5}_{-4.8}(\text{sys.})\ [\text{pb}]$$

forward-backward production asymmetry

$$A_{FB}{}^b = -0.51 \pm 0.29 \pm 0.03$$

$$A_{FB}{}^c = -0.50 \pm 0.20 \pm 0.02$$

Fragmentation of b and c quarks has also been studied.

energy fraction of b- and c-hadron relative to parent quarks are

$$\langle X_b \rangle = 0.60\ ^{+0.19}_{-0.07}(\text{stat.})\ ^{+0.02}_{-0.03}(\text{sys.})$$

$$\langle X_c \rangle = 0.50\ ^{+0.11}_{-0.08}(\text{stat.})\ ^{+0.01}_{-0.02}(\text{sys.})$$

This is the first measurement of forward-backward charge asymmetry of the c quark using semileptonic decays at TRISTAN energy region.

Acknowledgment

I am fortunate in having been able to join VENUS collaboration since 1988. I had a chance to install and complete a transition radiation detector system (TRD). I am glad to finish my thesis with a detector which I have been involved so much in working out. Moreover, I had an exciting time with a high luminosity experiment and with competing other experimental groups.

My thanks firstly go to Prof.Y.Nagashima, who has taught me since I was an undergraduated student and gave me a chance to join VENUS collaboration.

I would like to thank Dr.J.Haba for his helpful guidance and illumination of physics. He taught me many aspects of and how to do research in high energy physics throughout my work in VENUS collaboration. Without his encouragement, I could not have endured my long hard work.

I thank Prof.T.Yamanaka and Dr.M.Takita for their useful suggestions and advises.

I would like to acknowledge kindness which many collaborators in TRD group extended to me. Specially, I thank Dr.M.Sakuda. He taught me many things not only about the TRD system but also about the analysis of semileptonic decays. I could not have finished the analysis in this thesis without his support. I thank Prof.K.Ogawa who is the spokesman of VENUS collaboration. I wish to thank other collaborators in VENUS group and TRISTAN accelerator group.

Especially, I acknowledge the work of Dr.A.Krüger and Mr.D.Tatsumi on electron identification and photon conversion rejection. I wish to thank Dr.N.Terunuma and Dr.A.Suzuki, senior members of the TRD group.

I thank my friends, Mr.H.Takaki and Dr.F.Hinode, who worked in VENUS group at the same period and encouraged me. I thank Miss.S.Tsuzuki, Mrs.Annen and Mrs.Roppongi who are secretaries of Osaka Univ. and KEK.

Finally, I wish to thank my parents, brother who are always my 'guiding-light' and my fiancee, Miss.M.Jimbo, for their encouragement during my long graduate time.

Table of Contents

Chapter 1
Introduction

1.1. Quark Pair Production in e^+e^- annihilation

First, we give a brief history of discoveries of 'new' quarks in e^+e^- annihilation experiments, and 'standard model' of elementary particles. Second, we review current status of the quark pair production in the framework of the standard model. The fragmentation phenomenon of the heavy quarks into hadrons is also described in this section.

1.1.1. History of Heavy Quark discoveries and Standard Model

Electron-positron colliding experiments are 'clear' in the following two senses: 1) a full beam energy is effectively utilized because the electron and positron are point-like particles, 2) the initial state of the reactions is completely known. As a consequence of such advantages, electron-positron colliding experiments have made various contributions to elementary particle physics. In 1974, ψ resonance which is a bound state of $c\bar{c}$ (charmonium) was discovered in SPEAR[1]. (ψ (alias J) was also found at BNL in a proton-nucleus collision.) In 1975, τ-lepton was discovered in SPEAR[2]. In 1977, several Υ resonances which consisted of $b\bar{b}$ were observed clearly in DORIS, CESER.(They had been originally discovered by proton-nucleus collision at Fermilab[3].) With increased collision energy, PEP and PETRA confirmed the existence of the gluon. Since 1987, TRISTAN experiments have been in operation and have contributed much to the elucidation of the standard model. In 1989, SLC and LEP experiments started their operations at the center-of-mass energy around Z^0 pole.

We now consider that leptons and quarks are fundamental particles of the matter. Only 6 types of leptons and quarks and their antiparticles exist in the standard model. They are point-like spin 1/2 fermions. In addition, there are four types of intermediate bosons (γ(photon), Z^0(neutral weak boson), $W^{\pm}$(charged weak boson), g(gluon)) which are considered as the force carriers. Mass eigenstates of fermions that are called 'flavor' are grouped into three generations in ascending order of mass.

$$\text{leptons; } \begin{pmatrix}\nu_e\\ e^-\end{pmatrix}, \begin{pmatrix}\nu_\mu\\ \mu^-\end{pmatrix}, \begin{pmatrix}\nu_\tau\\ \tau^-\end{pmatrix} \qquad \text{quarks; } \begin{pmatrix}u\\ d\end{pmatrix}, \begin{pmatrix}c\\ s\end{pmatrix}, \begin{pmatrix}t\\ b\end{pmatrix}$$

The 't' quark has not been discovered yet. The 'standard model' is a successful theory that well describes behaviors of the elementary particles. It contains the electroweak theory and quantum chromodynamics (QCD), both of which are based on a principle of local gauge invariance. The former is the unified theory of electromagnetic and weak interaction[4]. QCD describes the strong interaction. Gauge invariance is believed to be a fundamental principle which determines the form of the particle interactions. The 3 interactions (excluding gravitation) are embedded in $SU(3) \times SU(2) \times U(1)$ gauge group.

1.1.2. Quark Pair Production

Quarks are produced in pair in the e^+e^- annihilation via a reaction

$$e^+e^- \rightarrow f\bar{f} \qquad (1\text{-}1)$$

where f signifies a quark and $\bar{f}$ is an anti particle. Pairs of u,d,s,c,b,t quarks will be produced if the center of mass energy exceeds two times of their mass. Fig.1-1 gives diagrams of quark pair production. We call a quark from pair production as 'primary quark' to distinguish it from those picked up from vacumm in hadronization.

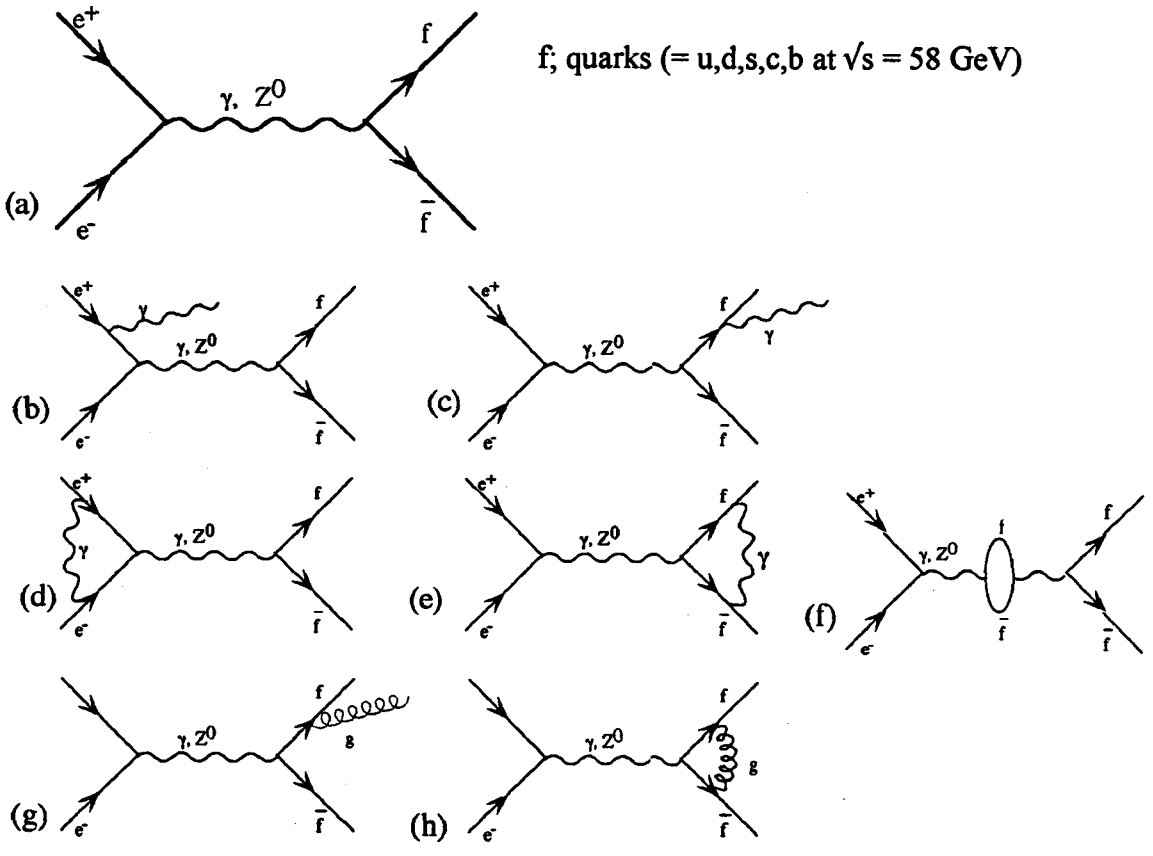

Fig.1-1 Diagrams of Quark Pair production in e^+e^- Annihilation

Figures show diagrams of quark pair production in e^+e^- annihilation. (a) lowest level diagram, (b,c) initial and final state photon radiation, (d,e) QED vertex correction term, (f) vacuum polarization of fermion pair, (g,) gluon emission, (h) QCD vertex correction term

Cross Section & Forward-Backward Asymmetry

The differential cross section in first order QED (Quantum Electrodynamics) for the production of a massless quark pair with electric charge (e_q) is:

$$\frac{d\sigma}{d\Omega} = \frac{\alpha^2}{4s} e_e^2 e_q^2 (1+\cos^2\theta) \tag{1.2}$$

with electron charge (e_e)=1. θ is the angle between the electron and the quark and s is square of total center of mass energy and α is a fine structure constant. Note that the cross section is proportional to the square of the quark charge.

Including electroweak effect, the equation (1.2) is modified as;

$$\frac{d\sigma}{d\Omega} = \frac{\alpha^2}{4s} [\, A(1+\cos^2\theta) + B\cos\theta \,] \tag{1-3}$$

$$A = e_e^2 e_q^2 + 2\, e_e e_q\, v_e v_q\, \Re X + (v_e^2 + a_e^2)(v_q^2 + a_q^2)\, |X|^2 \tag{1-4}$$

$$B = 4\, e_e e_q\, a_e a_q\, \Re X + 8\, v_e v_q\, a_e a_q\, |X|^2 \tag{1-5}$$

where $\Re$ means real part, X represents Z^0 propagation term and is given as follows .

$$X = \frac{\rho G_F M_z^2}{8\pi\alpha\sqrt{2}} \frac{s}{s - M_z^2 + i M_z \Gamma_z} \tag{1-6}$$

where G_F is Fermi-coupling constant, ρ is the ratio of neutral to charged current coupling strength and is very close to 1. M_z and Γ_z are mass and total width of Z^0 pole The fermion vector coupling constant (v_f) and axial vector coupling constant (a_f) are given as follows with Weinberg angle (θ_W).

$$v_q = \frac{e_q}{|e_q|} - 4\, e_q \sin^2\theta_W = \begin{cases} -1 + \frac{4}{3}\sin^2\theta_W & (q=d,s,b) \\ +1 + \frac{8}{3}\sin^2\theta_W & (q=u,c,t) \end{cases} \tag{1-7}$$

$$a_q = \frac{e_q}{|e_q|} = \begin{cases} -1 & (q=d,s,b) \\ +1 & (q=u,c,t) \end{cases} \tag{1-8}$$

An important observable is R_q, the ratio of hadronic total cross section to that of QED $e^+e^- \to \mu^+\mu^-$ process.

$$R_q = \frac{\sigma(e^+e^- \to f\bar{f})}{\sigma(e^+e^- \to \mu^+\mu^-)} \tag{1-9}$$

Its numarator can be obtained from eq(1-3) by integration over poler angle, and summing over all quark species. Similarly the denominator is obtained from eq(1-3), but replacing e_q with e_μ(=1) and setting all v_μ's and a_μ's to zero.

$$R_q = \frac{e_q^2 A_q}{e_e^2} \tag{1-10}$$

where A_q is a value A of fermion.
The forward-backward asymmetry $A_{FB}{}^q$ is defined as

$$A_{FB}{}^q = \frac{\int_0^1 \frac{d\sigma}{d\Omega} d\cos\theta - \int_{-1}^0 \frac{d\sigma}{d\Omega} d\cos\theta}{\int_{-1}^1 \frac{d\sigma}{d\Omega} d\cos\theta} \tag{1-11}.$$

Therefore, it is given as

$$A_{FB}{}^q = \frac{3}{8}\frac{B}{A}$$

$$= \frac{3}{2}\frac{a_e a_q}{e_e e_q} \Re X + (\text{Weak}^2) \tag{1-12}$$

At TRISTAN energy region (~60GeV), $|X|^2$ term in eq(1-4,5) makes negligible contribution in eq(1-12). Therefore vector and axial components decouple, the former contributing only to Rq and the latter only to A_{FB}. The weak squared term is less than 10% at TRISTAN energy region. The factor $\frac{a_e a_q}{e_e e_q}$ is always positive for all leptons and quarks. The sign of the asymmetry is determined by the sign of $\Re X$ to be negative below the Z^0 resonance. The equation (1-12) shows a fact that the forward-backward asymmetry effects determine the axial vector coupling (a_q). Fig.1-2 shows the forward-backward asymmetry of b and c quark production calculated with equation(1-12) with values $\sin\theta_w$ = 0.231, Mz = 91.16 GeV/c^2, Γz = 2.5 GeV/c^2, b quark mass = 5.0 GeV/c^2, c quark mass = 1.35 GeV/c^2. The Z^0 mass and width are taken from recent results of LEP and SLC experiments[5].

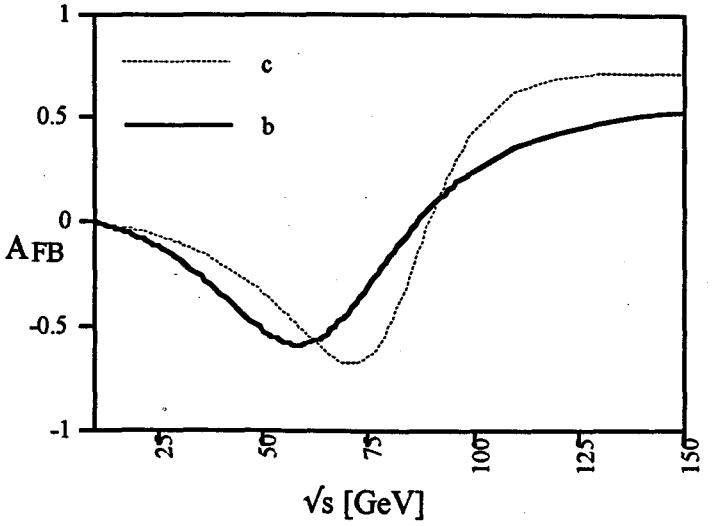

Fig.1-2 Forward-Backward Asymmetry of b/c Quark

The dotted line shows the forward-backward production asymmetry of c quark and the solid line gives that of b quark.

As shown in the figure, the asymmetry is negative and largest around 60 GeV, where the interference of γ and Z^0 diagram in Fig.1-1 is at its maximum. Thus it is clear that TRISTAN experiments are expected to see clear signature of the forward-backward production asymmetry. A precision measurement of the forward-backward asymmetry can decide the value of axial vector coupling.

Higher Order Corrections in QED & QCD

As shown in Fig.1-1, there are several higher order diagrams contributing to the quark pair production. Their effect ('Radiative correction') has to be taken into account in order to compare experimental measurements with theoretical expectations. The lowest order differential cross section should be modified as

$$\frac{d\sigma}{d\cos\theta} = \frac{d\sigma_{\text{lowest}}}{d\cos\theta}(1+\delta) \qquad (1\text{-}16)$$

where δ is the correction term of higher order QED. It is different for each quark flavor. The average value over 5 flavors is 0.33 at $\sqrt{s}$ = 58 GeV. The initial state photon radiation lowers the effective center-of-mass energy. After standard hadronic event selection by VENUS detector system (See Chapter-3), the effective center-of-mass energy is lower by about 2 GeV than 2 E_{beam}. In asymmetry measurements, we consider this effect in Chapter-5. QCD effect such as a hard gluon emission would affect R and A_{FB}. The diagram (Fig.1-1(g,h)) are the contribution of the QCD. Including QCD effect, R and A_{FB} are represented as follows[6].

$$R = 3\,\Sigma R_q\ [1+(\frac{\alpha_s}{\pi}+1.41\,(\frac{\alpha_s}{\pi})^2)\frac{f_1 R_q^{VV}+f_2 R_q^{AA}}{R_q}] \qquad (1\text{-}17)$$

$$A_q = [\frac{3}{4}\beta^3 + f_3(\frac{\alpha_s}{\pi} + 1.41(\frac{\alpha_s}{\pi})^2)]\frac{R_q^{VA}}{R_q} \qquad (1\text{-}18)$$

with

$$R_q^{VV} = e_e^2 e_q^2 + 2 e_e e_q v_e v_q \Re X + (v_e^2 + a_e^2) v_q^2 |X|^2 \qquad (1\text{-}19a),$$

$$R_q^{AA} = (v_e^2 + a_e^2) a_q^2 |X|^2 \qquad (1\text{-}19b),$$

$$R_q^{VA} = 4 e_e e_q a_e a_q \Re X + 8 v_e v_q a_e a_q |X|^2 \qquad (1\text{-}19c).$$

where β is the relativistic factor ($\beta = v/c$, v is quark velocity, c is the light speed). The coefficients f_1, f_2, f_3 are QCD correction factors and they depend only on the quark velocity. The observed value should be corrected with them to compare the theoretical expectation.

1.1.3. Fragmentation of Quark into Jet

The primary quarks which are produced in e^+e^- reaction convert into several partons (quarks and gluons) due to QCD effects and eventually into hadrons ('hadronization / fragmentation') (See Fig.1-3). The energy transfer (ΔE) in the hadronization of a primary quark Q→H+q (Q;primary quark, H; hadron which contains the primary quark, q; a quark produced in the fragmentation) is

$$\Delta E = E_H + E_q - E_Q \tag{1-20}$$

where E_H, E_q, E_Q are the energies of H, q and Q. Expressing in terms of momentum p of the primary quark and fractional momentum that is transferred to the hadron (x), ΔE can be rewritten as follows.

$$\Delta E = \sqrt{m_Q^2 + x^2p^2} + \sqrt{m_q^2 + (1-x)^2p^2} - \sqrt{m_Q^2 + p^2} \tag{1-21}$$

Here $m_H \approx m_Q$ is assumed where m_Q is mass of the primary quark and m_H is that of hadron. Using $\varepsilon_q = (\frac{m_q}{m_Q})^2$ (m_q is mass of the quark produced at fragmentation) and taking limit $P \gg m_q, m_Q$,

$$\Delta E \propto 1 - \frac{1}{x} - \frac{\varepsilon_q}{1-x} \tag{1-22}.$$

ε_q is treated as a free parameter to be fit to the data. At high energy, x can be approximated by $Xq = \frac{E_{hadron}}{E_{beam}}$,where E_{hadron} is the energy fraction of hadron contains the primary quark. The relative probability of the hadronization $D(Xq)$ is given by the square of transition amplitude times phase space. Since the transition amplitude is proportional to $\frac{1}{\Delta E}$ and to $\frac{1}{X}$ a phase space of decay, $D(Xq)$ can be represented as follows.

$$D(Xq, \varepsilon_q) = \frac{1}{Xq\,(1 - \frac{1}{Xq} - \frac{\varepsilon_q}{1-Xq})^2} \tag{1-23}$$

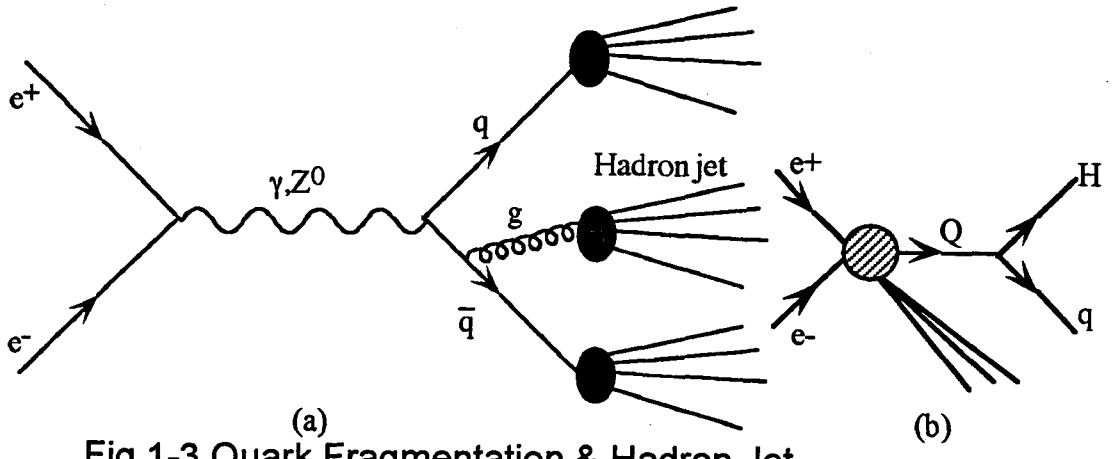

Fig.1-3 Quark Fragmentation & Hadron Jet

(a) The pair-produced quarks converts into partons. The partons (quarks, gluons) fragments into many hadrons. Hadrons which come from the same parton are collimated. They form 'hadron jets'. (b) schematic illustration of fragmentation with notation in the text.

$D(Xq)$ is called as the fragmentation function. The distribution is different for each quark flavor and is related to its mass. The fragmentation function and these kinematical idea were proposed by Suzuki[7], Bjorken[8] and Peterson, et al[9]. Fig.1-4 shows $D(Xq,\varepsilon_q)$ for various ε_q. If ε_q decreases, the fragmentation of the quark becomes 'hard' (i.e. the hadron taking most of its parent quark energy) as shown in the figure. The mean fractional energy of the quark ($<Xq>$) is also used to describe the fragmentation phenomena. Fig.1-5 shows $<Xq>$ as a function of ε_q.

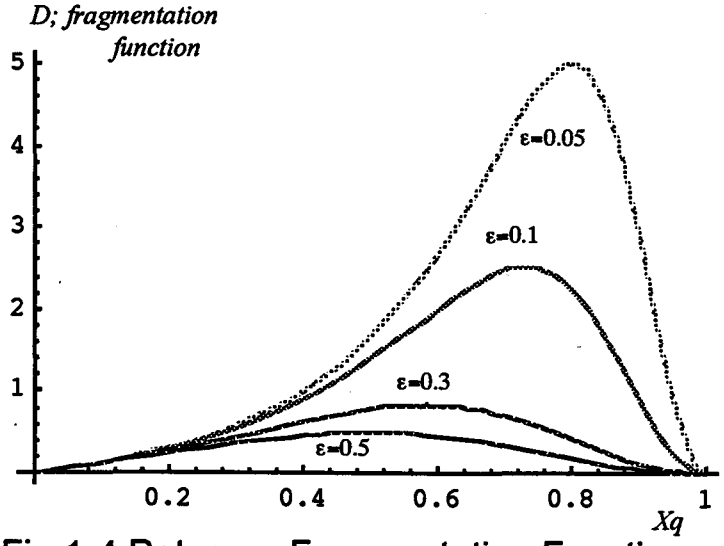

Fig.1-4 Peterson Fragmentation Function

Peterson fragmentation function that is given in the main text. The figure contains distributions with ε_q= 0.05, 0.1, 0.3, 0.5.

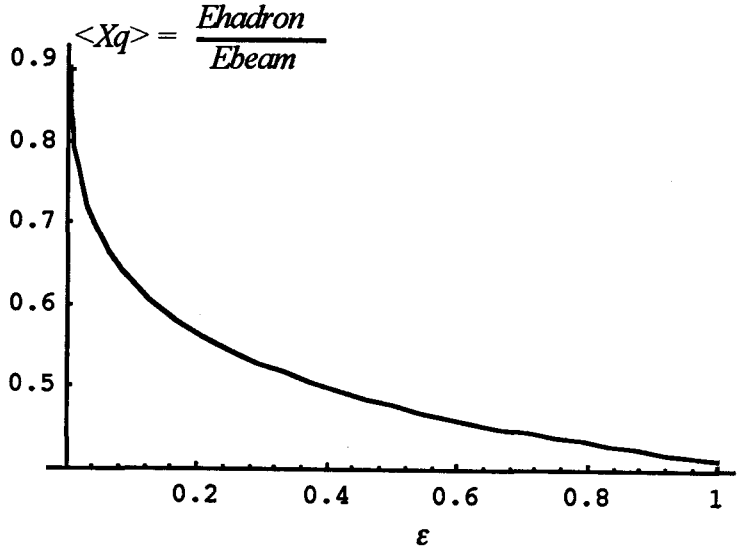

Fig.1-5 $<Xq>$ vs. ε_q with Peterson Function

The figure shows the mean energy fraction of the hadron that contains the primary quark as a function of ε_q.

1.2. An Electron in Multihadronic Final States

In a multihadronic final state of the quark pair production, electrons appear occasionally via various processes. In this section, we give a detail of such electrons. Especially, those from semileptonic decay of heavy quarks are given.

Note: We use following words for specific electrons. 'Inclusive electron' means an electron in the multihadronic events ($e^+e^- \rightarrow$ e X). It includes electrons from various sources. 'Semileptonic decay electron' is the electron from decay of heavy (b,c) quarks. 'Prompt' is semileptonic decay component of inclusive electrons in real data and its source (as b or c) can not be specified exactly.

1.2.1. Semileptonic Decay of Heavy Quarks

Weak Decay of Heavy Quarks

One of electron sources is a semileptonic decay of the heavy quark. Fig.1-6 shows diagrams of b and c quark semileptonic decay. The heavy quark decays into a lighter quark and a virtual weak boson. The emitted weak charged boson subsequently decays into a charged lepton and a neutrino. The charge of the weak boson should be determined by the quark charge. Therefore the charge of the lepton reflects the charge of the parent quark. Most of the time , the weak boson decays into a quark pair instead of the lepton pair. Fraction of each decay can be estimated roughly by counting the number of degree of freedom.

For the b quark semileptonic decay, each decay width Γ is proportional to,

$$\Gamma e\nu_e : \Gamma\mu\nu_\mu : \Gamma\tau\nu_\tau : \Gamma ud : \Gamma cs = 1 : 1 : 1 : 3 : 3$$

where the suffix denotes its final state. The factor 3 comes from a color degree of freedom of the quark. A channel in which b decays into u is possible but is heavily suppressed by Kobayashi-Maskawa matrix.[10]

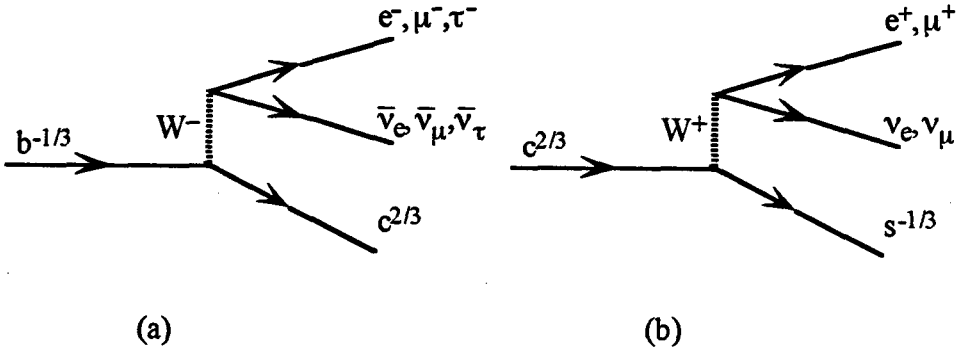

Fig.1-6 Semileptonic Decay of b/c quark

The figure shows the diagram of semileptonic decay of b and c quark. (a); b quark semileptonic decay, (b) c quark semileptonic decay.

Therefore, the decay branch is given as;

$$BR(b\to ce\text{-}\bar{\nu}_e) \approx \frac{\Gamma e\nu_e}{\Gamma e\nu_e + \Gamma\mu\nu_\mu + \Gamma\tau\nu_\tau + \Gamma ud + \Gamma cs} = \frac{1}{9} \quad (1\text{-}24)$$

The above simple calculation shows the semileptonic decay branching ratio of b quark is roughly ~10%. The world average value of measurements of BR(b→$e^{\pm}\nu_e$ hadrons) is 10.8 ±0.5%[11]. Though this simple formula is not exactly valid for c quark decay due to an additional contribution from annihilation process, it is known to be 9.6 ±0.9%[12] of the world average value of measurements.

Momentum Spectrum of Semileptonic Decay Electron

An important feature of the electron from semileptonic decay is its momentum spectrum. In the center of mass coordinate system of the b(c) quark, the electron momentum is decided by the energy transfer in the b→c (c→s)transition. It is roughly equal to the mass difference between b and c (c and s). Therefore, the momentum of the electron in b(c) center-of-mass system and hence the transverse momentum relative to the quark direction in the laboratory system is different for the b and c quark. Fig.1-7 shows the transverse momentum (p_t) distribution of the electron from b, b cascade and c. The b cascade decay is b→cX→eX'X. The quark direction is defined in Appendix-2.

It is found from the figure that the electron from b decay has higher p_t than that from c decay . In general, this characteristic is universal for different $\sqrt{s}$ region. We can enrich b or c quark in a hadron sample using p_t of the electron.

On the other hand, the absolute momentum (p) of the electron is affected by the Lorentz boost of the heavy quark (center of mass system of heavy quark → laboratory system). Fig.1-8 shows the momentum spectrum of the electron from b and c semileptonic decay. We already described in the section 1.1.3, that the b quark fragmentation is harder than c quark. Therefore, the momentum spectrum of the b electron is harder than c electron as shown in Fig.1-8.

Using these characteristics of p and p_t spectrum, we can separate or enrich events from b or c quark in the multihadronic process which is a mixture of all five flavors. The 2-dimensional p-p_t spectrum provides a good information to find the source of the inclusive electron.

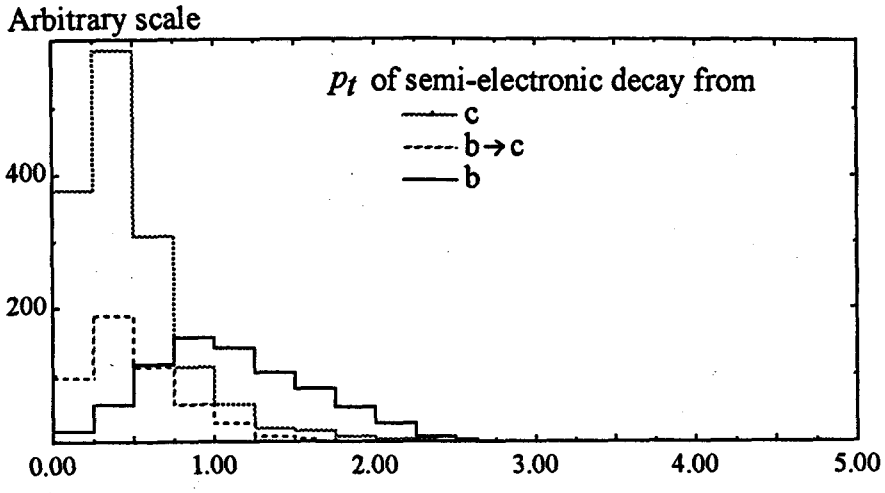

Fig.1-7 Transverse Momentum of the Electron from Semileptonic Decay

The transverse momentum p_t with respect to the quark jet axis. The dotted line; c→eX, the dashed line; b→cX→eX'X and the solid line; b→eX. The jet clustering was done with ymin = 0.05. (See Appendix-2)

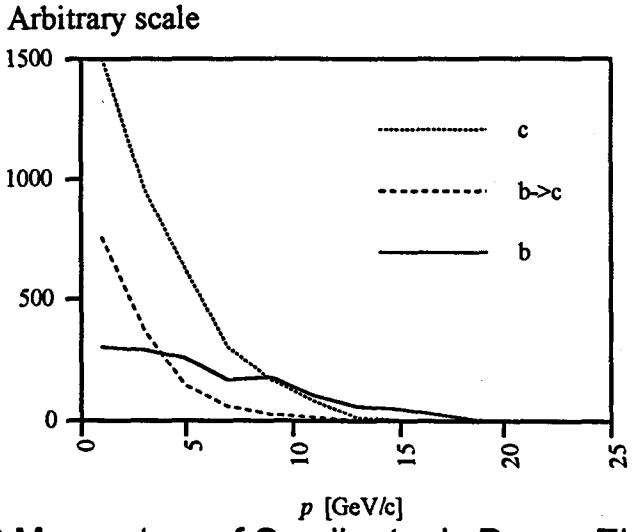

Fig.1-8 Momentum of Semileptonic Decay Electron

The momentum spectrum of semileptonic decay electron. The dotted line; c→eX, the dashed line; b→cX→eX'X and the solid line; b→eX

1.2.2. Other Sources

There are other sources of electrons in a multihadronic final state. They become backgrounds for the study of the heavy quark using its semileptonic decay. We will call the electron from the semileptonic decay in a data sample as 'prompt electron' in comparison to other background electrons.

Photon Conversion in Material

One of electron sources other than the semileptonic decay is photon (γ) conversion in a material ($\gamma \rightarrow e^+e^-$). The photon comes from the decay of π^0.About 98.8% of the neutral π^0 decay into 2 photons ($\pi^0 \rightarrow \gamma\gamma$). Most of the hadrons in a multihadronic final state are pions. The fraction of the neutral pion is roughly 1/3. Therefore, there are many photons from π^0 in the final state of multihadronic events. The photon would be converted to an electron-positron pair in the material. Our detector (VENUS detector system, See Chapter-2) has material of about 7% radiation length inside the charged track detector. The number of electrons from photon conversion is estimated as $[1- \exp(-7/9 \times 7\%)] \times 2 \times 1/3$ of all particles. These will become a background for prompt electron. However, their momentum is low ($\lesssim$2 GeV/c) and their transverse momentum relative to the quark direction is very small ($\lesssim$0.1 GeV/c), because most of π^0 have very low p and p_t . Moreover, the conversion electron pair have a clear signature. The electron from conversion is accompanied by an opposite charge track (positron). The two opposite charge track can be traced to the same point in the material. Using these characters, we can discriminate conversion electron (See Appendix-3).

Dalitz Decay of π^0

The π^0 has a small branching fraction decaying into an electron pair and 1 photon ($\pi^0 \rightarrow e^+ e^- \gamma$) which is called as 'Dalitz decay'. The momentum spectrum of these electrons are similar to that of the conversion electrons. However, the decay vertex is not in the material. Because the branching ratio is about 1.2 %, the yield is less than 10% of that of conversion electrons.

1.3. Strategy and Outline of This Thesis

The study in this thesis consists of two parts. One study is on electron identification, and the other is on the spectrum of the heavy quark using inclusive electrons.

The electron identification in multihadronic final state is a difficult task, because there are several hundred times more hadrons than electrons. The VENUS detector system that will be explained in the next chapter, has a powerful tool for electron identification. By combining the 'Transition Radiation Detector' with the lead glass calorimeter, the power of VENUS to identify electrons was greatly enhanced and we succeeded in obtaining an electron sample of high purity. Equipped with the new electron identification tool, the number of backgrounds which come from conversion and misidentification is greatly reduced and has been accurately estimated in each data reduction. Then the remaining number of prompt electron is used to derive the production cross section, its forward-backward asymmetry and the fragmentation function of the heavy quark simultaneously. The plan of this thesis is as follows.

Chapter-2 describes the experimental apparatus of TRISTAN and VENUS detector system. This chapter also includes the description of the Transition Radiation Detector

Chapter-3 describes event reconstruction and data reduction in VENUS. Selection criteria of multihadronic final state in VENUS is given in this chapter.

Chapter-4 describes the electron identification which is a key issue in this present work.

Chapter-5 describes the study of heavy quarks using electron candidates. In this chapter, The measurement of cross section and asymmetry of the b/c quarks using electron candidates are also described.

Chapter-6 includes discussion and conclusion.

In appendices, the definition and the selection of 'single electron' and two-photon events, jet clustering and rejection of photon conversion electrons are given.

References

[1] J.E.Augustin et al., Phys.Rev.Lett. 33(1974)1406.

[2] M.L.Perl et al., Phys.Rev.Lett. 35(1975)1489.

[3] S.Herb et al., Phys.Rev.Lett. 39(1977)252.

[4] S.L.Glashow, Nucl.Phys. 22(1961)579;
S.Weinberg, Phys.Rev.Lett. 19(1967)1264;
A.Salam and J.C.Ward, Phys.Lett. 13(1964)168

[5] ALEPH Collab., D.Decamp et al., Phys.Lett. 231(1989)519;
L3 Collab., B.Adeva et al., Phys.Lett. 231(1989)509;
DELPHI Collab., P.Aarnio et al., Phys.Lett. 231(1989)539;
OPAL Collab., M.Z.Akrang et al., Phys.Lett. 231(1989)530;
MARK II Collab., G.S.Abrams et al., Phys.Lett. 63(1989)720;

[6] Applequist T and Politzer D, Phys.rev.**D12**(1975)1404
Pennington M R, "Cornerstones of QCD", Repts.on Progr.in Phys.46(1983)393
Jersàk J et al., Phys.Lett.**98B**(1081)363

[7] M.Suzuki, Phys.Lett. **B71**(1977)139

[8] J.D.Bjorken, Phys.Rev. **D17**(1978)171

[9] C.Peterson et al., Phys.Rev. **D27**(1983)105

[10] M.Kobayashi and K.Masukawa, Progr.Theor.Phys. 49(1973)652

[11] ARGUS collab., H.Albrecht et al., Phys.Lett. **B249**(1990)359
CLEO collab., S.Henderson et al., Phys.Rev. **D45**(1992)2212

[12] ARGUS collab., H.Albrecht et al., Phys.Lett. **B278**(1992)202

Chapter 2
Experimental Apparatus

The data analyzed in this thesis were obtained by VENUS at TRISTAN experiment. At first, we give a brief description of TRISTAN accelerator complex. Then, we explain VENUS and other TRISTAN apparatus in detail.

2.1. TRISTAN

TRISTAN (Transposable Ring Intersecting Storage Accelerator in Nippon)[1] is an electron-positron collider at National Laboratory for High Energy Physics (KEK) in Tsukuba city, Japan. Fig.2-1 is a layout of TRISTAN. It started its operation in November, 1986. Since then, the beam energy and luminosity have been improved steadily. The QCS (Super Conducting Quadruple magnets) were installed in the autumn of 1990. Since then, TRISTAN operation entered the second phase for high luminosity experiment. The TRISTAN accelerator complex consists of three parts; a linear accelerator, an accumulation ring and a main ring for colliding experiments.

2.1.1. Beam Injector & Linear Accelerator

A beam injection system consists of a pre-accelerator, a conversion target (generation system of electron and positron) and a post accelerator. The pre-accelerator is a high current electron linear accelerator (LINAC ,~10A, 200 MeV). The positron beam is produced by irradiating a tantalum target with an electron beam from the pre-accelerator. The post accelerator is another linac that accelerates both the electron and positron beams up to 2.5 GeV. The whole LINAC is 390m long and transpose the beam to the accumulation ring. The peak current of the electron (positron) beam is 100 mA(15 mA).

2.1.2. Accumulation Ring

The accumulation ring (AR) is an energy booster of the beam so that it can be injected into the main ring. It has a 377m circumference and accumulates electrons and positrons from LINAC. AR accumulates the beam up to 20 mA and accelerates them to 8 GeV. The 8 GeV electron or positron beam is then injected into the main ring (MR).

2.1.3. Main Ring

MR (main ring) consists of four straight sections for acceleration and four quadrant arc sections. The straight sections contain RF cavities for beam acceleration. The injected beam from AR is accelerated from 8 GeV to around 30 GeV and stored. The electron and positron beams are grouped each into 2 bunches that positioned symmetrically. There are four colliding sections. The beams collide every 5.0 μsec at the center of the straight sections. The vacuum in the beam pipe is kept at about $0.5\sim1.0 \times10^{-8}$ Torr to achieve long beam life.

In the second phase of the high luminosity operation starting 1991, the beam energy is fixed at 29 GeV. The average luminosity of the collision is 3.7×10^{31} /cm^2/sec. VENUS group compiled integrated luminosity 700~800 pb^{-1} per day on average. Parameters of TRISTAN-MR are listed in Table 2-1.

Table 2-1 The Parameters of TRISTAN Main Ring

Circumference	3018 m
Bending radius	246.5 m
Length of the straight section	194.4 m × 4
Total length of RF section	299.5 m
Injection beam energy	8 GeV
Maximum beam energy	32 GeV
Energy spread	2.33×10^{-3}
RF voltage	385.3 MV
RF frequency	508.58 MHz
RF frequency shift	3.0 kHz
Radiated energy in a turn	253 MeV
Beam revolution frequency	99.3 kHz
Numbers of colliding sections	4
Numbers of beam bunches	$e^- \times 2 + e^+ \times 2$
colliding interval	5 μsec
Beam life	200~300 min.

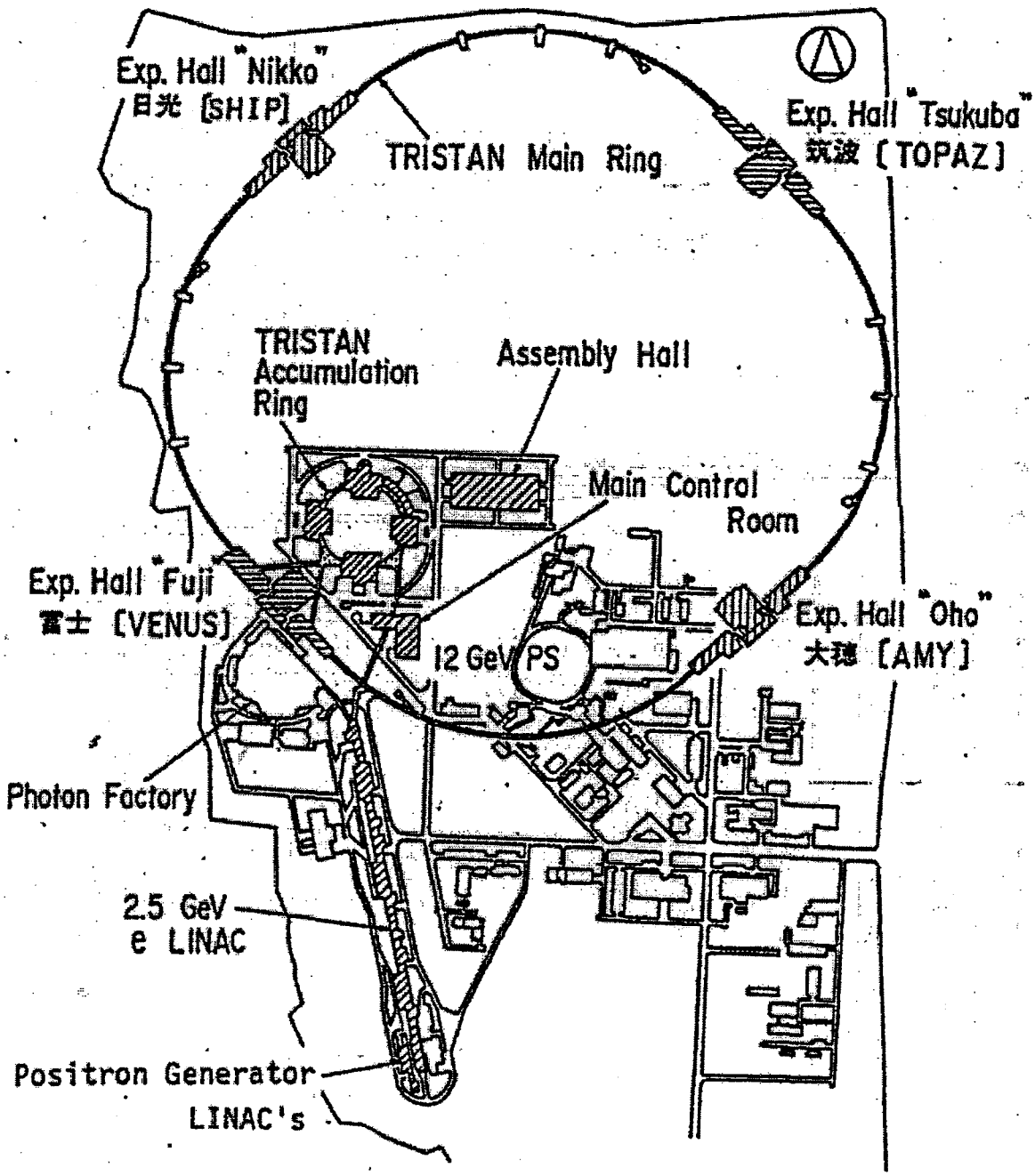

Fig.2-1 TRISTAN Layout

2.2. VENUS Detector

There are four colliding sections in TRISTAN MR. They are located in experimental halls called Fuji, Nikko, Tsukuba, Oho (See Fig.2-1). VENUS is in the Fuji experimental hall.

2.2.1. General Description

VENUS[2] (Versatile National laboratory and Universities Spectrometer) is a general purpose spectrometer. It has a cylindrical symmetry and good hermeticity. The coverage of the detector around the colliding point is 99.7% of 4π. Fig.2-2 shows a cut view of VENUS. The picture in Fig.2-3 was taken while it is under construction.

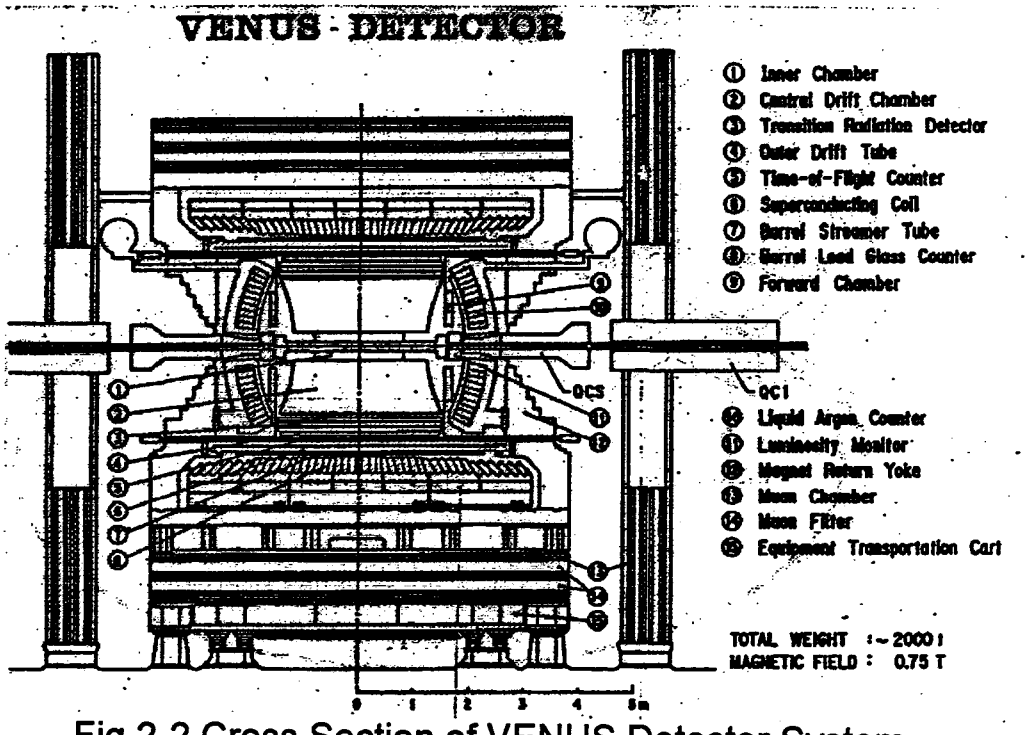

Fig.2-2 Cross Section of VENUS Detector System

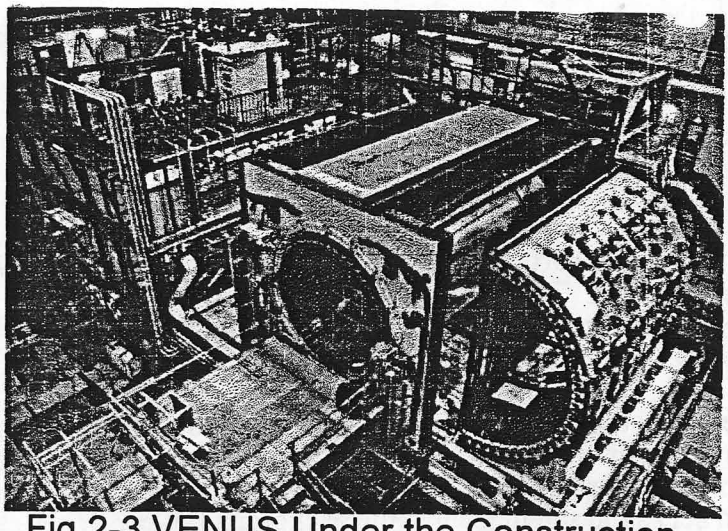

Fig.2-3 VENUS Under the Construction

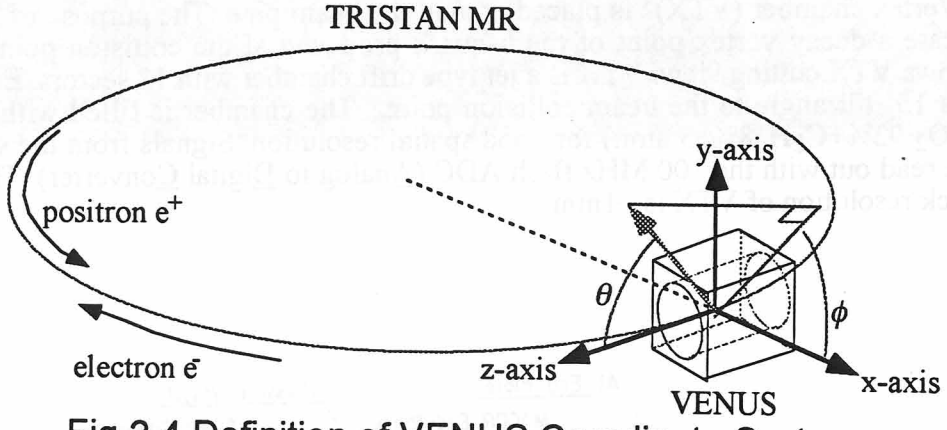

Fig.2-4 Definition of VENUS Coordinate System

The right handed coordinate system of VENUS is defined as Fig.2-4. The z-axis is parallel to the electron beam direction. The y-axis is the vertical direction. θ and ϕ are polar and azimuthal angles as defined in the figure. VENUS is made of many components which are described in the following sections.

2.2.2. Detector Components

In the following, many detector components of VENUS are described one by one outwards from the center.

Beam Pipe

The beam pipe is a part of both MR and vertex chamber (VTX). Fig.2-5 shows the beam pipe and VTX. The center part of the beam pipe is made of beryllium. The material was chosen for its low density and strength against compression. The thickness, outer diameter, and the length are 1.1, 98 and 240 mm. The beryllium pipe is covered with a 0.05 mm-thick titanium sheet to absorb background X-rays. The beam pipe on both sides of the beryllium is made of 3 mm-thick stainless steal. Stainless bellows are placed between the beryllium pipe and the stainless steel pipe to protect from the force exerted by the detector assembly. The stainless parts are expected to act as the shield against the background X-rays.

Vertex Chamber

Vertex chamber (VTX)[3] is placed around the beam pipe. The purpose of VTX is to locate a decay vertex point of the b-quark produced at the collision point. Fig.2-5 shows VTX cutting view. VTX is a jet type drift chamber with 12 sectors. Each sector has 15° tilt angle to the beam collision point. The chamber is filled with slow gas (CO_2 92%+$C_2H_6$8%, 3 atm.) for good spatial resolution. Signals from the sense wire are read out with the 100 MHz flash ADC (Analog to Digital Converter). The double track resolution of VTX is ~1mm.

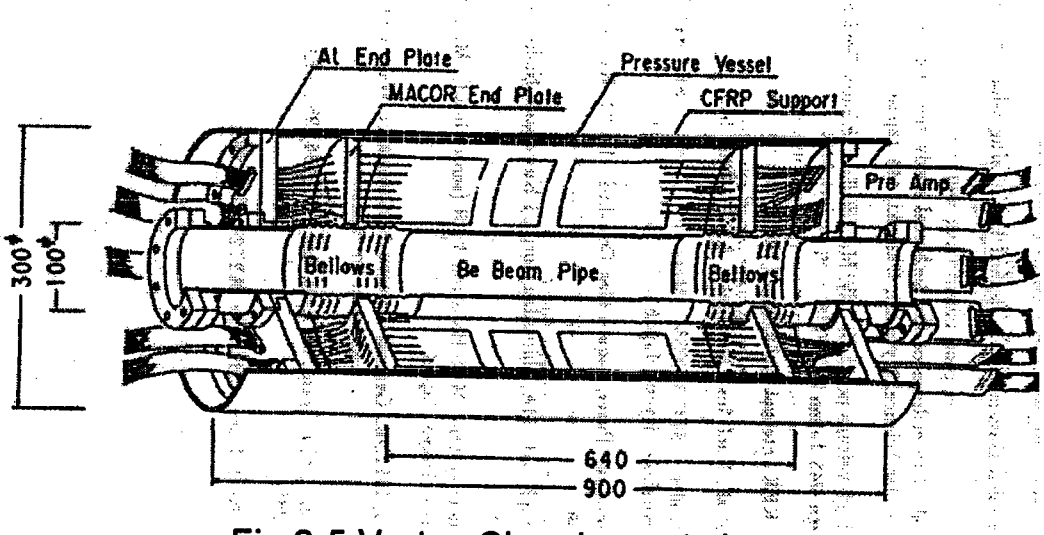

Fig.2-5 Vertex Chamber cut view

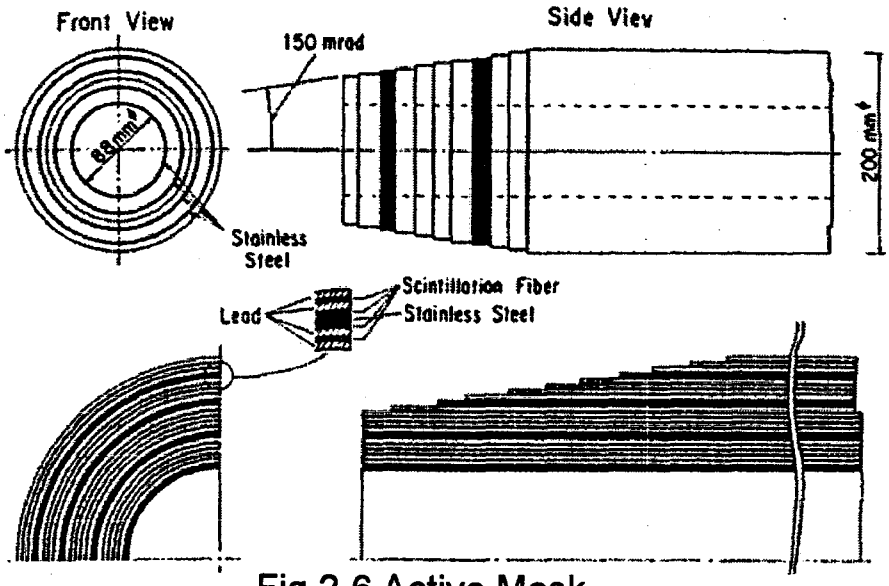

Fig.2-6 Active Mask

Trigger Chamber

The trigger chamber is placed outside of VTX. It consists of many layers of concentric cylindrical wire chambers. It finds tracks originating from the interaction point and serves to make a second level trigger.

Active Mask

Active mask[4] is both an electron shower detector and a shield against backgrounds made by the beam. It is a sandwich of cylindrical shape lead sheets and plastic scintillation fiber sheet. The structure is shown in Fig.2-6. The detector covers the small angle region (45~150 mrad.). It can tag Bhabha event (electron-positron elastic reaction $e^+e^-\rightarrow e^+e^-$) with a signal from the scintillation fibers. By counting the number of Bhabha events, the beam luminosity is measured.

Central Drift Chamber (CDC)

CDC[5] (Central Drift Chamber) is the main track detecting device of VENUS. It is a cylindrical multi-wire drift chamber. Fig.2-7a shows r-ϕ plane of CDC cross section. The inner and outer radius of CDC are 25 cm and 126 cm. The length is 300 cm. Side walls are CFRP (Carbon Fiber Reinforced Plastic) whose thickness are 1.5 mm for inner and 5.0 mm for the outer wall. End wall is made from aluminum. Wires are arranged in such a way to make a total of 7104 cells with single hit capability (Fig.2-7b). CDC has 20 layers of 'axial wire' cells that are parallel to z-axis and 9 layers of 'slant wire' cells that has ±3.3° tilt angle from z-axis in ϕ direction. Two adjacent layers of axial wires are staggered by half cell width. Polar angle coverage of CDC is $|cos\theta| \leq 0.75$. Signals from anode wires are amplified by pre-amplifiers placed on the end plate and sent to post-amplifiers & discriminators in the electronics hut. TDC's (Time to Digital Converter) measure the drift time of ionized electrons from passage of particles to arrival at the anode wires. Spatial resolution of charged tracks is typically 270 μm in the range of $|cos\theta| \leq 0.75$. Performance of CDC will be described in Chapter 4.

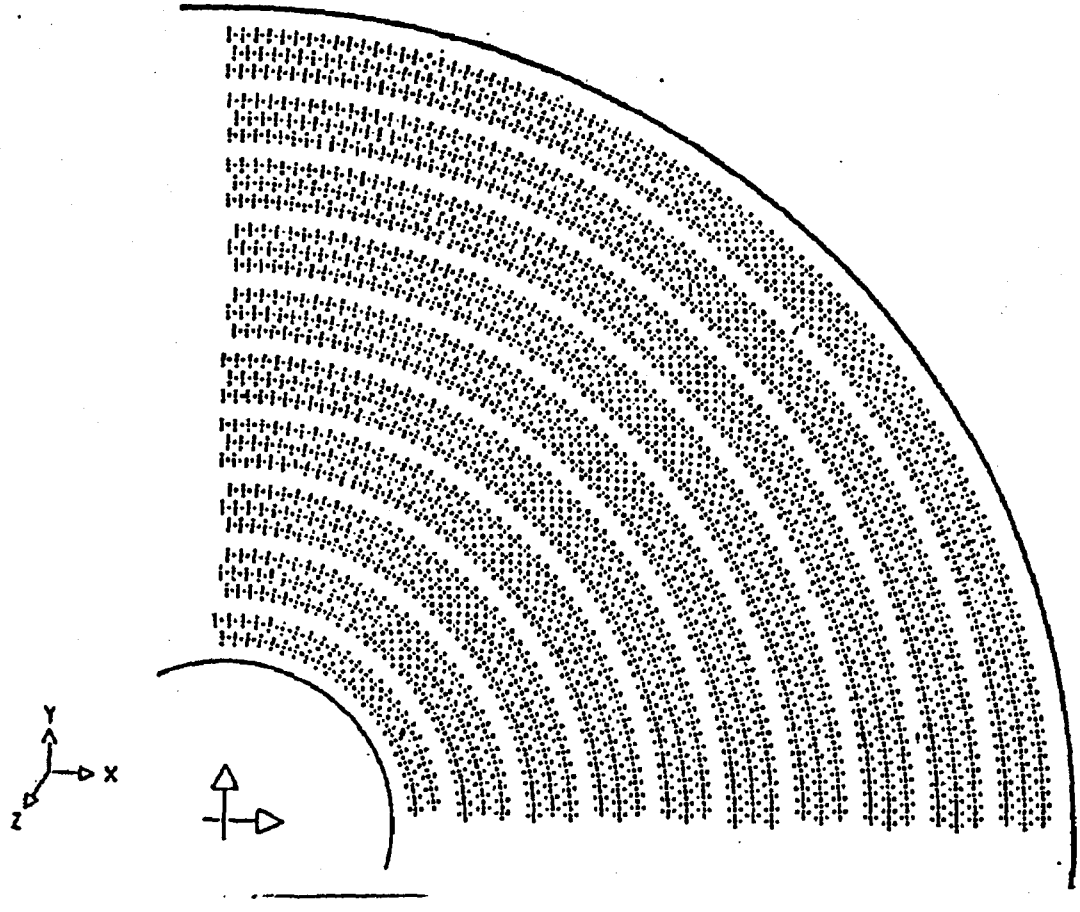

Fig.2-7a CDC Cross Section and Structure of a Chamber Cell
End view of one quadrant of CDC cross section.

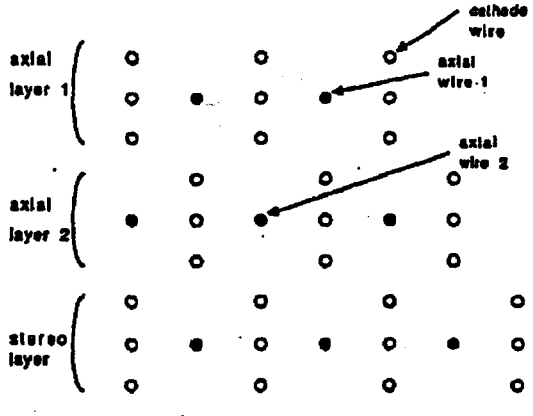

Fig.2-7b CDC Chamber Cell

Transition Radiation Detector (TRD)

TRD[6] (Transition Radiation Detector) is a special device for electron identification. It was installed in autumn, 1990 as a part of the upgrade plan of VENUS. It is placed between CDC and ODT (outer drift tube). The detector consists of two parts. One is x-ray chambers filled with Xe(90%)+CH_4(10%) gas and the other is radiator boxes which contain polypropylene fibers as radiator. A detailed description of TRD reserved another section (See section 2.2.3 for hardware and chaptert 4 for software analysis) because it is not only the author's major contribution but also it plays a crucial role in the present thesis.

Outer Drift Tube

Outside TRD is an outer drift tube system (ODT) which consists of three layers of staggered cylindrical drift tubes which have 284.4cm of length. ODT occupies the position at the radius range between 157cm and 162cm. It covers angle range of $|\cos\theta| \leq 0.66$.

Time-of-Flight Counter

Time-of-flight counter system (TOF) consists of 96 scintillation counters with rectangular cross section of 10.7cm×4.2cm and have a length of 466cm. They are placed along the z-axis cylindrically at 164cm inner radius. Photo-multiplier tubes (PMT) are attached to both sides of the counter through light-guides 145cm long. TOF covers angle range of $|\cos\theta| \leq 0.81$. The time resolution of the TOF is 200 ps.

Super Conducting Magnet

VENUS magnet produces a magnetic field of 7500 gauss strength. The magnetic field is uniform within 0.3% deviation over the whole volume of CDC. The magnet system consists of super conducting solenoid, flux return yoke, a helium refrigerator and a high current power supply. Its inner radius is 177 cm and length is 527 cm. The iron return yoke supports the magnetic force about 230 t.

Barrel Streamer Tube

The barrel streamer tube system (BST) is placed between the magnet and the Lead glass calorimeter. Each tube has a rectangular cross section of 1.9 cm × 1.35 cm and has a length of 444 cm. Total of 1200 tubes are grouped into 16 modules, two staggered layers of cylindrical shape. The anode wire is strung at the center of the tubes. Copper cathode strips are attached onto the inner and the outer side of the modules. The inner strips are aligned perpendicular to z-axis and outer ones are inclined by 45 degree to them. BST operates in the limited streamer mode. The detector gives hit points of charged particles and electron converted from photons at the coil.

Barrel Lead-Glass Calorimeter (LG)

An electromagnetic calorimeter measures energies and incident position of electrons and photons. Barrel lead-glass electromagnetic calorimeter (LG) of VENUS has a cylindrical shape with radius of 2 m and length of 6m. It consists of 43 rings and each ring has 120 modules giving total of 5160 counter modules. Fig.2-8 shows the structure of LG. The modules are arranged in a semi-tower-geometry, approximately pointing to the collison point. They are tilted by 3° in ϕ-direction and by 7° in θ -direction so as not to miss particles through the gaps between counters. The gaps are of 1.5 mm width typically. LG covers angle region of $|\cos\theta| < 0.79$. One module of LG calorimeter consists of a lead-glass block, a light guide and a photomultiplier tube. The lead glass (DF6 type) block is 30 cm in depth and its typical cross section is 12 cm × 11.6 cm at the front face. The depth of the lead-glass corresponds to 18 X_0 or 1 nuclear interaction length. Main ingredients of DF6 are PbO(70.9%) and SiO_2(27.3%). DF6 has density 5.18 g/cm^3, 1 X^0 of 1.68 cm and refractive index of 1.805. The plastic light-guide is 6 cm long.

An electromagnetic shower induced by an electron or a photon of the energy up to more than 30 GeV is well contained in LG. The electromagnetic shower is a multiplication of electrons and photons by cascade process of pair-conversion ($\gamma \rightarrow e^+e^-$) and bremsstrahlung ($e \rightarrow e\gamma$) in the material. The shower constituent loses its energy by multiplication and eventually stops due to energy losses by ionization. The photomultiplier tube (PMT) detect Čerenkov light that is emitted from electrons in the shower. The integrated electric charge from the PMT is interpreted as the energy deposit in the counter.

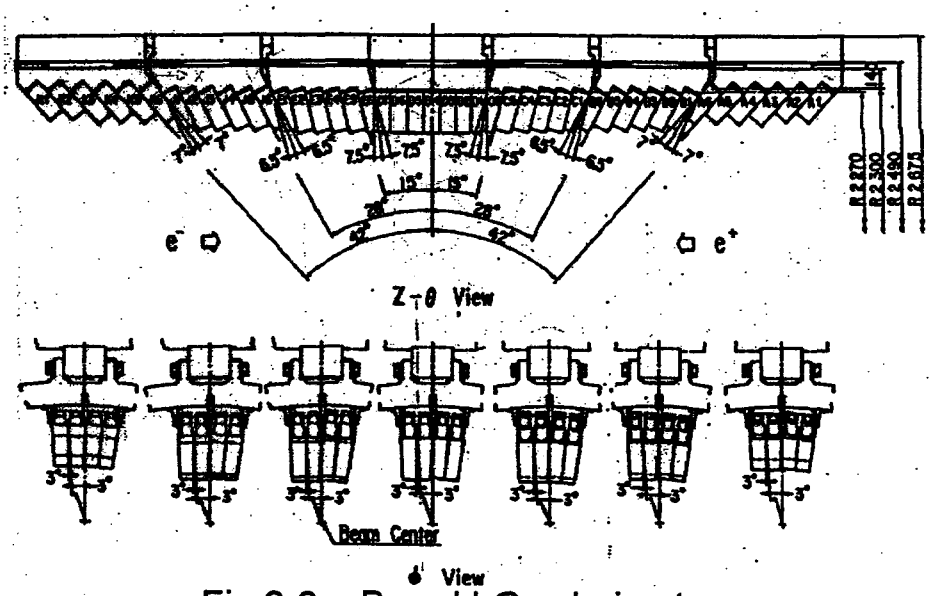

Fig.2-8a Barrel LG calorimeter

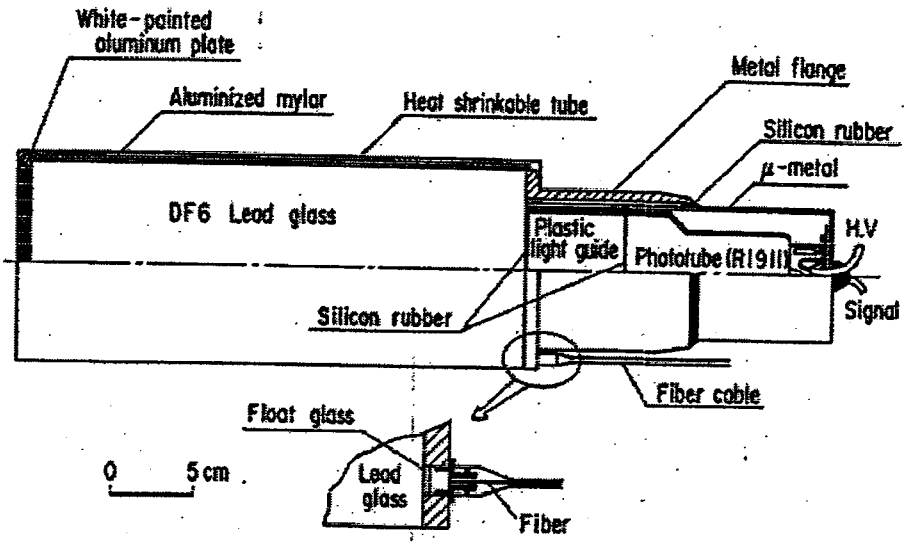

Fig.2-8b LG PMT

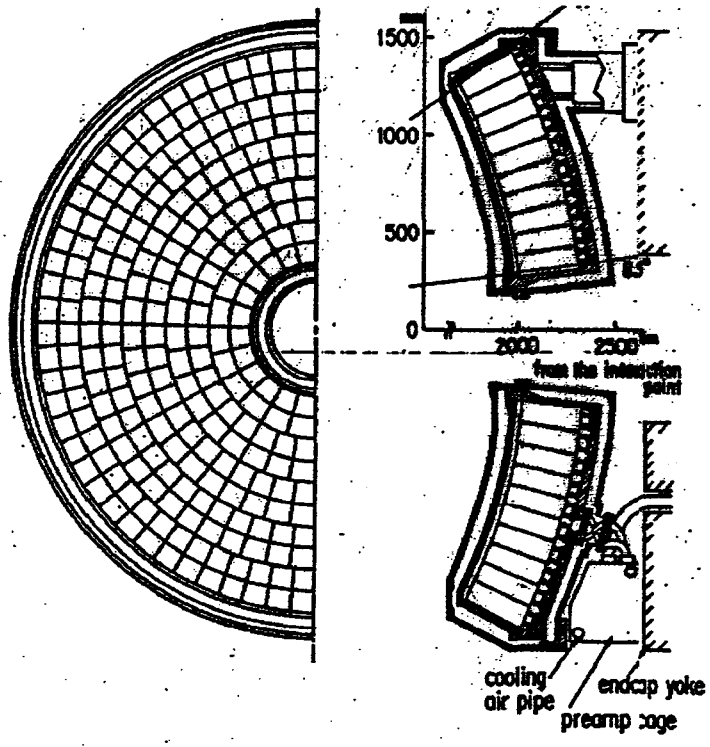

Fig.2-9 Structure of LA calorimeter

End-cap Liquid Argon Calorimeter (LA)

End-cap liquid argon calorimeter (LA)[7] is a sampling electromagnetic calorimeter. The energy is measured by collecting charges from ionization induced by shower particles. LA is placed in the forward region of VENUS. Two liquid argon calorimeters are installed between CDC and end plate and end-cap of the return yoke. Angular coverage of both side LA is $0.79 \leq |\cos\theta| \leq 0.99$. Each calorimeter is divided into twelve sectors. The angle between two sectors is 30° in r-ϕ plane. Each sector is further divided into the inner and outer part subsectors, which have angular ranges of $0.91 \leq |\cos\theta| \leq 0.99$ and $0.79 \leq |\cos\theta| \leq 0.91$, respectively. Fig.2-9 shows the structure of LA. Each detector consists of 480 tower modules that look at a point on the beam axis that is 80 cm off from the interaction point. One tower module consists of 70 calcium-lead plates of 1.5 mm thickness that corresponds to 20.3 X_0. The whole calorimeter is soaked in liquid argon at 86 °K. Each of the calorimeter has 1920 signal readout channels.

Muon Detector

Muon detector is placed outside of the return yoke. It consists of a barrel part and forward / backward parts of drift tubes sandwiched between thick iron absorbers.[8]The barrel part has eight layers of tubes, covering angular region of $|\cos\theta| < 0.69$ and 90% in ϕ. Tubes of inner six layers are parallel to z axis and those of outer two layers are perpendicular to them. The forward / backward parts have four layers of drift tubes covering $0.69 < |\cos\theta| < 0.93$. The total material from inner surface of the york to the 5th layer of the barrel part amounts to at least 5.3 absorption length.

2.2.3. Transition Radiation Detector (TRD)

Transition Radiation

When an ultra-relativistic charged particle (Lorentz factor $\gamma = \frac{1}{\sqrt{1-\beta^2}} \gtrsim O(1000)$) traverses two media of different dielectric constant, X-ray which is called 'transition radiation' is produced at the boundary.(Fig.2-10). The existence of transition radiation was first suggested by Frank and Ginzburg[9] in 1945. Principle of radiation mechanism is the same as Čerenkov radiation. The radiation is considered as result of annihilation of a charge with its image in the conductor. The differential flux of pointing vector(S) is written as follows.

$$\frac{d^2S}{d\theta d\omega} = \frac{2\alpha\theta^3}{\pi}\left(\frac{1}{1/\gamma^2+\omega_1^2/\omega^2+\theta^2} - \frac{1}{1/\gamma^2+\omega_2^2/\omega^2+\theta^2}\right)^2 \qquad (2\text{-}1)$$

where θ is emission angle from the particle direction, ω is frequency of the X-ray, $\omega_{1,2}$ are plasma frequencies of the media and α is fine structure constant. Total energy of the radiation is given as

$$S = \frac{\alpha}{3}\frac{(\omega_1-\omega_2)^2}{\omega_1+\omega_2}\gamma \cong \frac{\alpha}{3}\gamma\,\omega_1 \quad (\text{for } \omega_1 >> \omega_2) \qquad (2\text{-}2)$$

These equations suggest three things.

1. Total energy of the transition radiation is proportional to Lorentz factor γ of the charged particle
2. Radiation peaks at very forward angle ($\theta \sim 1/\gamma$).
3. Strength of the transition radiation from one boundary is so small as $\sim O(\alpha = \frac{1}{137})$. This means that multi layers of media boundary are needed for a practical use.

Fig.2-11 shows a spectrum of the transition radiation at the single boundary between polypropylene (ω_1=20eV) and helium (ω_2=0.28eV). For example, the average of the total energy is 28 keV with 600 boundaries for electron whose momentum is 2GeV/c using equation(2-2). (It is not strict, because there are interference of X-rays which is called as 'Formation zone effect'[10].) A practical transition radiation detector system we designed has multi layers of the media and X-ray detector as shown in Fig.2-12b.

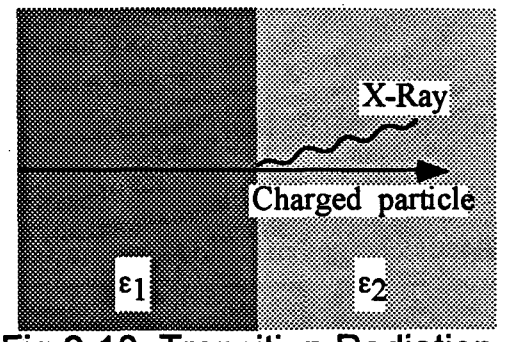

Fig.2-10 Transition Radiation

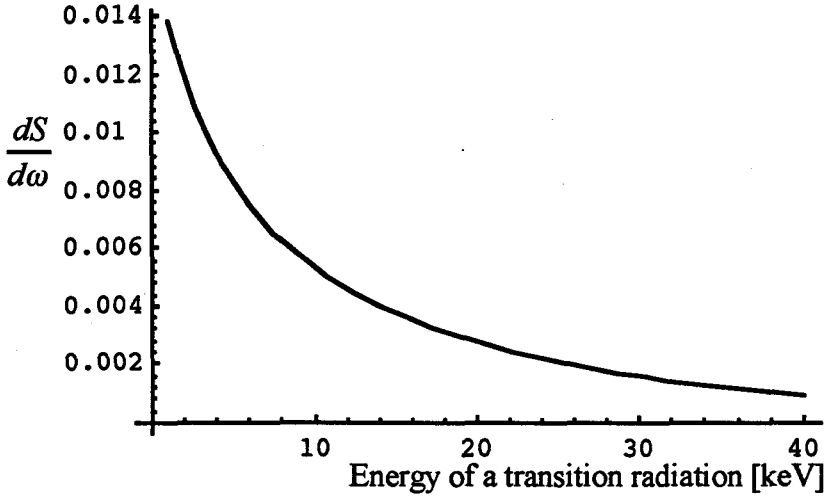

Fig.2-11 Spectrum of Transition Radiation

Structure of TRD

TRD has large cylindrical structure as shown in Fig.2-12a. It is made of two parts. One is a airtight 'radiator box' which contains radiative material and helium gas. Other is a X-ray chamber filled with xenon gas to detect the transition radiation. TRD is divided into eight octants. Each octant has 4 layers of the radiator box and X-ray chamber combination. The detector is divided into 32 sets of radiators and chambers. The structure is composed of a pair of endplates (15mm thick aluminum), inner and outer cylinder (3.0mm thick, ϕ=2540mm, 3114mm aluminum) and eight side-panels. The side-panel which separates octants consists of 13.8mm thick aluminum honeycomb with 0.6mm aluminum skin on each side. There are windows that separate radiators and chambers. The X-ray chamber is composed of an aluminized mylar sheet as the window on innner surface and an aluminum plate on the outer surface to separate itself from the next radiator. In the middle, anode wires are strung along z axis between two end plates. The total radiation length of TRD is set to be $0.18X_0$ (Aluminum $=0.13X_0$ + radiator$=0.05X_0$).

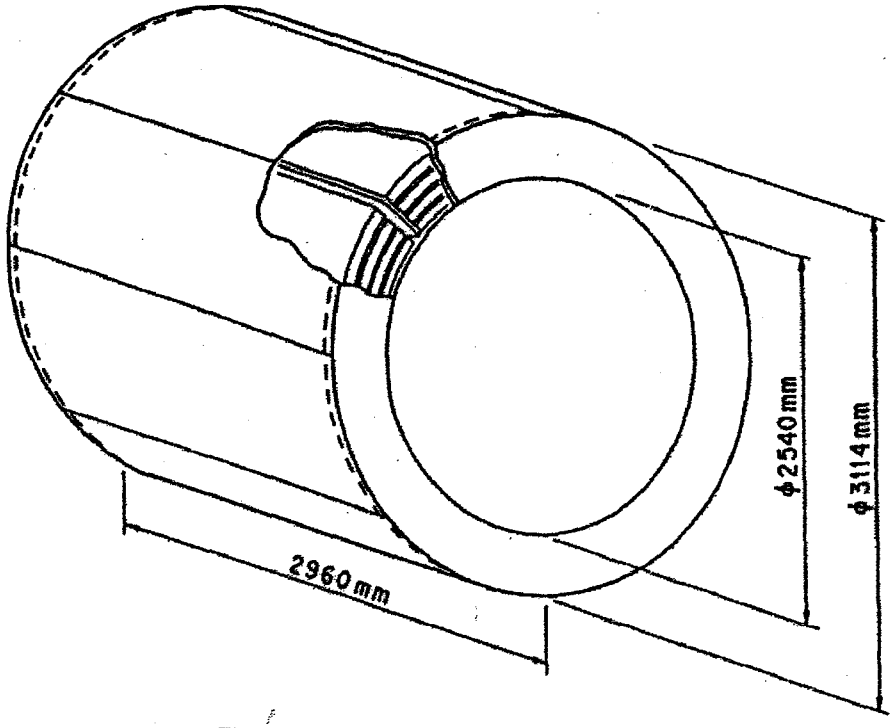

Fig.2-12a TRD Over View

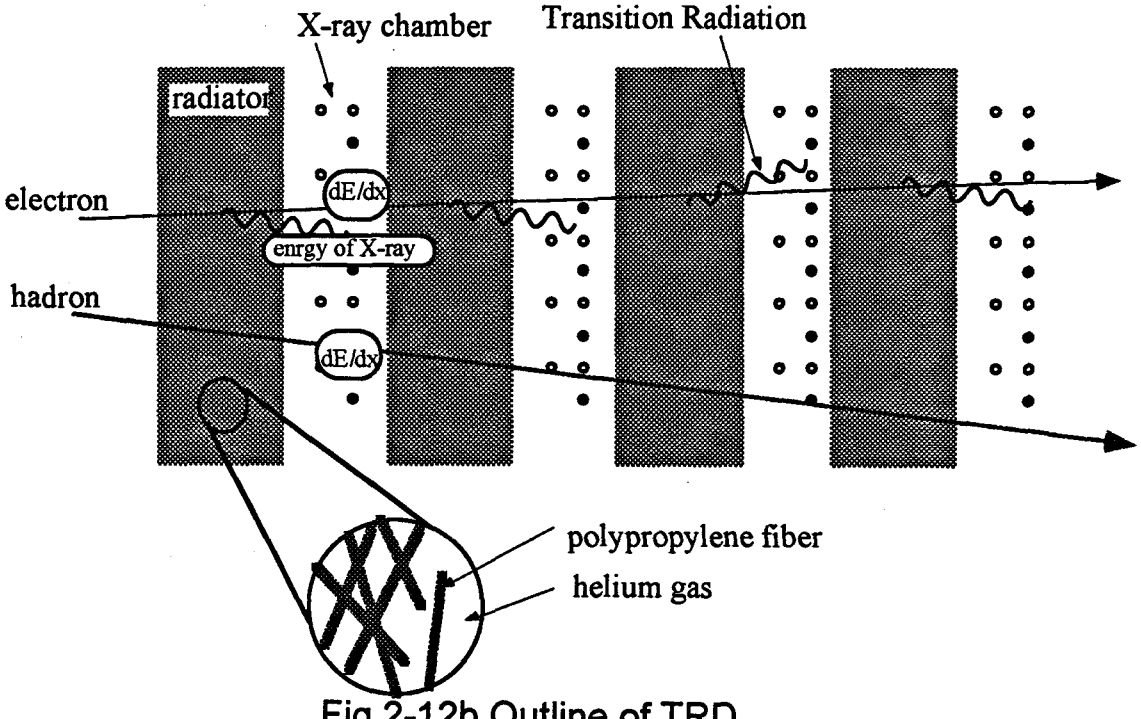

Fig.2-12b Outline of TRD

A schematic illustration of TRD mechanism. All charged particles deposit energy in X-ray chambers. However, only an ultra relativistic charged particle (electron) emits photons in the radiator and it is detected by X-ray chambers.

Radiator Box

Fig.2-13 shows the structure of the radiator box. The radiator box consists of an aluminum shell, two endplates, two ribs, three sets of radiators and a "window". The radiator is made of the polypropylene fibers (ϕ=18μm), compressed to have the density of 0.12g/cm^3. The thickness of the radiator is 45±1 mm.

The "window" is made from the 3 mm thick polymethacrylimide rigid form (Rochacell-31) reinforced by a 25 μm thick Mylar and a 25 μm thick aluminized Mylar on each side. It serves to seal gas contained inside. It should be as thin as possible not to absorb X-rays from the radiator. It should take a uniform shape, namely, the distance to anode wires has to be the same everywhere. Every small deformation leads to a non-uniform gas gain.

The boxes are filled with Helium gas. It is chosen for its smallest plasma frequency (ω_p=0.28eV) and its small absorption of X-ray. The gas flows at a rate of ~300cm^3/min. Pressure of the radiator box is kept at atmospheric pressure. Helium can easily permeate into polymethacrylimide rigid form of window and the inner pressure of it slightly increase. Moreover, helium gas permeate into X-ray chambers, too. To prevent the rigid-form bulge and suppress the contamination of helium in the chambers, it is kept at slightly lower pressure than atmospheric by pumping from both ends of the window through a small tube.

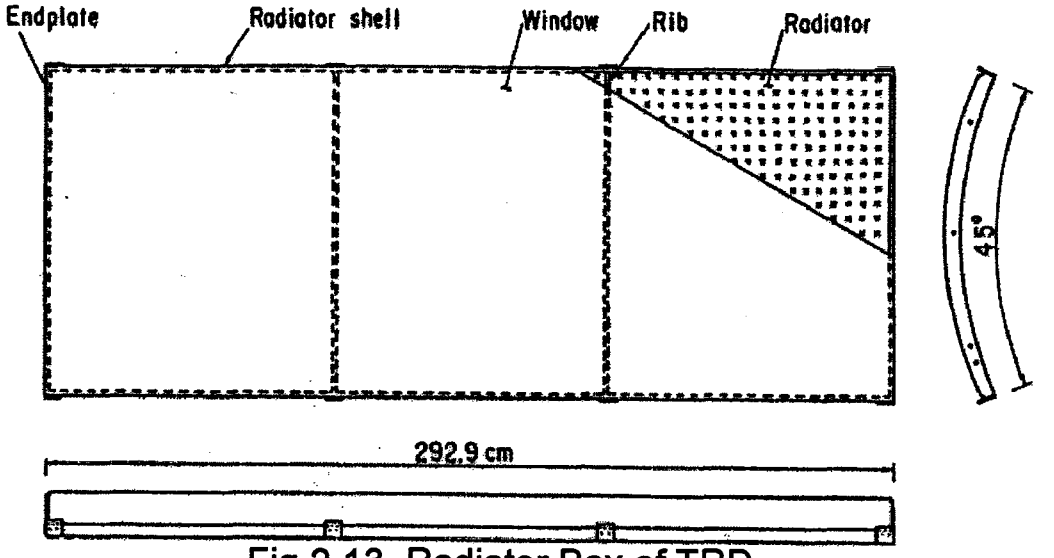

Fig.2-13 Radiator Box of TRD

X-ray Chamber

The X-ray chamber consists of aluminized Mylar cathode plate (at -300V) which is actually the outer wall of the radiator box, aluminum plate of the radiator shell (kept at the ground level potential =GND) and wires. There are three types of wires; sense wire, potential wire and grid wire. They are kept at electric voltage of +1740V, +200V, GND respectively. The structure of the chamber cell and drift path of the electron is shown in Fig.2-14. Total number of sense wires and field wires are 2688 and 5504. Specification of the wires are shown in Table 2-2. The drift path is estimated by a simulation under a magnetic field of 0.75 T taking Lorentz angle into account.

Xenon gas is efficient for the X-ray detection because of its short absorption length. TRD uses Xe (90%) + CH_4 (10%) gas. The accuracy of the methane mixture is controlled within ±0.5%. The total gas volume is 2.3 m^3. Since xenon gas is

expensive, a closed gas circulation system is used for the X-ray chamber. Circulation rate is about 3 ℓ/min. The pressure of the chamber is maintained at 25±5 mm water above atmospheric pressure.

Signals from the sense wire is amplified by a charge-sensitive preamplifier mounted on the endplate. Preamplifier signals are sent through a set of individually shielded 16 twisted-pairs cables to a TKO-ADC(*) module in pseudo-differential mode. There are cables also for power transmission and for calibration pulse transmission. Signals are digitized by ADC and the data are sent to a data acquisition (DA) system.

Note: (*) TKO is a KEK standard electronics.

Table 2-2 Wire specifications of TRD

	Sense wire	Potential wire	Grid wire
Voltage	+1740 V	+200 V	GND
Material	Gold-plated tungsten with 3% rhenium	Gold-plated copper-beryllium	
Diameter	30 μm with ±2% weight tolerance	107 μm	
Weight/cm	1.35×10^{-4}g/cm	7.2×10^{-4}g/cm	
Tension	90 g	280 g	
Sag Gravitational	160 μm	280 μm	
Sag Electric force	≤ 14 μm	≤ 5 μm	

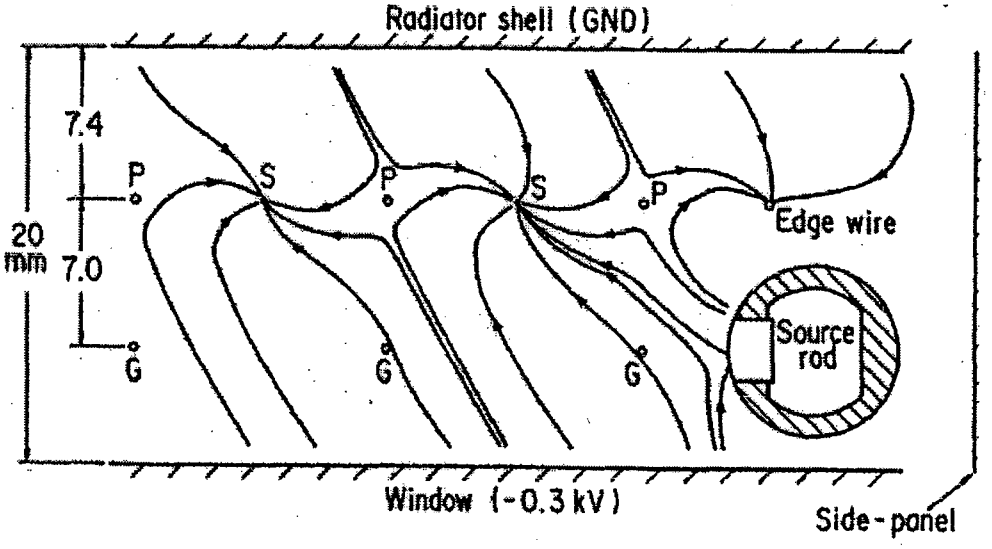

Fig.2-14 Structure of TRD chamber cell

Gain Monitor & TRD On-Line System

The purpose of TRD on-line system is to control high voltage, to monitor chamber gas gain, to supervise pressures and temperatures of the detector and gas circulation system. The gas gain change of as large as ±20% is expected for long experimental period, due to the change in the atmospheric pressure, gas composition etc (See Fig.2-15). To keep gas gain constant or measure it during experiments, TRD on-line system control the high voltage of anode wire of X-ray chamber and measure spectrua of ^{55}Fe X-ray sources (5.9keV) which are placed at the end of each chamber. It is called as 'gain monitor'.

Variation of gas gain with time is constantly corrected with ^{55}Fe spectrum. Further more on-line system can optimize the high voltage to keep the gas gain variation within ±1%. Details of the method of the gain correction in the software analysis will be described in the chapter-4 in detail.

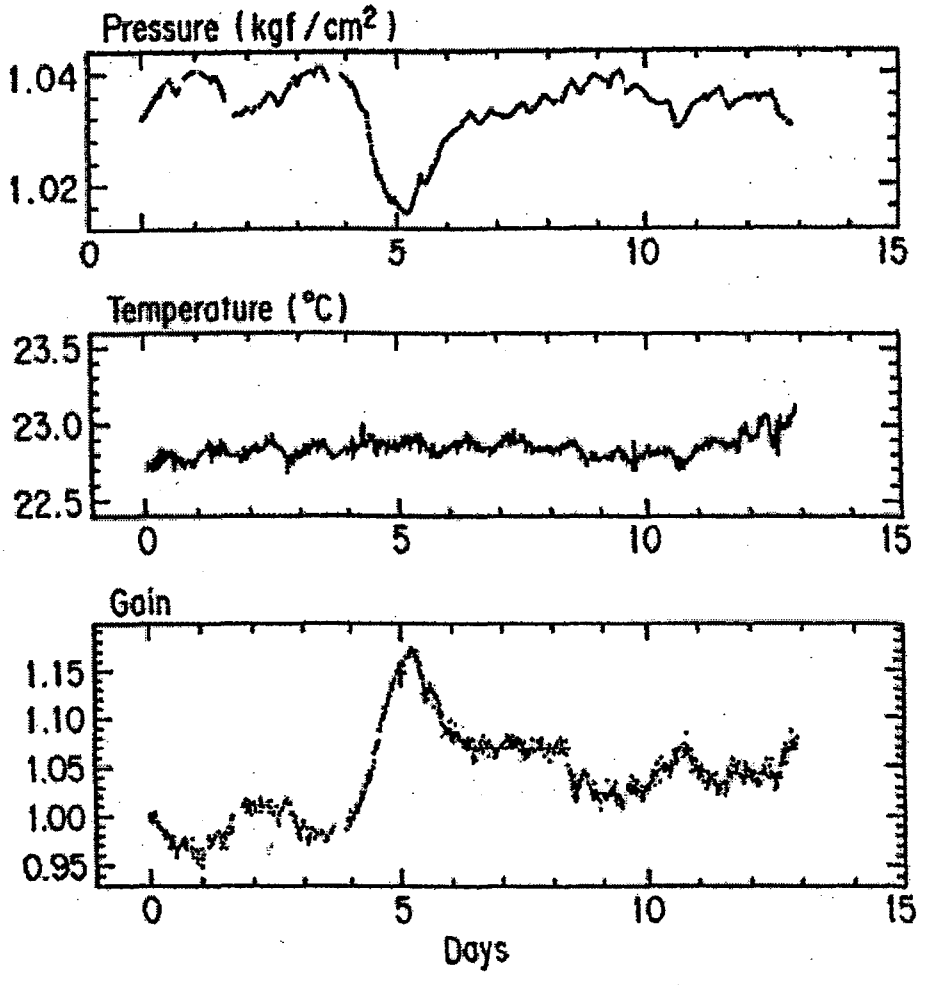

Fig.2-15 Typical Example of the Gain Variation of Pressure and Temperature in TRD

2.2.4. Data Acquisition

In TRISTAN MR, electron and positron bunches collide every 5 μsec. A trigger and data readout system are needed to get all physically significant events and to reduce backgrounds.

VENUS data readout system starts to record the detector signals at every e^+e^- collision. If there is no trigger, then a "First Clear" signal is sent to clear data buffer before next colliding. The data readout system is stopped and data buffer is cleared. When the trigger system decides to record an event as physically interesting phenomenon, it masks the First Clear signal and the data collection system starts automatically.

Trigger System

VENUS trigger system is composed of the first and second level trigger. The first level trigger is designed to work between beam crossings and the second level trigger includes software program.

The First Level Trigger

The first level trigger is a fast hardware logic that takes less than 5 μsec before the next "First Clear" signal. There are two types of triggers in first level in VENUS. One is a neutral trigger using energy information in calorimeters. The other is a charged track trigger defined by CDC information.

1. Neutral trigger

(a) LG total energy sum trigger
A total energy deposit in LG is larger than 4 GeV.

(b) LA total energy sum trigger
At least one side of LA has a total energy deposit larger than 6 GeV.

(c) LA sector sum trigger
At least one of the sectors of LA has a energy deposit larger than 2.5 GeV

(d) Active Mask trigger
Active Mask has energy deposit larger than 10 GeV in a back-to-back configuration. This trigger is provided for small angle Bhabha events. The result of this trigger is used to monitor luminosity on real-time basis.

2. Charged trigger

(a) Coplanar trigger
At least one pair of tracks with transverse momenta to the beam axis larger than 0.7 GeV/c in a back-to-back configuration is found by the track-finding modules. The trigger requires that the r-ϕ angle between the two tracks is larger than 120 degree.

(b) LG segment sum trigger
At least one of LG segments has an energy deposit larger than 0.7 GeV and at

least two tracks have transverse momenta larger than 0.7 GeV/c. In this trigger, there is no requirement for the track configuration.

(c) Two-track-limited (TTL) trigger
TTL trigger is necessary to have a large acceptance for an event which has some tracks in opposite direction. It requires the existence of a track with an angle from the opposite direction of the other track smaller than 60 degree.

Moreover, random trigger is made at the rate of 0.1 Hz to monitor accidental backgrounds.
These trigger signals are processed by a trigger decision module which looks at a preprogrammed memory table as areference.

The second-level trigger

TTL and coplanar events in the first-level trigger contain large backgrounds such as beam-pipe or beam-gas collision. The second-level trigger is a software trigger to reduces about 50% of backgrounds in it by using several track finding conditions. The trigger rate with requirement of first and second level is typically 5 Hz and dead time of the trigger system is 10% but it strongly depends on the beam conditions.

Data Read Out System

VENUS data acquisition system[11] has a tree-like structure as shown in Fig.2-16. There are more than 30,000 readout channels which amount to a data size of 5 k byte per event. Signals from detector components are processed at the front-end electronics. Most of digitized data are sent to on-line system computers through an interface. Some of the data collected and analyzed by a local computer within each detector component are sent to the on-line system through the network. The on-line system controls the data acquisition and monitors the data status.
A typical data acquisition time of one event is 28 msec. The collected data are sent to the main frame computer through optical fibers and are stored in a magnetic tape library.

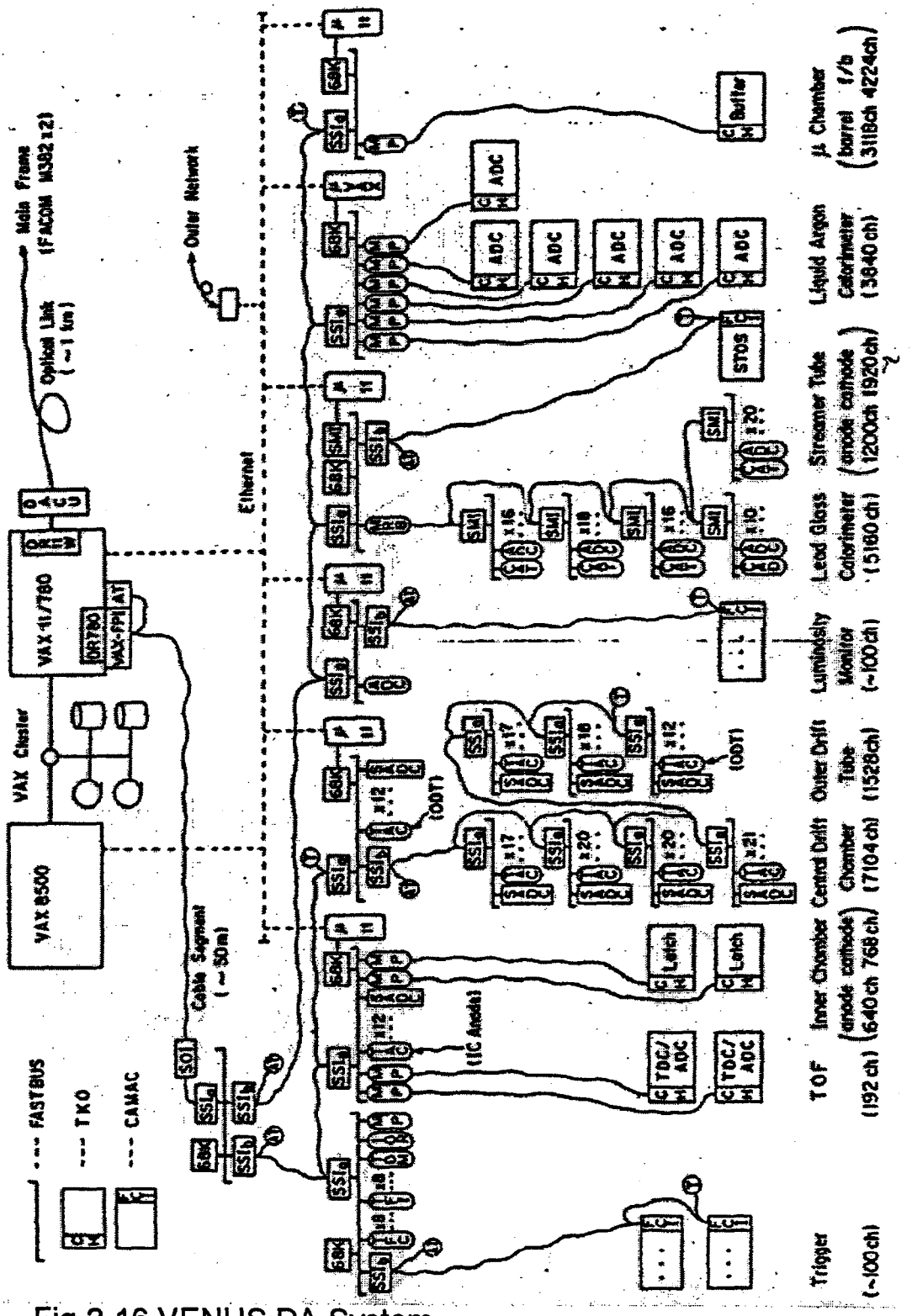

Fig.2-16 VENUS DA System

2.2.5. Luminosity Measurement

Luminosity L is a measure of the intensity of the beam. It is related to a number of events N and cross section σ by

$$N = \sigma \int L\, dt \qquad (2\text{-}3).$$

It can also be expressed as

$$L = \frac{I_{e^+} I_{e^-}}{4\pi f_{rev}\, n_b\, e^2\, \sigma_x\, \sigma_y} \qquad (2\text{-}4).$$

where I_{e^+}, I_{e^-} are current of the electron and positron beam, f_{rev} is revolution frequency of the beam, n_b is number of bunches in the beam, e is magnitude of the electric charge and σ_x, σ_y are horizontal and vertical beam sizes.

Experimentally, the luminosity is usually measured using a well-known process with large cross section. In VENUS, the number of Bhabha scattering ($e^+e^- \rightarrow e^+e^-$) events are counted by LG, LA and Active Mask during the experiments.

References

[1]TRISTAN Project GGroup, 'TRISTAN Electron-Positron Colliding Project', KEK report 86-14(1986)

[2]VENUS Collab., KEK Report TRISTAN-EXP-001(1983)

[3]Y.Yamada et al., KEK-Preprintt-92-166, submitted to Nucl.INstr.Meth.

[4]Active Mask reference

[5]R.Arai et al., Nucl.Instr. and Meth. **A217**(1983)181

[6]M.Sakuda et al., Nucl.Instr.Meth. **A311**(1992)57

N.Terunuma et al., Nucl.Instr.Meth. **A323**(1992)471

J.Haba et al., Nucl.Instr.Meth. **A303**(1991)346

Y.Fukushima et al., KEK-preprint-92-162, submitted to IEEE 1992 Nuclear Science Symposium, Florida, Oct.25-31, 1992.

[7]Y.Fukushima et al., IEEE Trans.Nucl.Sci. **36**(1989)670

[8]Y.Asano et al., Nucl.Inst.Meth. **A254**(1987)35

[9]I.Frank V.Ginzburg, J.Phys.(Moscow),5,353(1945)

[10]M.H.Saffouri. IL Nuovo Cimento 5D,N2(1985)175

L.Durand, Phys.Rev. D11(1975)89

X.Artru et al., Phys.Rev. D12(1975)1289

[11]K.Amako et al., VENUS Offline Note 002(1987)

Chapter 3
Event Reconstruction & Data Reduction

For physics analysis, raw data must be processed to reconstruct physical quantities such as tracks, energy etc... of particles. Then reconstructed events have to pass a series of filters to reduce backgrounds and to select desired signals. In this chapter, at first a method to reconstruct events from raw data is given, then selection of desired events using various physics requirements are described.

3.1. Event Reconstruction

Event reconstruction consists of two steps. In the first step, raw data are converted to physical quantities by using calibration parameters of the detector. For example, TDC (Time to digital converter) outputs are converted to drift length of CDC cell, ADC counts to energy deposits in LG modules and so on. In the second step, informations on physical objects such as tracks or electromagnetic showers are extracted. In the following, we give mainly reconstruction techniques of charged tracks in CDC and electromagnetic shower clusters in the calorimeters. These are major and most important informations for the event analysis.

3.1.1. Charged Track Reconstruction

In order to recognize charged particles and to measure their momentum, trajectories of the charged particles must be reconstructed from CDC hits. They are carried out in both the r-ϕ plane and r-z plane. The reconstruction procedure is called PERPR[1].

A trajectory in r-ϕ plane is expected to be an arc in a uniform magnet field. It is obtained by fitting hit points to a semi-circle. At least six hit points were required to lie within an allowed deviation from the reconstructed trajectory. The transverse momentum to the beam axis $p_\perp$ is decided by its curvature. Then z coordinate is obtained using slant wire hit information as,

$$z = \frac{\ell}{2} - \frac{d}{\tan\alpha} \qquad \ldots(3\text{-}1).$$

with ℓ the slant wire length, d the distance between the axial trajectory and the slant hit position along the z-axis and α the slant angle (+3.3 or -3.3 degree). The trajectory is expected to be a straight line in the r-z plane. Combining r-ϕ and z information, a three-dimensional track is obtained where at least three slant wire hits are required. Charged particles in the range of $|\cos\theta| \leq 0.75$ can cross all axial and slant layers of CDC. Geometrical parameters of the track are illustrated in Fig.3-1. Criteria of these parameters for the track selection are given in the following section. The resolution of the charged track is dependent on the particle momentum. The spatial resolutions of the high momentum track are given as

$$\sigma_{vtx}(r\text{-}\phi) \simeq 460\ \mu m$$
$$\sigma_{vtx}(z) \simeq 6.7\ mm \qquad \ldots(3\text{-}2)$$

where the contribution of multiple coulomb scattering is very small. The angular resolution in azimuthal and polar angle are estimated as

$$\sigma_\theta = 9 \sin^2\theta \quad mrad$$
$$\sigma_\phi = \quad 1.3 \quad mrad \qquad \ldots(3\text{-}3).$$

Momentum resolution is derived from these relations. At the magnetic field of 0.75T, the resolution of the transverse momentum $\sigma_{p_\perp}$ is as follows.

$$\frac{\sigma_{p_\perp}}{p_\perp} = \sqrt{(1.3\%)^2 + (0.8\% \times p_\perp)^2} \qquad \ldots(3\text{-}4)$$

where $p_\perp$ is measured in GeV/c. The reconstruction efficiency of high $p_\perp$ tracks ($|\cos\theta| \leq 0.75$) is better than 99.9% in the r-ϕ plane and 98.0% in the r-z plane for isolated track with slightly lower value for those in jets. Typically, the efficiency in the core of the jet in multihadronic events is 93% for $|\cos\theta| \leq 0.68$. The estimation of the reconstruction efficiency in the hadron jet is given in Chapter-4.

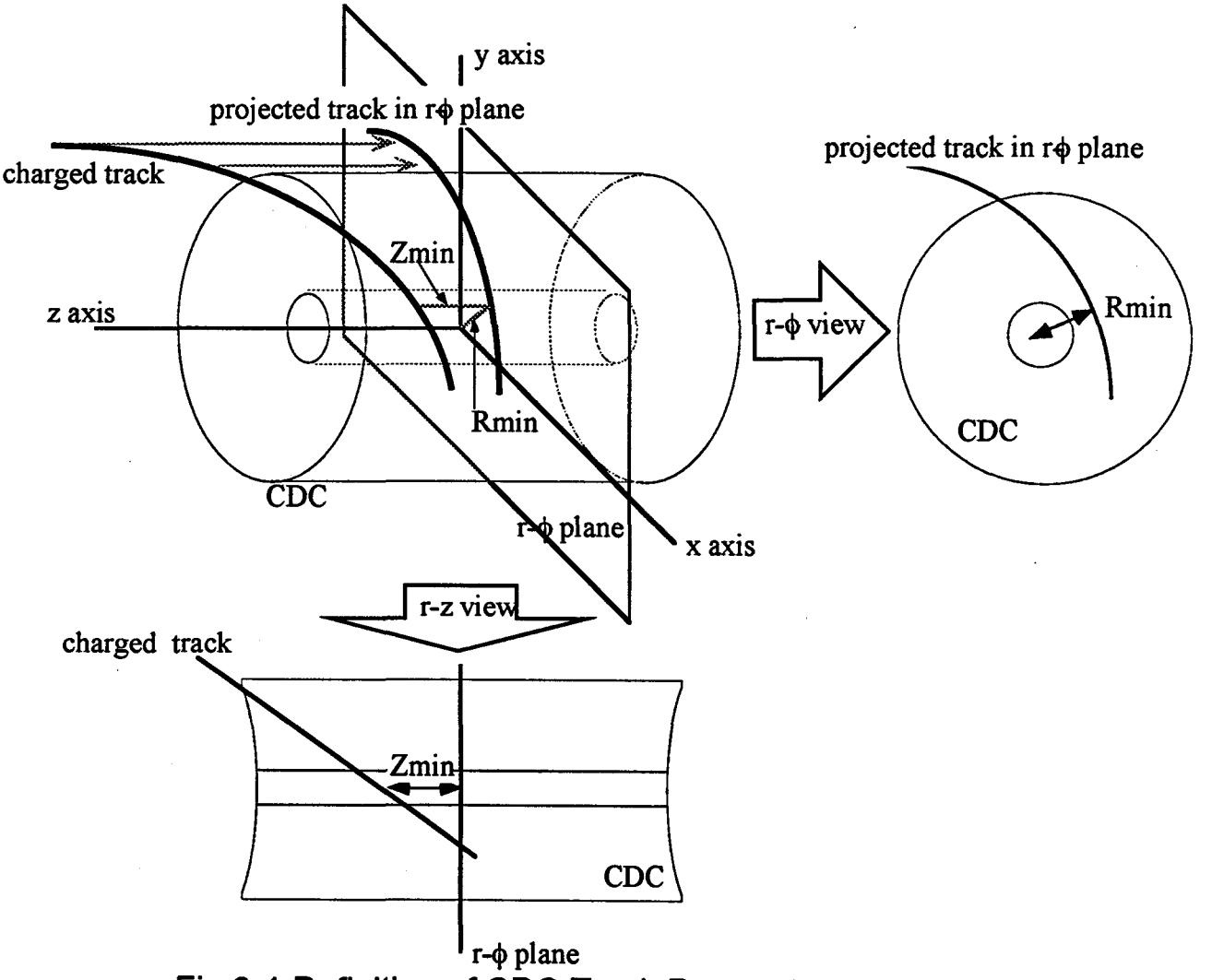

Fig.3-1 Definition of CDC Track Parameters

3.1.2. Cluster Reconstruction

An electromagnet shower in the calorimeter generally spreads over some neighboring modules or cathode pads. To derive total energy and incident points of a particle, a clustering method which regroup such neighboring hit modules is adopted.

LG Clusters

The spread of the energy deposit of electromagnetic shower can be expressed[2] as

$$\frac{dE}{dx} = \frac{E}{\lambda} \exp\left(-\frac{|x-x_0|}{\lambda}\right) \quad \ldots(3\text{-}5)$$

where x is the distance in a coordinate perpendicular to the incident direction, x_0 is incident position, λ is a constant (=1.0cm) that characterizes lateral spread of the shower (See Fig.3-2).

Each module in a cluster must adjoin to other side by side. The "cluster" is decided as follows.

1. Start with a module that has the largest energy deposit ($E_{parent.}$) (called as a 'parent'), search for an energy deposit in neighbor modules.

2. If a module adjacent to the 'parent' has a energy deposit ($E_{daughter}$), it is recognized as a 'daughter'. There may be more than one daughter. The daughter(s) and the parent form a family.

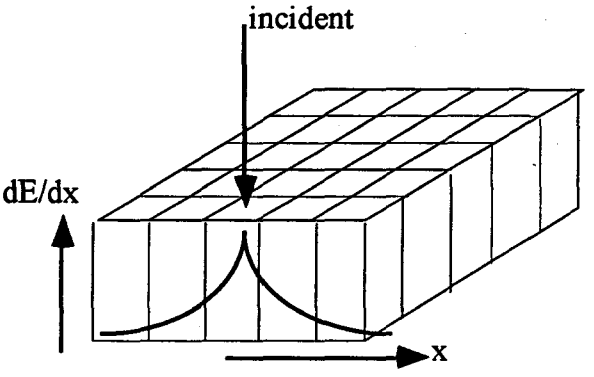

Fig.3-2
Energy deposit in LG calorimeter

3. Find a 'grand child' around the 'daughter' module. The energy deposit of 'grand children' module should be consistent with at least one of following conditions.

(a) $E_{daughter} > \frac{E_{parent}}{5}$, ...(3-6a)

(b) The energy deposit E of the ground children

$$E < \frac{E_{parent}}{2}$$

and $E < 3\, E_{daughter}$, ...(3-6b)

4. Find a 'great grand child' in the neighbor of 'grand children' with conditions (3-6) using $E_{grand\ child}$ instead of $E_{daughter}$. All of the grand children and great grand children are added to the family.

5. If no more 'great grand ... child' can be found, the family thus grouped for make a cluster.

6. After removing modules which belong to the cluster, the step 1 to 5 are repeated for the remaining modules to form another cluster.

7. Step 6 is repeated untill all of the hit modules are clustered.

The energy of a cluster E [GeV] is sum of all energy deposits in the modules within the cluster. The energy resolution of LG calorimeter is studied by using Bhabha scattering event. It is given as

$$\frac{\sigma_E}{E} = \frac{5.4\%}{\sqrt{E}} + 2.8\% \qquad \ldots(3\text{-}7)$$

The cluster center $x_{cluster}$ is energy weighted mean of x_i's where x_i is the coordinate of its module in the cluster.

$$x_{cluster} = \frac{\sum_i E_i^{\alpha} x_i}{\sum_i E_i^{\alpha}} \qquad \ldots(3\text{-}8)$$

Here, the weight E_i is the energy deposit in the module and the constant value α is tuned as 0.34 by Monte Carlo program EGS4[3] to give the most accurate incident point of a particle.

LA Clusters

The clustering method of LA is similar to that of LG. The lateral shower spread in LA can be expressed as a sum of two exponential terms. The energy resolution of LA calorimeter is studied by using Bhabha scattering event. It is given as,

$$\frac{\sigma_E}{E} = 1.6\% + \frac{10.2\%}{\sqrt{E}}, \qquad \ldots(3\text{-}9)$$

where E is measured in GeV.

3.2. Data Reduction

3.2.1. Standard Multihadronic Event Selection

Our primary interest is selection of $e^+e^- \rightarrow q\bar{q}$ event. In the final state of this event, quarks fragment and become hadron jets. Multihadronic events are characterized by many charged tracks, large energy deposit in the calorimeters and small missing momentum along the beam direction.

Following five conditions are standard VENUS hadron cuts to select multihadronic events.

1. Total energy deposit in the calorimeter $E_{cal} > 5$ GeV
   E_{cal} is the sum of the energy deposit in the region of $|\cos\theta| < 0.89$.

2. Number of good track $N_{good} > 5$
   A 'good track' means a well reconstructed charged track in CDC. The condition of the good track is as follows.

$$\left.\begin{array}{l} N^{hit}_{axialwire} \geq 8 \\ N^{hit}_{slantwire} \geq 4 \\ |R_{min}| < 2 \text{ cm} \\ |Z_{min}| < 20 \text{ cm} \\ |\cos\theta| < 0.85 \\ p_{\perp} > 0.2 \text{ GeV/c} \end{array}\right\} \quad \ldots\ldots (3\text{-}10)$$

   The meaning of each parameter is explained in Fig.3.1.

3. Visible energy $E_{vis} > E_{beam}$ beam energy
   E_{vis} is the sum of cluster energies in the calorimeters and momenta of good tracks.

4. longitudinal momentum balance $P_{bal} \leq 0.4$

   where $P_{bal} = \dfrac{|\Sigma p_z|}{E_{vis}}$

5. At least one of the jet mass should be larger than 3 GeV/c^2
   The jet mass means the invariant mass of a group of particles in one of the two hemisphere divided by a plane perpendicular to the thrust axis. In calculating the invariant mass, charged particles are assumed as π and neutrals as photons. This cut is effective for the rejection of τ-pair production.

Note: 'Thrust' axis is one of variables which are frequently used in the jet analysis to define a primary quark direction. We use 'thrust' axis instead of quark direction (See Chapter5) and 'jet clustering' to recognize hadron jets in multihadronic final state. Definition and detail of them are given in Appendix-2.

Fig.3-3 shows distributions of some parameters of real data and expectation of multihadronic events. The detector acceptance of VENUS using these criteria for 5-flavor multihadronic event at $\sqrt{s}$ = 58 GeV is 75.1 ±0.5 %. For the semileptonic decay event of b and c quark, the acceptance is 79.3 ±1.1%. These are estimated by Monte-Carlo simulation of multihadronic final state (JETSET7.3)[4] using VENUS detector configuration.

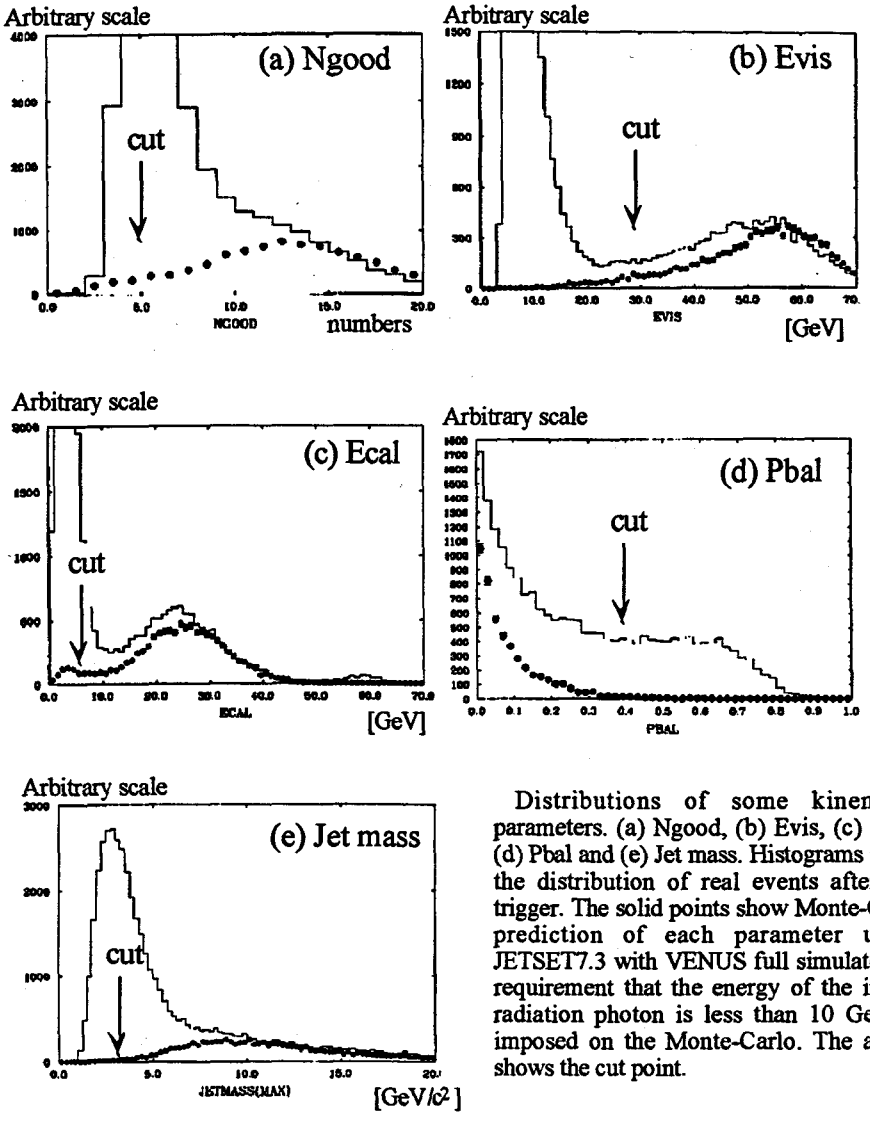

Distributions of some kinematic parameters. (a) Ngood, (b) Evis, (c) Ecal, (d) Pbal and (e) Jet mass. Histograms show the distribution of real events after the trigger. The solid points show Monte-Carlo prediction of each parameter using JETSET7.3 with VENUS full simulator. A requirement that the energy of the initial radiation photon is less than 10 GeV is imposed on the Monte-Carlo. The arrow shows the cut point.

Fig.3-3 The cutting parameters of hadron selection

3.2.2. Bhabha & Two Photon Event Rejection

In addition to hadronic events, There are additional events coming from Bhabha, two-photon ($e^+e^-\rightarrow e^+e^-\gamma\gamma$ and $\gamma\gamma\rightarrow X$, See Appendix-1) and hard photon radiation ($e^+e^-\rightarrow q\bar{q}\gamma$). Contamination of these events is less than 1% in multihadronic event sample[5]. However, when we select events that have an inclusive electron, they become a significant fraction in the sample. Therefore, we must impose further criteria.

Events which should be rejected look like those in Fig.3-4. For Bhabha events, an electron occasionally radiates a photon and it converts to an electron positron pair in the material as shown in Fig.3-4a. In this case, the numbers of charged tracks increase up to five or six. In most two-photon events, electrons go forward and are missed in the beam pipe. Occasionally, however, one or two electrons are tagged in the detector as Fig.3-4b. Fig.3-4c shows an example of a multihadronic event with hard photon radiation.

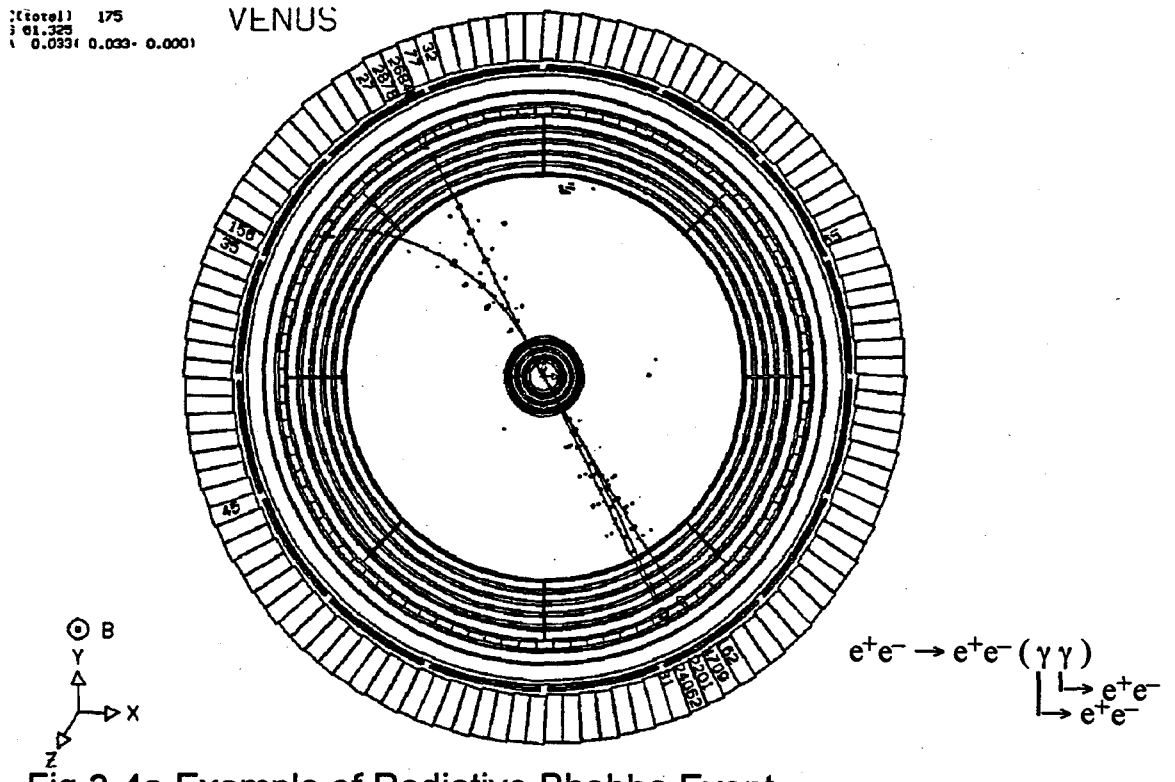

Fig.3-4a Example of Radiative Bhabha Event

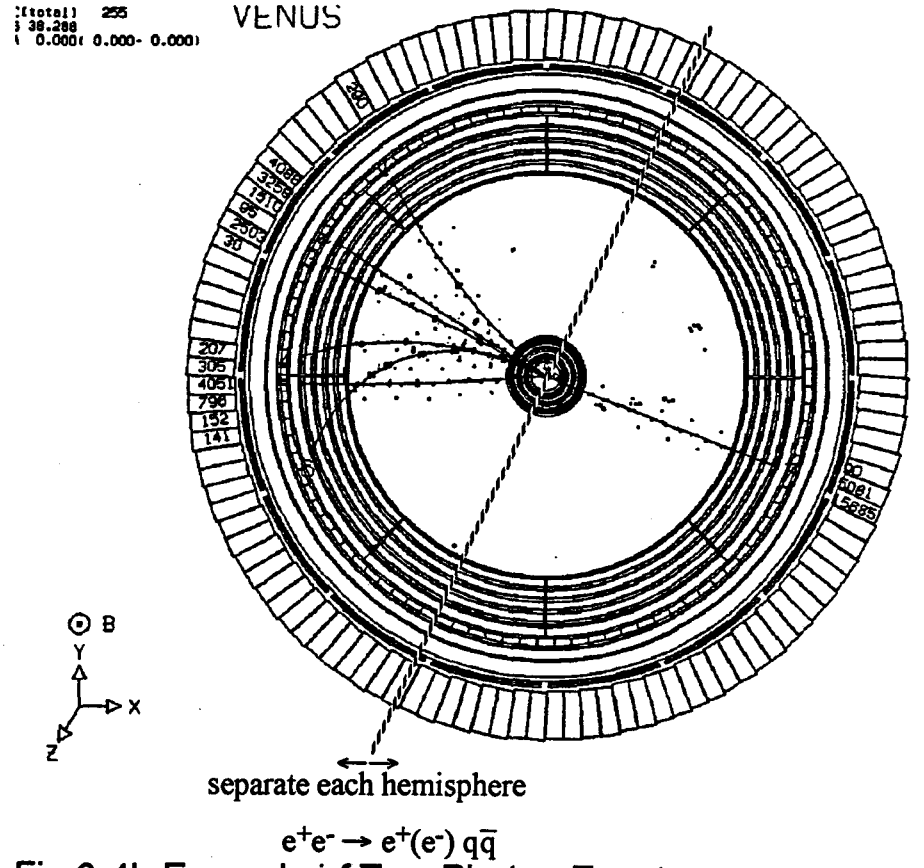

$e^+e^- \rightarrow e^+(e^-)\, q\bar{q}$

Fig.3-4b Example of Two Photon Event

Only one electron candidate is found in one of the event hemisphere.

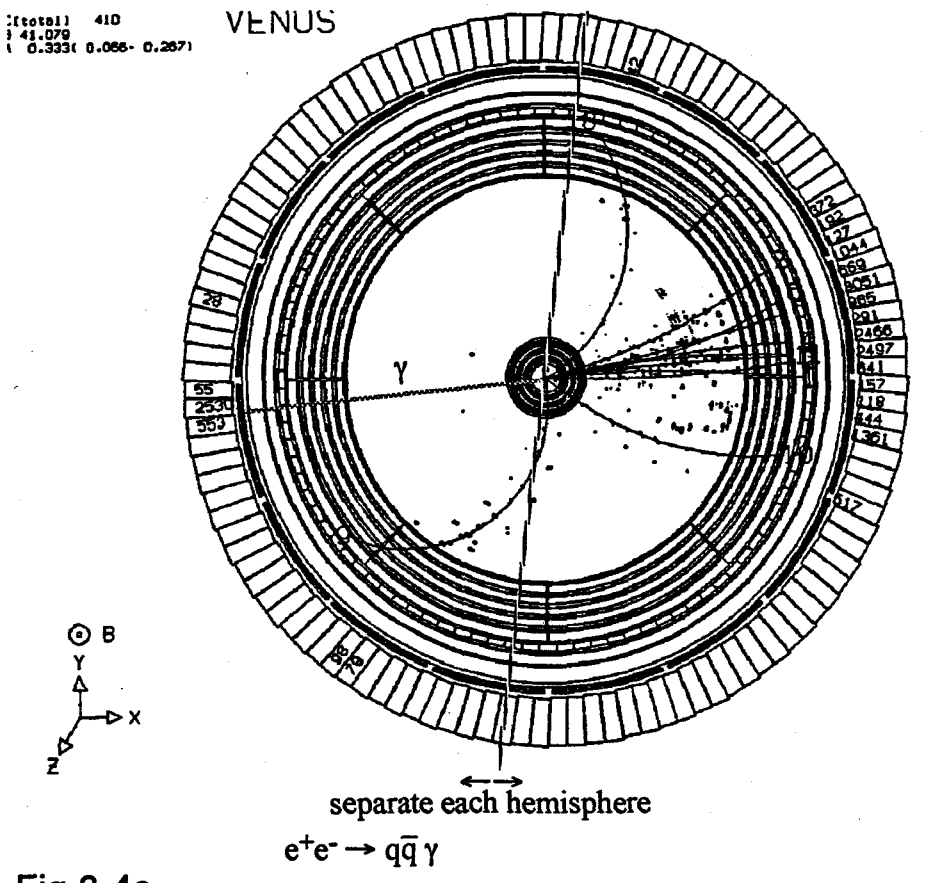

Fig.3-4c
Example of Multihadronic Event with Hard Photon Radiation
No charged tarck and only energy deposits are found in one of the event hemisphere in 3-dimension.

The rejection criteria are follows.

1. There are two clusters on LG or LA whose energy is larger than 15 GeV and there exists an associated charged track to each cluster.
(rejection of radiative Bhabha events) (Fig.3-4a)

2. There is only one charged track in one of the hemisphere and its $\frac{E}{p}$ larger than 0.7. $\frac{E}{p}$ is the ratio of the energy deposit E of a cluster which associates to the charged track and p is its momentum. (rejection of electron tagged two-photon event) (Fig.3-4b)

3. There is no charged track in one of the hemisphere.
(rejection of hard radiation events) (Fig.3-4c)

Events which satisfy one of these condition, are rejected. The efficiency of these criteria for the desired events is shown in Table 3-1 with that of the standard multihadronic event selection.

In the experiment with TRD operation, we got $\int Ldt = 74.6 \pm 0.5 \pm 1.9\ pb^{-1}$, and 9791 events are selected as a result of the standard multihadronic event selection. After Bhabha & two-photon event rejections, total of 9437 events remained.

Table 3-1 efficiency of hadronic event selection

	5-flavor	Semielectronic decay event of b and c quarks
Standard multihadronic event selection	75.1 ±0.5 %	79.3 ±1.1%
Bhabha & two-photon event rejection for the standard multihadronic event	97.8 ±0.7 %	98.0 ±1.4%
Total acceptance	73.4 ±0.5%	77.7 ±1.1%

Reference of this chapter

[1]Y.Nakagawa et al., Jpn.J.Appl.Phys. **25**(1986)1049

[2]G.A.Akopdjanov et al., Nucl.Instr.and Method **140**(1977)441

[3] T.Kamitani, Ph.D.Thesis, Osaka University (1989)

[4]T.Sjöstrand and M.Bengtsson, Comput.Phys.Commun. 46(1987)43; 39(1986)347

M.Bengtsson and T.Sjöstrand, Phys.Lett.**185B**(1987)435

[5] VENUS collab. H.Yoshida et al., Phys.Lett.**B198**(1987)570

K.Abe et al., Phys.Lett.**B234**(1990)107

Chapter 4
Electron Identification

In this Chapter, we present the method for electron identification in VENUS. Electron identification in multihadronic events with good efficiency and small contamination is generally hard, since the number of hadron backgrounds is several hundred times more than that of electrons. Using two independent detectors, LA & TRD, we have achieved hadron rejection of ~1/1000 and have obtained electron candidate tracks of high purity.

4.1. Methods of Electron Identification

As we described in Chapter 2, VENUS has a special ability of electron identification using TRD in addition to an ordinary calorimeter technique. With these two independent methods, we obtained a high purity sample of electron and were able to check their performance independently.

Here, we search for electrons among all charged tracks in multihadronic event which are selected in previous chapter. It is possible to exist many electrons in a one multihadoronic event. At first, we require an acceptance of TRD and LG ($|\cos\theta| \leq 0.68$) for a track direction. Second, momentum p of electron candidates should be greater than 1.0 GeV/c since TRD and LG is not efficient at low momentum. After these selections of a charged track, we use TRD and LG to identify electrons in multihadronic event.

4.1.1. *E/p* Method with LG Calorimeter

E/p

E/p is ratio of energy deposit in the electro-magnetic calorimeter E[GeV] and momentum p[GeV/c] of an associated charged particle . For the electron or positron which deposit its whole energy in the calorimeter, *E/p* ratio should be unity while other non-showering particles such as $\pi\pm$ show $E/p \ll 1$.

In VENUS experiment, momentum of a charged particle is calculated from the curvature of its trajectory in CDC. Its resolution is expressed as a function of transverse momentum with respect to magnetic field ($p_\perp$)) in eq.(3-4). Total energy of electron is measured by the calorimeters. VENUS has two of them; Lead-Glass electro-magnetic shower calorimeter and Liquid-Argon sampling calorimeter. Since TRD covers barrel region only, which is also covered by LG, we use only LG hereafter. The energy resolution of LG is given in eq.(3-7).

By extrapolating a track in CDC to LG surface, we decide incident point of the charged particle in LG[1]. For an electron, an electro-magnetic shower in the calorimeter spreads typically over 2×2 modules. To minimize the overlap effect of

energy deposit among particles, only 2×2 modules around the incident point are used in calculating sum of the deposit energies in LG. Fig.4-1 shows a typical energy deposit pattern of an electron from a controlled sample and a hadron in LG. Hereafter, we always use the controlled sample of 'single electron event' when we want to show performance od a genuine isolated electron. 'Single electron' event is a QED process ($e^+e^-\rightarrow e^+e^-\gamma$) where only one electron or positron is tagged in VENUS system. Extracting 'single electron' is described in Appendix-1.

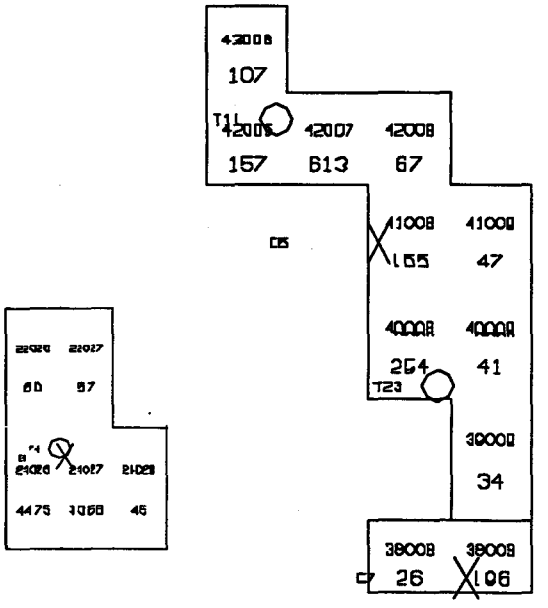

(a) (b)

Fig.4-1 Example of Electron and Hadron Energy Deposit in LG

(a) example of an electron cluster. (b) example of a hadron cluster. The cross symbol shows the center of cluster. The circle symbol shows the incident point of charged track. The electron cluster is taken from a 'single electron' event (See Appendix-1). The hadron cluster is taken from multihadronic event which is described in Chapter-3.

Since there is slight nonlinearity in the energy E as a function of momentum, E/p values deviate from unity at low momentum as shown in Fig.4-2. Moreover, the resolution $\sigma<E/p>$ is slightly wider for momentum below 1GeV/c (Fig.4-2(b)).

It should be corrected so that $<E/p> = 1.0$ for all momentum region. We introduce μ value as follows.

$$\mu \equiv \frac{(E/p - <E/p>)}{\sigma<E/p>} \qquad (4\text{-}1).$$

For an electron that has momentum of several GeV/c , 2×2 modules contain most of its shower. We require the selection criterion for electrons as $\mu > -2.5$ without upper value cut. The μ distribution of electron has a long tail because the electron may emits photon (bremsstrahlung) as shown in Fig.4-3. In the case of Fig.4-3(b), E/p tends to be greater than 1.0, because 2×2 modules contain the energy deposit of the photon and the electron completely, while the track momentum in CDC corresponds to that of the electron after bremsstrahlung. Therefore, the upper value cut introduce the inefficiency for electron detection. The hadron background in high E/p region is negligible as will be classified later and is shown in Fig.4-25.

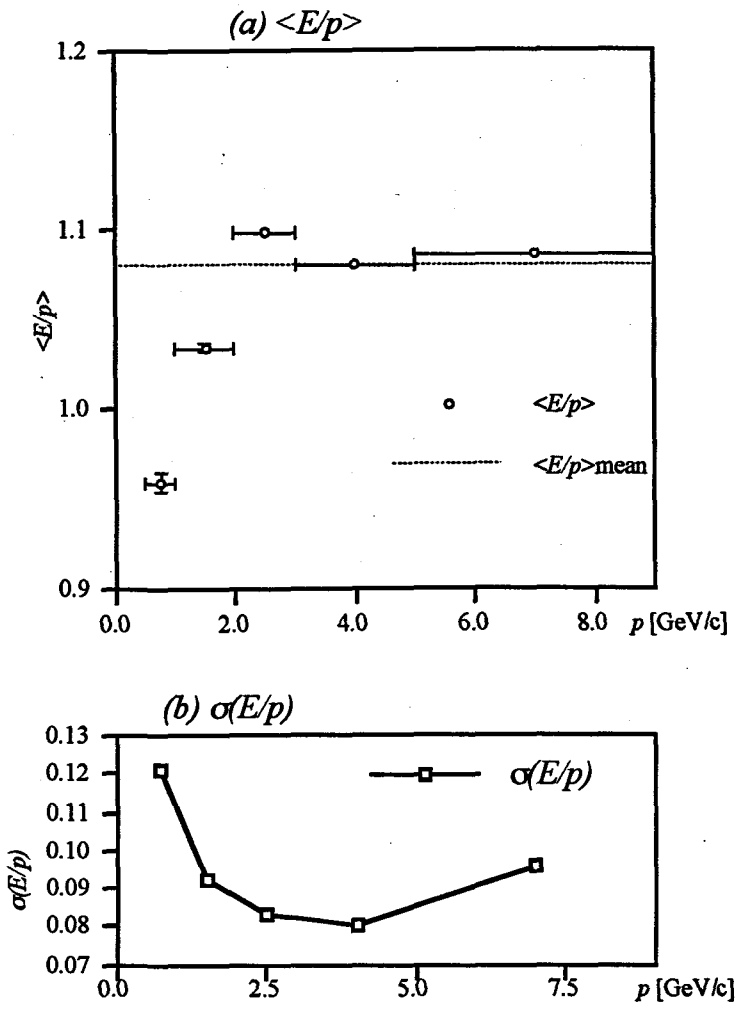

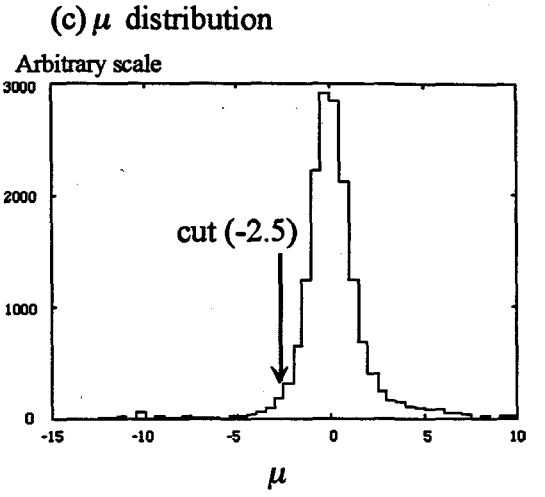

The momentum dependence of E/p and the deviation of E/p from 1.0.

(a) mean of E/p, (b) standard deviation of E/p and (c) μ distribution

These data are measured using 'single electron' events. The dotted line in Fig.4-2(a) is the mean over the whole momentum range. The error bar is statistical error only. (c) is a μ distribution of electrons. A cut point $\mu \geq -2.5$ is shown in Figure.

Fig.4-2 Momentum Dependence of E/p

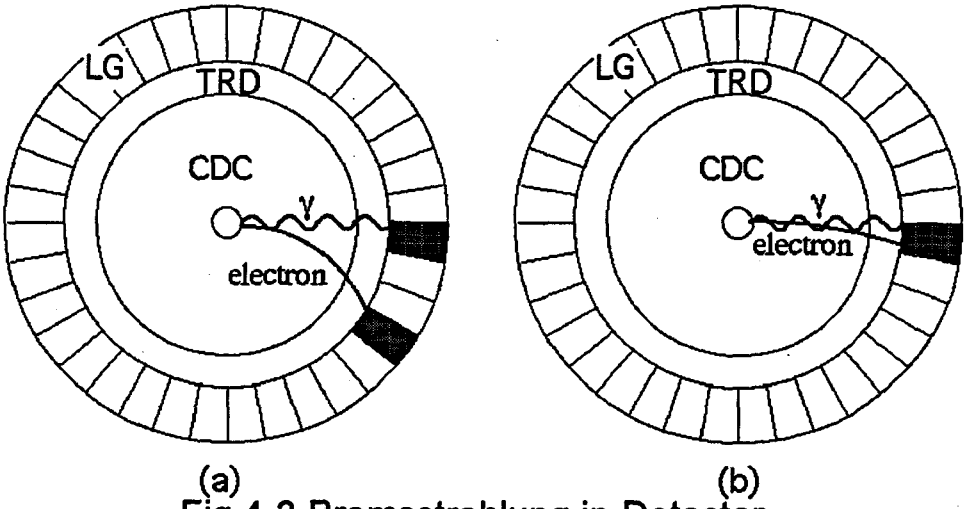

Fig.4-3 Bremsstrahlung in Detector

Schematic illustrations of bremsstrahlung in the detector. (a) a hard photon bremsstrahlung, (b) soft photon bremsstrahlung. In case (a), clusters of electron and photon is separated and E/p of charged track are calculated correctly as 1.0. However, in case (b), photon and charged track go into the same cluster. In this case, E/p is larger than 1.0, because the momentum of the charged particle is measured after bremsstrahlung.

Track-Cluster Matching

In addition to the cut in μ , we require track-cluster matching to reject hadrons further. There are two reasons why the hadron track occasionally has a large μ value and becomes a background for electron identification.

1) Photons in a jet causes a shower which overlaps with the other hadron track,
2) Hadronic shower starts in LG calorimeter.

In either case, the center of gravity of the energy deposit in the 2×2 modules is expected to deviate significantly from the incident point of the hadron track. On the other hand, the electron should show smaller deviation. Fig.4-1b shows typical energy deposits of a hadron in LG. The incident point of the hadron and the cluster center would not associate well. The requirement of track-cluster matching thus can suppress hadrons.

We define goodness of matching as the difference between the cluster center and the incident point Δ_Z (for z direction) and $r\Delta\phi$ (for ϕ angle direction) must be less than 6.5 cm (See Fig.4-4). Fig.4-5 shows distributions of the difference between the center of 2×2 module's energy deposits and the incident point of the electron track extrapolated from CDC with 'single electron' event data in two angles. The criteria of the matching parameter Δ_z, $r\Delta_\phi$ to be less than 6.5 cm improves hadron background by ~10%.

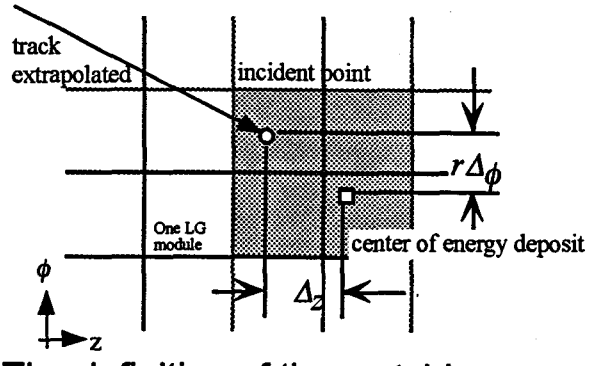

Fig.4-4 The definition of the matching parameters

Definition of track-cluster matching parameters. Δ_z and $r\Delta_\phi$ are distance between the center of the cluster and the incident point of the charged track along the z or ϕ axis.

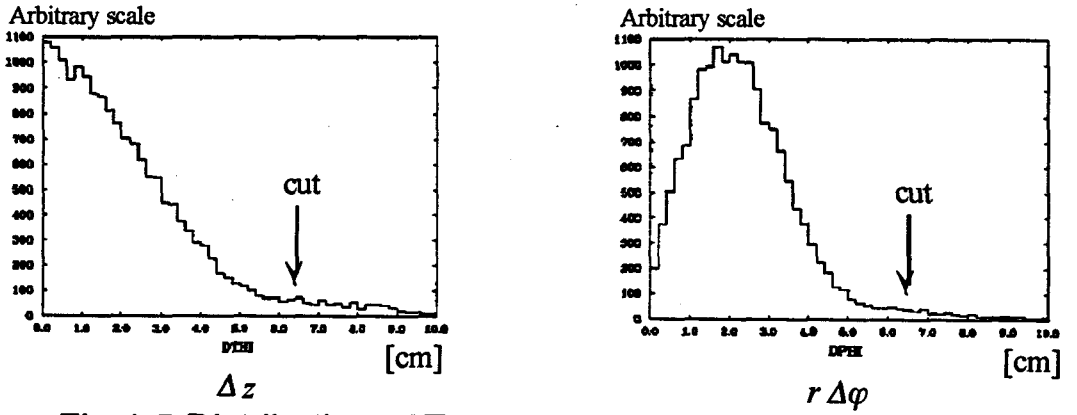

Fig.4-5 Distribution of Track-Cluster Matching Parameter

The track-cluster matching parameter Δ_z and $r\Delta_\phi$ The cutting point of them for electron identification is 6.5 cm. These are Δ_z and $r\Delta_\phi$ distributions of 'single electron' events.

4.1.2. Use of Transition Radiation

How to Identify Electrons with TRD

In TRISTAN energy region, only the electron reaches $\gamma \geq O(10^3)$ in the multihadronic event (where $\gamma = \frac{1}{\sqrt{1-(v/c)^2}}$ is a relativistic factor of the particle). Any other charged particle cannot reach speed enough to emit detectable transition radiation. A transition radiation is a several 10keV X-ray for VENUS-TRD's radiator[2]. Fig.4-6 shows a truncated mean spectrum of electrons and π energy deposit in TRD where truncation means exclusion of the largest pulse height in the four layers. The X-ray chamber is sensitive not only to transition radiation but also to ionization of charged particles. The energy deposit E of π samples which is only due to ionization is below 10 keV. An energy is deposited by electron through both ionization and transition radiation. The spectrum extends to higher energy than that of π's as shown in Fig.4-6. Thus, electron can be distinguished from π by the energy deposition in TRD. Since ionization and total energy of transition radiation depend on the particle momentum, we must decide selection criteria for e/π separation depending on its momentum. Fig.4-7 shows the mean energy deposit of electron and hadron in TRD.

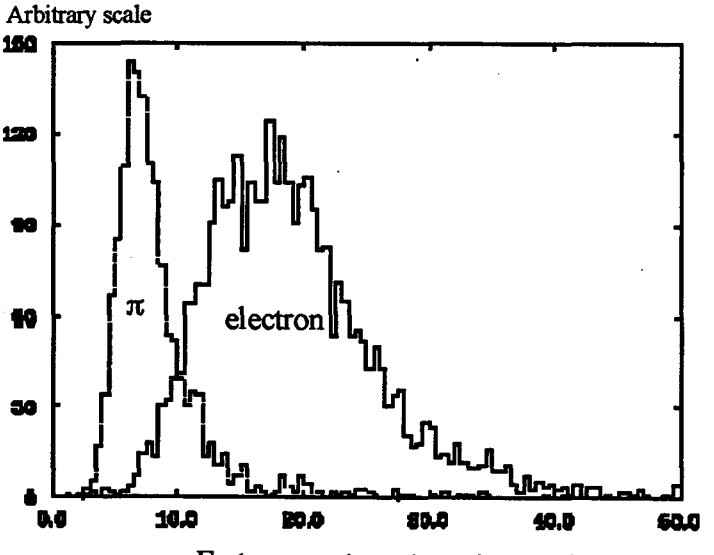

Fig.4-6 TRD Energy Spectrum

Energy spectrum of the electron and π of TRD. The electron sample was selected from the 'single electron' sample and π sample selected from the two-photon event (See Appendix-1).

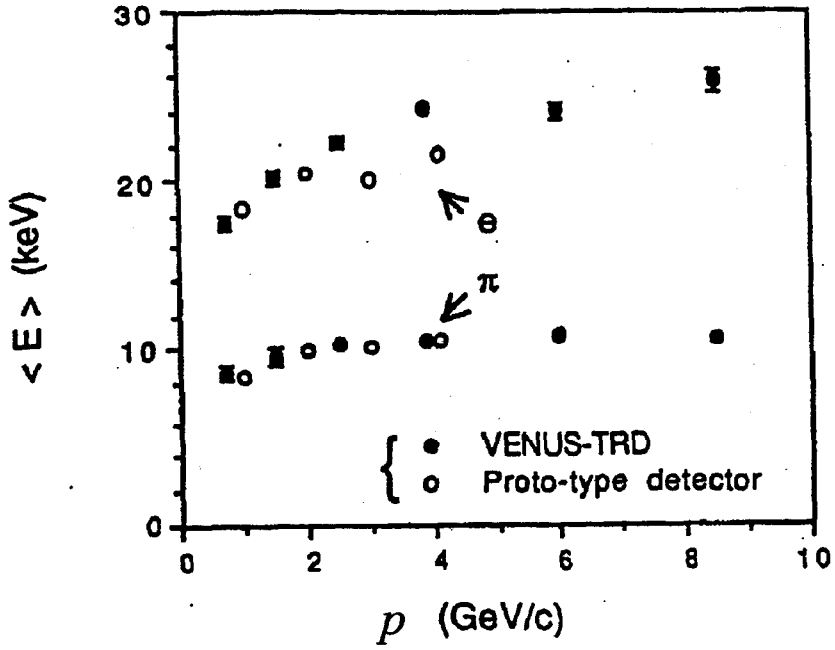

Fig.4-7 Mean Energy Deposit of Electron And Hadron in TRD

The mean energy deposit of electron and hadron in TRD. The solid circle symbol shows VENUS-TRD data from e^+e^- colliding experiment. The circle symbol shows the data of proto-type detector with beam test.

Selection Criteria with TRD

By cutting low energy part of the TRD spectrum ($E_{TRD} \geq E_{cut}$), we can obtain an electron sample with reduced hadron (π) contamination. The hadron contamination as well as the electron efficiency (ε_e^{TRD}) are functions of the cut energy E_{cut}. It is roughly 5% at ε_e^{TRD}=80% and 8% at ε_e^{TRD}=90% for low-multiplicity event. It increases about 2~3% in the multihadronic event. We chose an E_{cut} where the electron efficiency ε_e^{TRD} becomes 80 % in low-multiplicity event. The cut point depends on the particle momentum as follows.

$$E_{cut}(\varepsilon_e^{TRD}=80\%)[\text{keV}] = \begin{cases} 8.9 + 1.1p\ [\text{GeV/c}] & \text{for } p < 1.9\ \text{GeV/c} \\ 11 & \text{for } p \geq 1.9\ \text{GeV/c} \end{cases} \quad \ldots(4\text{-}2)$$

The detail of derivation of energy deposit E_{TRD} is given in next section.

4.1.3. Data Analysis Flow of TRD information

In this section, we describe data flow of TRD in off-line analysis[3]. The flow consists of two parts. One is association of energy deposit in TRD with the trajectory of the charged particle in CDC. The other is correction of gain variation as a function of time and position in the chamber. The off-line data analysis flow is illustrated in Fig.4-8.

Track-Hit Clustering & Sharing

By extrapolating a CDC track to TRD, we search an associated hit in TRD. It will be presented as 'track-hit clustering' from now on. Since a CDC track has a finite spatial resolution and a charged track may be deflected by multiple-scattering in the materials before TRD, a track-hit clustering must consider these effects. Fig.4-9 gives the definition of association width ε by which TRD hits are associated with the track.

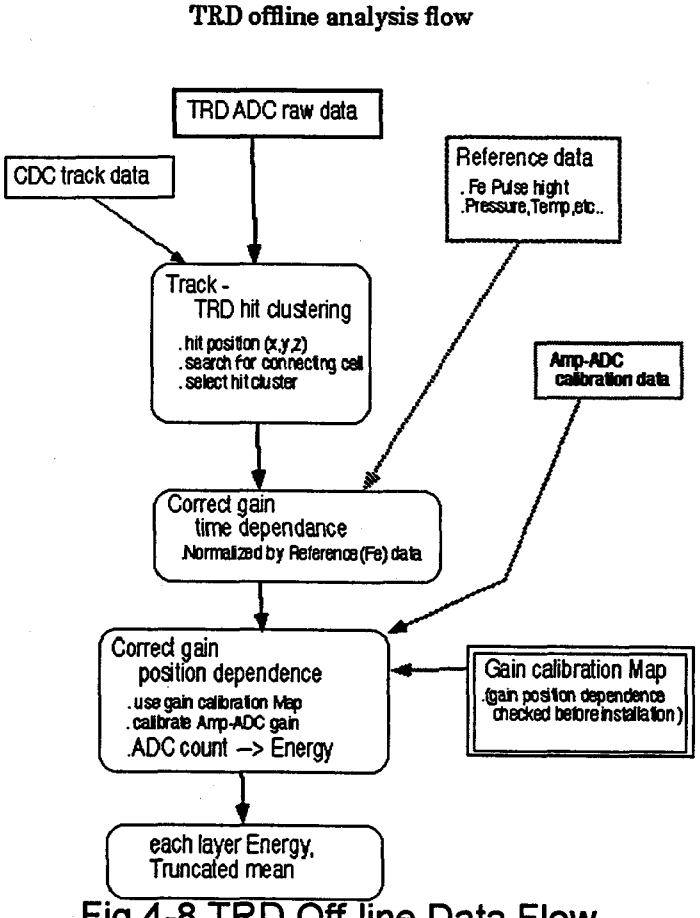

Fig.4-8 TRD Off-line Data Flow

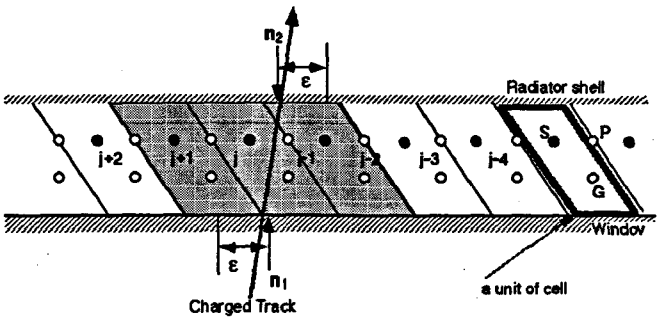

Fig.4-9 Track-hits clustering

Track-hit clustering. The associated chamber cell of charged track is contained in the shaded zone.

Fig.4-10 shows clustering efficiency as a function of ε. We choose ε=0.5 [in unit of chamber cell]. Typically an incident track is associated with two hits in one layer of TRD, because the drift paths of ions are skewed by the magnetic field. The track-hit clustering efficiency is found to be more than 98% in each layer of TRD. With requirement of geometrical acceptance estimated by a CDC track, the probability of having hits in all the layers in TRD is 96.3 ±0.2%, including the effect of sector gaps of TRD, a dead wire etc.

In a multihadronic event, about 10% of all tracks overlap with each other in a single cell of TRD. Therefore, energy deposits in TRD should be shared correctly with associated multiple tracks. Otherwise, the energy overlapping track could be misidentified as electron. In this procedure, the position dependence of the chamber gain and the path length of the tracks in TRD cell should be taken into account. For 3-dimensionally reconstructed tracks, we can decide incident point and path length in the cell. We divide ADC count of the wire to each associated track in proportion to the gain at the incident point or the path length.

$$ADC_i = ADC_{total} \times \frac{G_i \cdot L_i}{\sum_i (G_i \cdot L_i)} \qquad \ldots(4\text{-}3)$$

where ADC_i is the contribution of the i-th track in total ADC count (ADC_{total}), Gi is the relative gain at the incident point of the i-th track. It is normalized by a gain at the position where ^{55}Fe is placed in the same X-ray chamber. L_i is the path length in the chamber cell of the i-th track. This 'sharing' method improves contamination of hadrons by ~20% in typical jets.

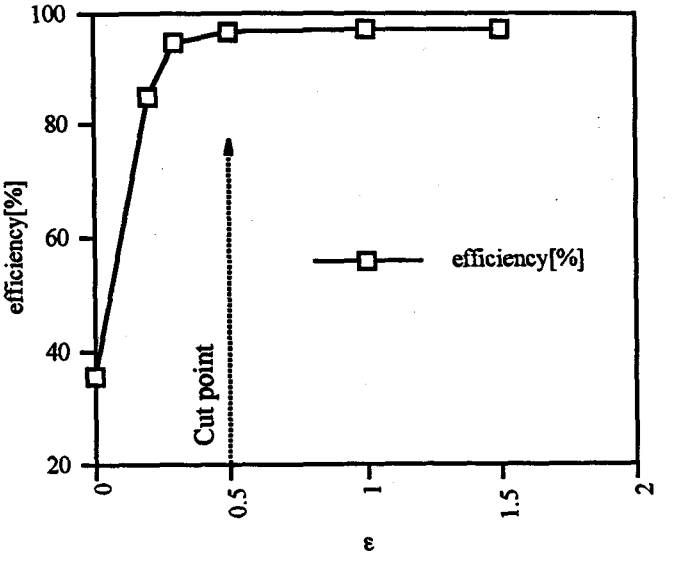

Fig.4-10 ε vs Association Efficiency

Figure shows the association efficiency between the charged track and TRD hit as the function of ε in units of cell width. It is defined in Fig.4-9. The criteria of association is determined to be $\varepsilon \geq 0.5$. The probability of having hits in all four layers in TRD is 96.3 ±0.2%.

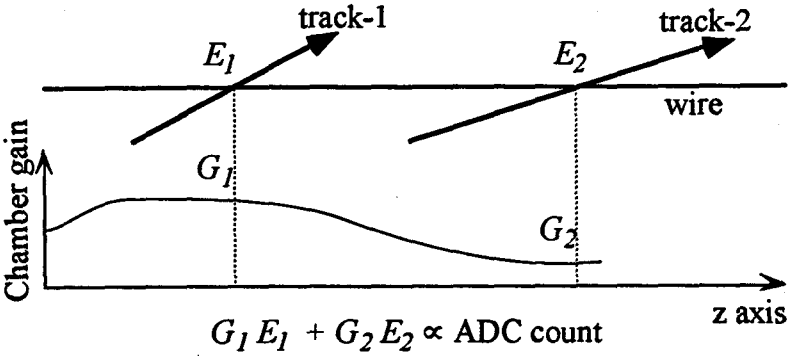

Fig.4-11 Track-hits Sharing in TRD

Figure shows the idea of track-hits sharing. The track-1(2) deposits energy $E_1(E_2)$. The chamber gain at each incident points is G_1 and G_2. These relative gain is a function of z position in this figure. In this case, the ADC counts which sum up all energy deposits in this wire is proportional to $G_1 E_1 + G_2 E_2$.

Energy Correction of Position Dependence

The gain in the X-ray chamber has some position dependence due to distortion of the cathode plane (typically ~100μm) and wire sag. The relative gain G_i can be represented as a function of z and ϕ. Fig.4-12 shows the position dependence of the gain in ϕ direction as expressed as a function of wire number at the same z position. Typical gain variation due to distortion is 10~20 %. Moreover wire sag effect by gravity also causes gain variation along z coordinate and the tilt angle of the cell (ϕ). Fig.4-13 shows the effect of tilt angle of the cell. On the other hand, gain of the electronics such as preamplifiers and ADCs have slight variation within 5 %.

Therefore the energy should be calibrated according to the gain map which is made before the installation.

The gain position dependence was measured for all 32 TRD's X-ray chambers before installation. We scanned each wire of TRD by 10 cm step for outer 2 layers and by 20 cm for inner 2 layers with ^{109}Cd X-ray source (22 keV). Total of 57344 points are measured. In order to monitor overall gain variation, ^{55}Fe X-ray (5.9 keV) spectrum was continuously measured at each reference point of the chambers. Fig.4-12 shows the result and a global fitting of the gain variation. The error of gain map is within 2~3% which is shown in Fig.4-12c as the difference between the measurement and the global fit. The relative gain position dependence of each chamber is calibrated with the result of using ^{109}Cd. Moreover, independent calibration for position dependence with e, π and cosmic-ray is constantly done with data during operation. It adds more fine tuning of the calibration.

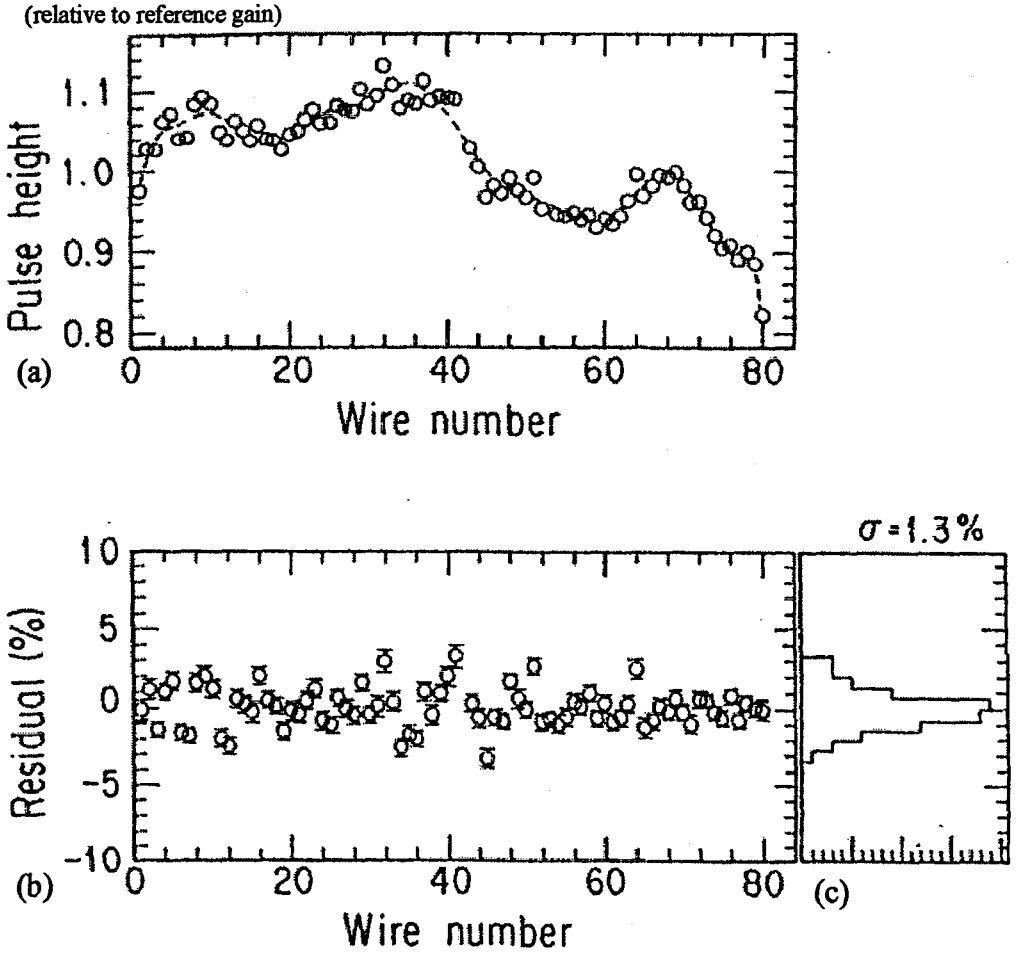

Fig.4-12 Position Dependence of Chamber Gain

Figure shows a typical example of position dependence of chamber gain which is measured using ^{109}Cd (X-ray, 22keV). (a) is a position dependence as a function of wire number at same z position. Pulse height is a relative gain which is normalized by a gain at reference point. (b) is a residual from a global fitting which is shown in (a) with dashed line. (c) is a projection histogram of (b). A standard deviation σ of (c) is 1.3%.

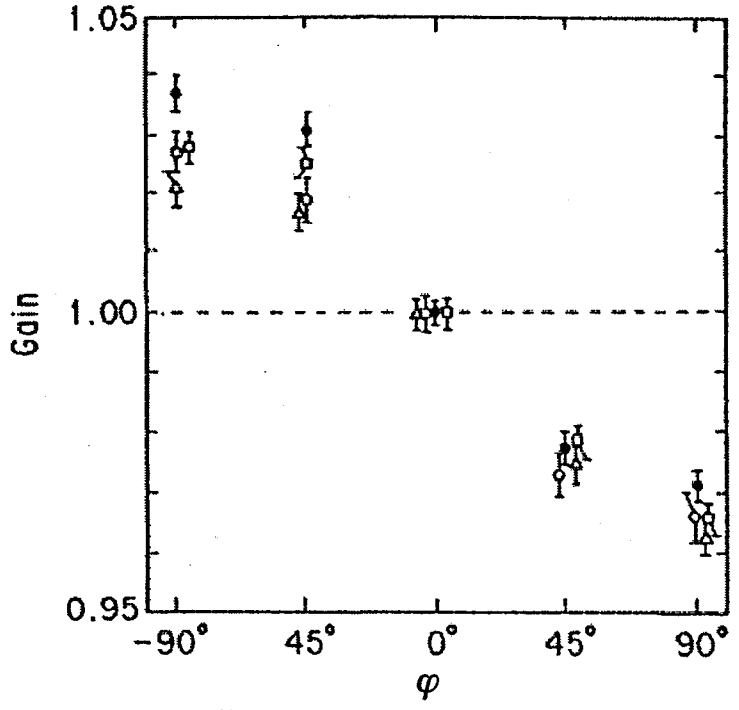

Tilt angle of a chamber cell [degree]

Fig.4-13 Wire Sag Effect for Chamber Gain

The gain variation by wire sag effect is shown in the figure. It depends on a thilt angle of a chamber cell (ϕ).

Energy Correction of Time Dependence

Further correction of the energy should be made for time dependence of the chamber gain. It always drifts due to change of atmospheric pressure, temperature, gas composition and electronics conditions (HV, ADC) etc.. All 32 X-ray chambers of TRD have reference points which are always irradiated by 5.9 keV X-ray from ^{55}Fe. Their spectrum are measured between experiments and data are recorded (See the detail in Chapter-2). This information is used for the correction of the time dependence. Since the ratio of the gain at a point and that at reference point $G_i/G_{reference}$ is almost constant, the spectrum of the reference can be used to correct other points. The corrected energy at a time $E(t)$, is made using ^{55}Fe spectrum as follows.

$$E_{TRD} = E(t) \times \frac{R(t=0)}{R(t)} \qquad \ldots(4\text{-}4)$$

where $R_{(t)}$ is a peak value of the spectrum at ^{55}Fe reference points. E_{TRD} is the energy which is normalized at t =0.

Combining the correction methods described above, the energy is calculated as the function of incident point of the charged track and event time as follows.

$$E_{TRD}\,[\mathrm{keV}] = \frac{ADC_i}{G_i(wire\ number,\ z)} \times \frac{R(t=0)}{R(t)} \times f_{energy} \qquad \ldots(4\text{-}5)$$

where f_{energy} is the conversion ratio from ADC count to energy. $G_i(wire\ number,\ z)$ is representation of G_i in equation(4-3).

To identify an electron, we compare energy E_{TRD} to cutting energy E_{cut} in equation(4-2).

4.2. Backgrounds in Electron Candidates

μ distribution of electron candidates which are selected with criteria in previous section is shown in Fig.4-14. As mentioned before, misidentified hadrons would be the most serious background for electron tagging. In addition, γ-conversion electron and Dalitz decay electron would also be backgrounds for electrons from semileptonic decay of heavy quarks.

4.2.1. Hadron Background

Selection of Hadron Sample by TRD

As shown in Fig.4-6, a pure sample of π's can be selected by cutting E_{TRD} above 8keV. With this sample, we can estimate the background beneath the electron peak shown in Fig.4-14. The solid circles indicate electron candidates before μ>-2.5 requirement. The histogram represents a μ distribution for π's thus selected in the multihadronic event. It shows the hadron background. The histogram is normalized to the number of entries in the range μ < -5.0. Table4-1 shows the hadron background thus estimated in the electron candidates after cut with μ>-2.5 . The contamination of hadron backgrounds of electron candidates is 10.0 ±0.9% for μ> -2.5.

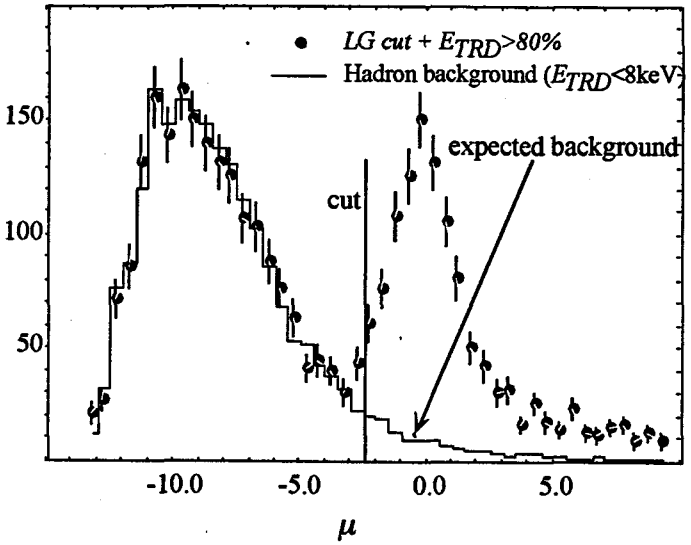

Fig.4-14 μ Distribution of Electron Candidates

The hadron background that is selected by E_{TRD}≤8keV is shown as solid line. The plotted points are electron candidates before μ cut.

Table 4-1 Hadron Background of Electron Candidate

		p[GeV/c] 1.0~2.0	2.0~3.0	3.0~5.0	5.0~
pt[GeV/c]	0.0~0.5	9.7% ± 1.4%	11.2% ± 2.6%	12.0% ± 2.9%	12.9% ± 3.2%
	0.5~1.0	10.9% ± 2.9%			
	1.0~	8.8% ± 4.1%	11.0% ± 6.0%	4.4% ± 3.1%	7.5% ± 3.7%

Hadron backgrounds of electron candidates. The quantity of the hadrons in the final sample of electron candidates is calculated with the method described in the text. The background of all p-p_t region is 10.0±0.9%.

4.3. Estimation of Efficiency

In this section, we describe additional factors affecting acceptance and efficiency of the detector for the electron identification in the multihadronic event.[Note]

Detection efficiency of electrons with the criteria described in the section 4.1.3 are estimated here.

Inefficiency of the detection arises from several factors such as chamber inefficiency, gaps or dead channels of TRD, module gaps of LG, energy loss due to bremsstrahlung etc. Furthermore, the efficiency in hadron jets is significantly degraded comparing with that in an ideal environment, where electrons are well isolated from other particles. As for track reconstruction, electron tracks may be lost or poorly reconstructed due to the existence of nearby tracks as illustrated in Fig.4-19. In the calorimeters, the energy deposit of nearby particles may affect the cluster center position calculated in section 4.1.1. Nearby tracks are also harmful for the electron track in TRD, since they may have an excessive energy with the algorithm described in the section 4.1.2. and consequently, the electron track may be given substantially less energy as shown in Fig.4-21.

To evaluate these effects quantitatively, the study was made in the following two steps

1) Estimation of the efficiency in an controlled environment using "single-electron" sample.
2) Estimation of the degradation of the efficiency in the multihadronic events. This was accomplished by embedding a well-established electron data taken from 'single electron' sample into the multihadronic event data. ("Embedding" method)

Note: Here, we describe only efficiency of detectors (CDC, LG and TRD) for electron identification. On the other hand, acceptance of trigger for multihadronic event is needed for estimation of numbers of events. Measurement of angular distribution of quark should be also corrected with the acceptance. It is given in Table 5-2 in the next Chapter.

4.3.1. Detection Efficiency of 'Single Electron' Tracks

To show performance of TRD, we give efficiencies of electron identification and hadron contamination of tracks in low-multiplicity events. Here, overlap effect between tracks and energy deposits are negligible. In this respect, tracks in low-multiplicity events make a good sample for testing the detector performance. To study E_{TRD} spectrum of pure electrons, we use 'single electron' events ($e^+e^- \rightarrow e^+e^-\gamma$). As the low-multiplicity hadron sample, we use two-photon reaction $e^+e^- \rightarrow e^+e^-\pi^+\pi^-$ (These are described in Appendix-1). Fig.4-15 shows correlation of electron efficiency and hadron contamination for the above two cases. TRD energy cut for electron identification is chosen using this relation and the spectrum of E_{TRD} as shown in Fig.4-6. Electron detection efficiencies under various conditions are summarized in the first row of Table 4-2 (a),(b) and (c). When TRD and LG are used together, the efficiency is~60% for $p < 1$GeV/c and ~70% for $p \geq 1$GeV/c.

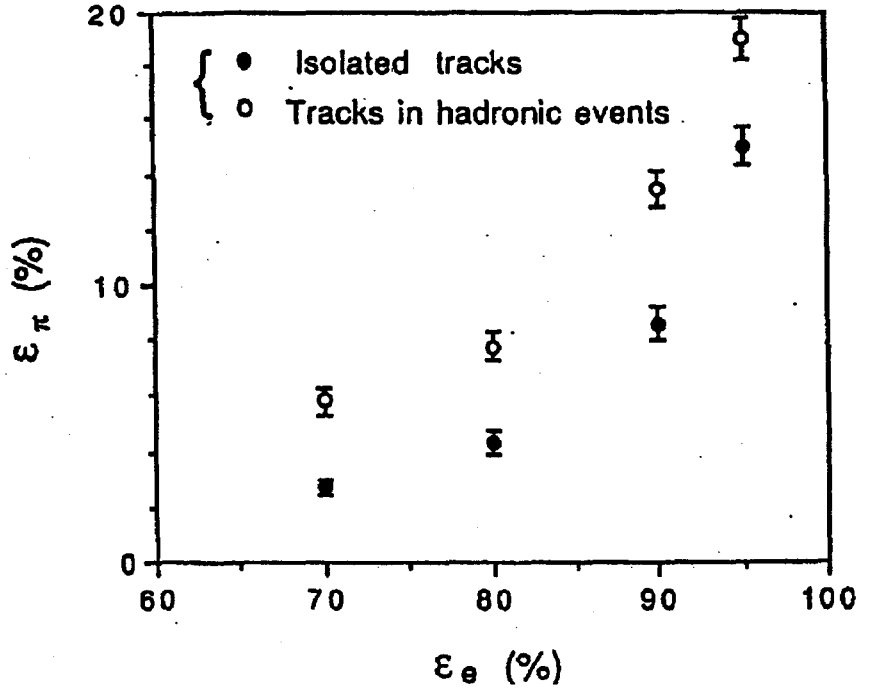

Fig.4-15 Electron Efficiency vs. Hadron Efficiency

Table 4-2 Electron Identification Efficiency of LG&TRD

(a) TRD & LG

		p[GeV/c] 0.0~1.0	1.0~2.0	2.0~3.0	3.0~5.0	5.0~
Single e		59.9% ± 1.1%	67.1% ± 0.9%	71.0% ± 0.9%	71.7% ± 0.7%	69.8% ± 1.1%
inclusive e	0.0~0.5	50.9% ± 1.6%	56.7% ± 1.6%	60.9% ± 1.3%	65.3% ± 1.1%	60.3% ± 1.8%
pt[GeV/c]	0.5~1.0	57.4% ± 1.6%	59.9% ± 1.4%			
	1.0~	–	62.1% ± 1.8%	64.1% ± 1.3%	65.4% ± 1.0%	62.8% ± 1.6%

(b) LG

		p[GeV/c] 0.0~1.0	1.0~2.0	2.0~3.0	3.0~5.0	5.0~
Single e		81.8% ± 0.9%	90.8% ± 0.5%	90.8% ± 0.6%	93.0% ± 0.4%	91.4% ± 0.7%
inclusive e	0.0~0.5	74.6% ± 1.6%	82.2% ± 1.3%	84.0% ± 1.0%	88.6% ± 0.7%	86.9% ± 1.3%
pt[GeV/c]	0.5~1.0	82.7% ± 1.3%	87.2% ± 1.0%			
	1.0~	–	89.3% ± 1.2%	88.2% ± 1.0%	88.9% ± 0.7%	86.5% ± 1.2%

(c) TRD

		p[GeV/c] 0.0~1.0	1.0~2.0	2.0~3.0	3.0~5.0	5.0~
Single e		72.0% ± 1.1%	76.9% ± 0.8%	80.5% ± 0.8%	79.1% ± 0.6%	77.6% ± 1.0%
inclusive e	0.0~0.5	71.8% ± 1.6%	76.3% ± 1.5%	78.6% ± 1.2%	79.8% ± 0.9%	76.4% ± 1.6%
pt[GeV/c]	0.5~1.0	72.8% ± 1.5%	77.3% ± 1.2%			
	1.0~	–	77.9% ± 1.6%	80.6% ± 1.6%	79.6% ± 0.9%	77.7% ± 1.5%

The electron identification efficiency in the barrel region of VENUS. The cut criteria of TRD energy deposit is given in equation (4-2) in main text.

(a) ε_e^{LG+TRD} efficiency of LG and TRD selection for electron

(b) ε_e^{LG} efficiency of LG selection for electron (c) ε_e^{TRD} efficiency of TRD selection for electron

4.3.2. Detection Efficiency of An Electron in Multihadronic Events

Since there are many factors which affect the efficiency of electron identification, the detector simulator does not always predict its value exactly. Therefore, we have tried to estimate it with real experimental data as much as we can.

In charged track reconstruction, more than 2 tracks may be lost in the track finding algorithm due to chamber inefficiency and due to hit sharing. The momentum and spatial spread of the reconstructed track could result in the deviation of *E/p* from unity and mismatch between the tracks and the cluster (See Fig.4-16)

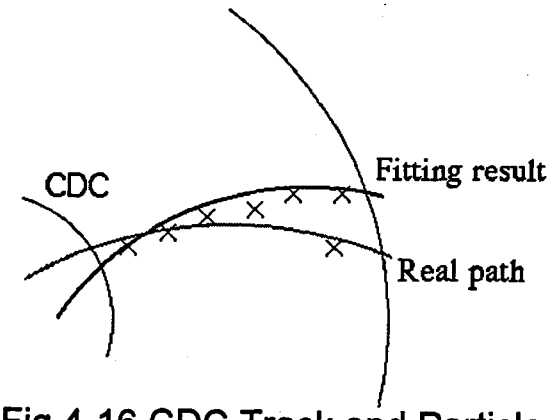

Fig.4-16 CDC Track and Particle Path

In the calorimeter, the energy deposit of a charged particle overlaps with that of nearby particle. If the energy deposit of a hadron overlaps with that of γ, or other energy deposits, it looks like a large energy deposit faking an electron (Fig.4-17).

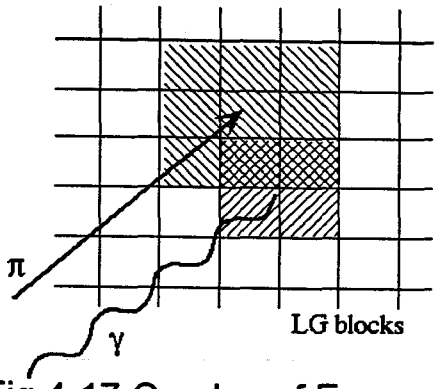

Fig.4-17 Overlap of Energy Deposit

Figure shows an image of overlap of energy deposit. The cross hatched region is overlap of hadron energy deposit and photon energy deposit.

To evaluate the efficiency of the electron identification in the multihadronic events, well-established electron samples are embeded in them. The sample was taken from 'single electron' events as was done in the previous section. Then they are reanalyzed and the efficiency of identification in multihadronic event can be determined.

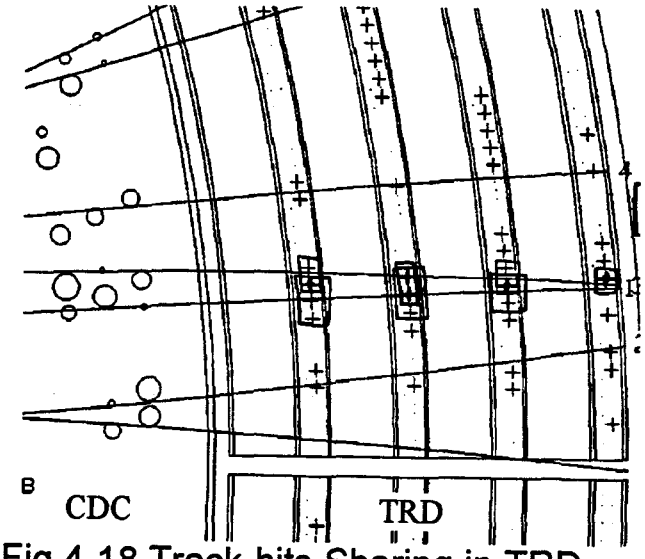

Fig.4-18 Track-hits Sharing in TRD

'Single Electron' Event Embedding in Multihadronic Events

First, we choose a 'single electron' event and a multihadronic event in a short experimental period, because the variation of chamber gain between them is likely to be small. CDC hits of two events are mixed on drift time base. When an electron track overlaps with one of multihadronic event in the same CDC cell, only the faster drift time is picked up in the new mixed data. The tracks are reconstructed again after mixing CDC hits. Similarly, the data of LG are mixed by simply summing up those of two events. For TRD, the chamber gains of the multihadronic event are corrected to equaly those of 'single electron'. After this correction, we sum up the two raw data of 'single electron' and multihadronic event. They are reanalyzed after reconstruction of tracks in mixed CDC data. Fig.4-19 shows flow of making superimpose event. An example of event mixing is shown in Fig.4-20.

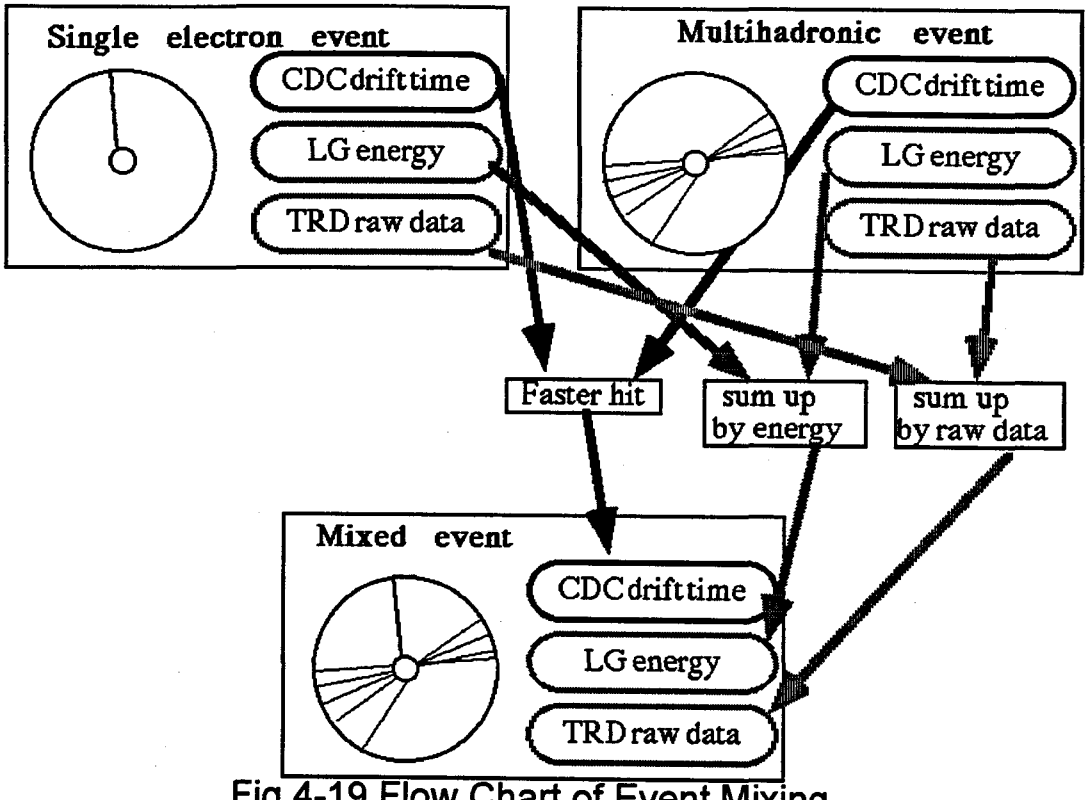

Fig.4-19 Flow Chart of Event Mixing

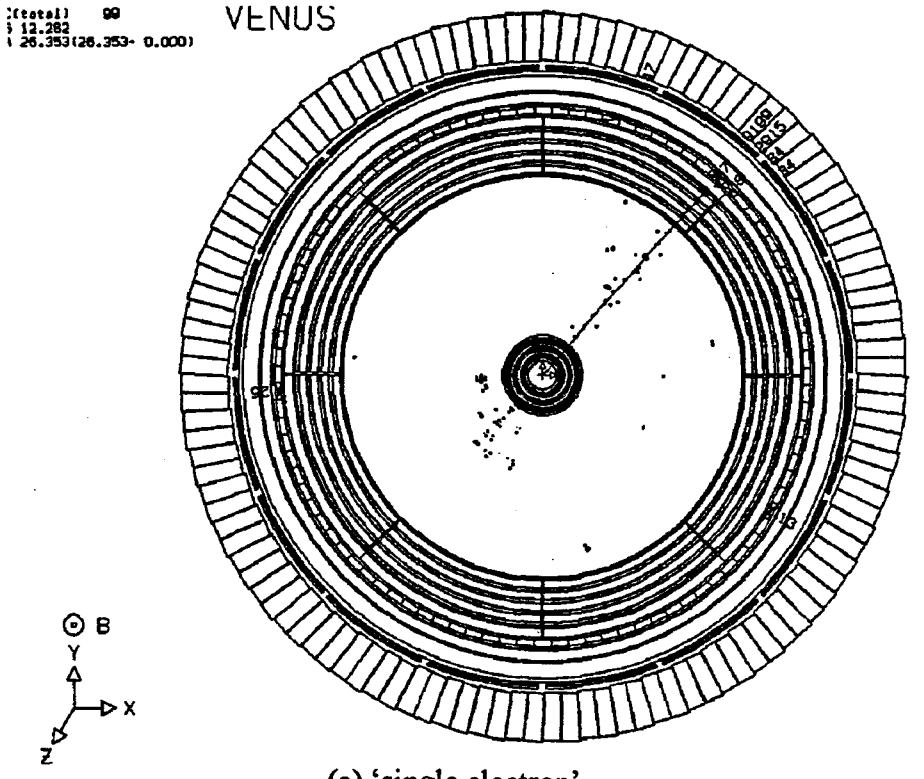

(a) 'single electron'

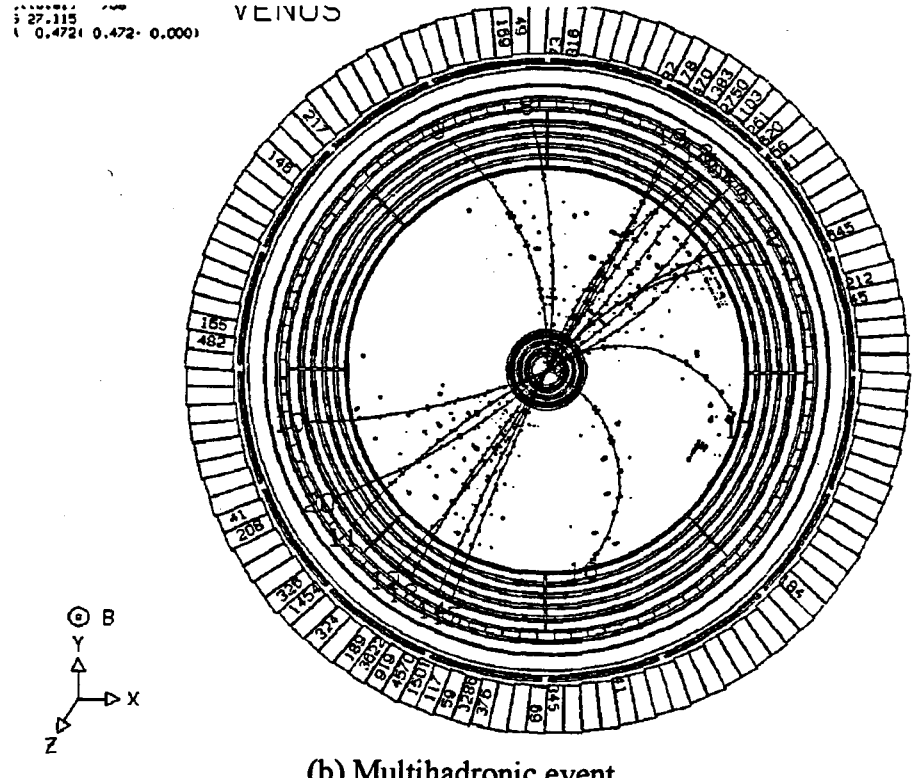

(b) Multihadronic event

Fig.4-20a,b Example of Superimpose Electron Event

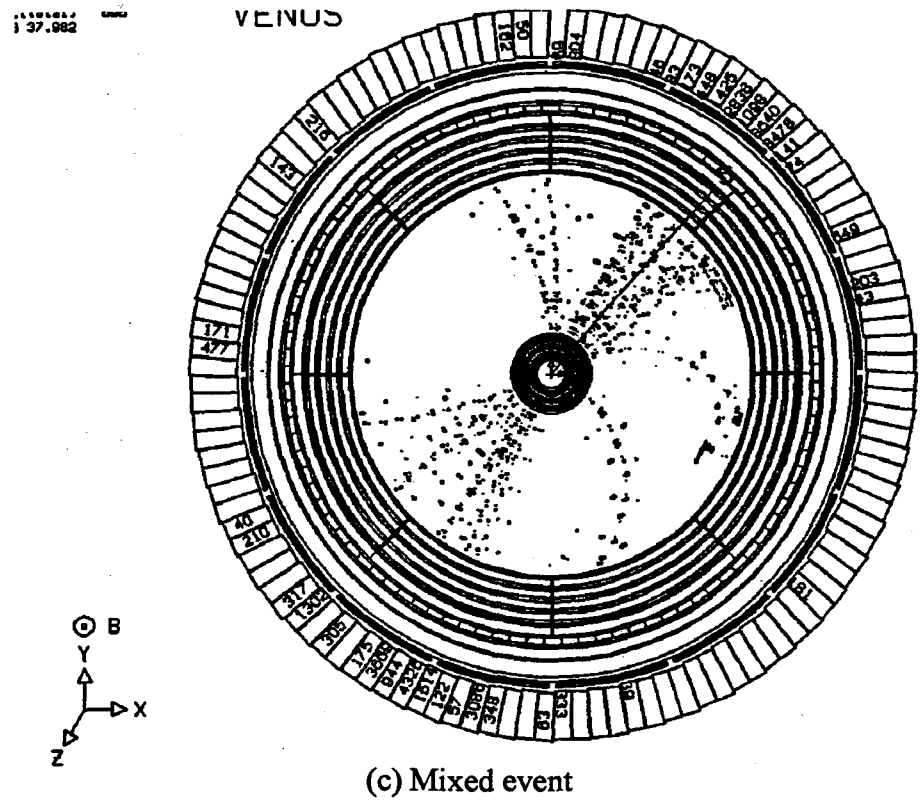

(c) Mixed event

A track in figure (a) is embbeded into those in figure (b). It shows as a track in figure (c)

Fig.4-20c Example of Superimpose Electron Event

Effect of Nearby Particles in Hadronic Jets

We found degradation of efficiency in track reconstruction or energy measurement with the above mentioned technique. These effects are shown in Fig.4-21 as the ratio of the reconstructed quantities, 'after' to 'before' embedding. The resultant effect on E/p distribution is shown in Fig.4-22a and its ratio is displayed in Fig.4-22b.

Fig.4-23 shows the efficiency loss due to effects of hadron jet as a function of p_t. It is evident that electrons close to the jet axis, which have low p_t, are affected seriously by nearby particles in the jet. The over-all detection efficiency are shown in Fig.4-24 and tabulated in Table 4-2 as a function of p and p_t.

We list in the 2nd, 3rd and 4th raw of Table4-2 shows efficiencies for electron identification in the multihadronic event studied this way. They do not include detector acceptance effect. These are the efficiencies for electrons within $|\cos\theta| \leq 0.68$ (= TRD & LG coverage).

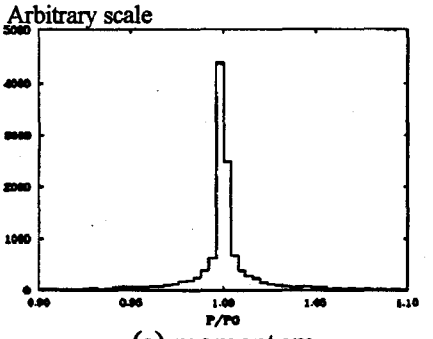

(a) momentum

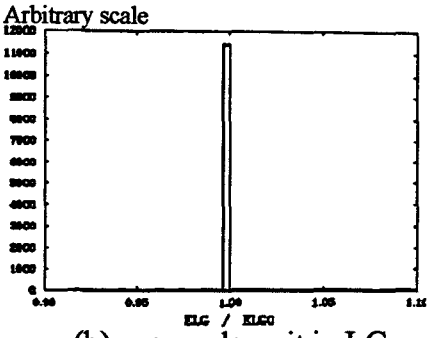

(b) energy deposit in LG

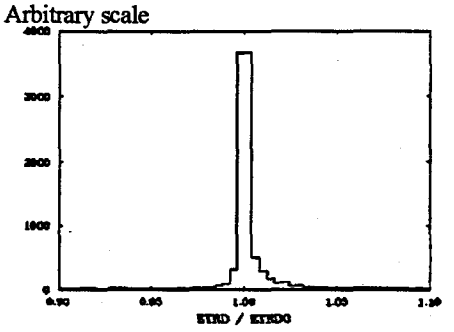

(c) TRD energy

The figure shows the variation after electron embedding.
Ratio = $X_{\text{after mixing}}$ / $X_{\text{before mixing}}$ for each value is shown. (a) momentum of CDC track, (b) energy deposit in LG, (c) energy deposit in TRD.

Fig.4-21 Variation after Mixing

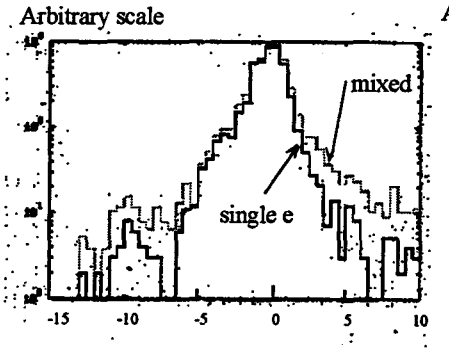

(a) $\sigma(E/p)$ distribution

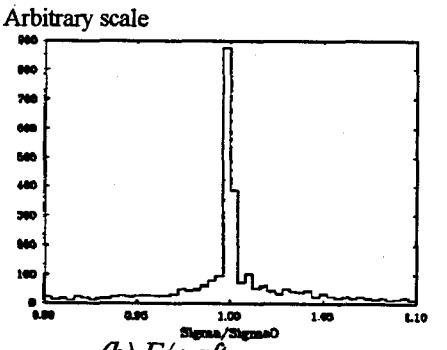

(b) $\frac{E/p\ after}{E/p\ before}$

Fig.4-22 *E/p* Distribution of 'Single Electron' and Mixed Event

(a)*E/p* distribution of 'single electron' and mixed event. The solid line shows *E/p* distribution of 'single electron' tracks. The dotted line gives a distribution of embedded track in mixed events. The overlap of energy deposit makes high energy tail. The effect for the inefficiency is 5~10% for p_t <1.0 GeV/c region after requirement of track-cluster matching.

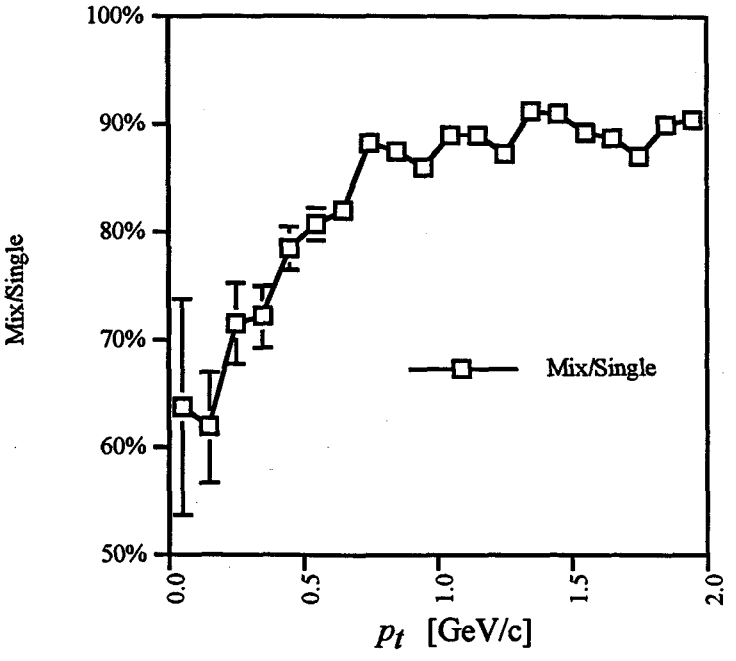

Fig.4-23 Effect of hadron jet

Figure shows the ratio of electron identification efficiency of 'single electron' and mixed event(=multihadronic event). In low p_t region, the efficiency decreases significantly.

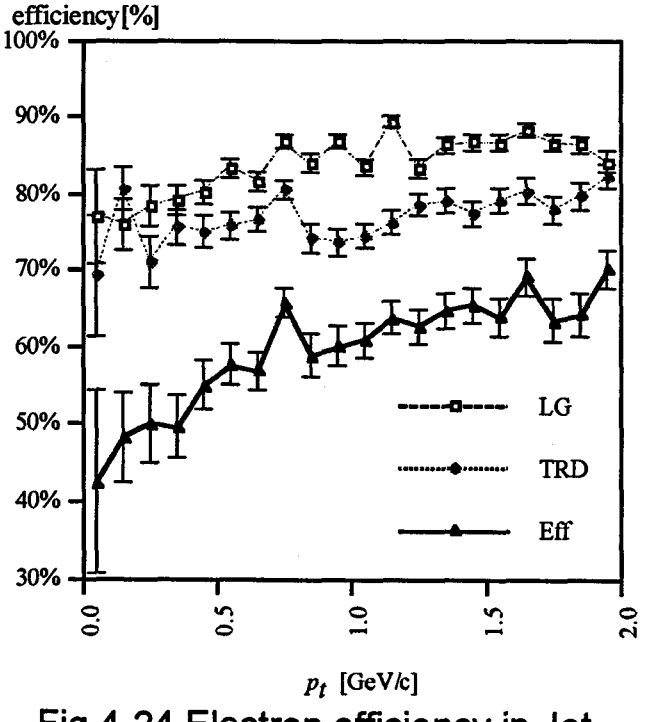

Fig.4-24 Electron efficiency in Jet

Figure gives electron identification efficiency in hadron jet which is estimated by superimpose method.

TRD Efficiency for a Hadron in Multihadronic Events

To estimate the purity of electron candidates, we need efficiency of TRD, or LG, for hadrons in multihadronic events (See the section 4.4). Table 4-3 presents TRD efficiency for the hadron estimated with the charged track with μ<-5σ. The hadron efficiency of TRD (ε_h^{TRD}) is estimated as

$$\varepsilon_h^{TRD} = \frac{\text{Numbers of tracks selected by LG\&TRD in } \mu<-5\sigma}{\text{Numbers of tracks selected only by LG in } \mu<-5\sigma} \quad \ldots(4\text{-}6).$$

Table 4-3 Hadron Efficiency of TRD Criteria

	p[GeV/c] 1.0~2.0	3.0~4.0	4.0~5.0	5.0~
pt[GeV/c] 0.0~0.5	9.2% ± 0.4%	8.2% ± 0.4%	7.2% ± 0.4%	8.7% ± 0.6%
0.5~1.0	8.2% ± 0.5%			
1.0~	5.9% ± 0.9%	7.7% ± 1.1%	6.4% ± 0.9%	10.4% ± 1.0%

Table presents hadron efficiencies (ε_h^{TRD}) after TRD selection of ε_e^{TRD}=80% in multihadronic events . Hadrons are suppressed more than ten times after using TRD information.

4.4. Summary of Electron Candidates In Multihadronic Event

Here, we summarize criteria for selection of electron candidates in multihadronic event.

1. The track should be reconstructed well and should be with TRD & LG acceptance.

good track in multihadronic event as selected by condition (3-10)

acceptance	$\|\cos\theta\| \leq 0.68$
and	$\|p\| \geq 1.0$ GeV/c

2. The energy deposit LG calorimeter should be associated well with CDC track in terms of its momentum and position in

$$\mu \geq -2.5$$

$$r\Delta_{\phi,}\Delta_{\theta} \leq 6.5 \text{ cm}$$

3. At least three out of four TRD layers should have a hit and the truncated mean energy of the track should be greater than the threshold

$$N_{hit}^{TRD} \geq 3 \text{ layers}$$

$$E_{TRD} \geq E_{cut}(\text{at } \varepsilon_e^{TRD}=80\%)$$

$$(E_{cut}(\text{at } \varepsilon_e^{TRD}=80\%) = 8.9 + 1.1p \text{ or } 11 \text{ keV})$$

After applying all the above criteria, total of 1333 electron candidates tracks are found in 1131 multihadronic events.

μ distribution of the finally selected electron candidates in the multihadronic events is shown in Fig.4-25. Fig.4-26 is p and p_t distribution of the electron candidates. Solid circles in Fig.4-25 in the region of $\mu \geq -2.5$ corresponds to 1333 electron candidates. Dotted line corresponds to the selection with only LG information. Figure shows a performance of TRD.

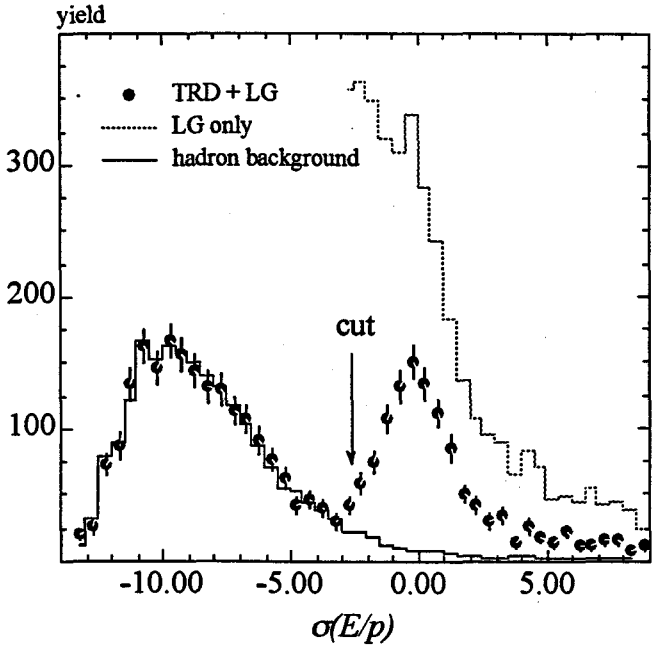

Fig.4-25 μ Distribution

μ distribution of the tracks in multihadronic event. The selections of the track are given in the text. The dotted line corresponds to the selection with only LG information (track-cluster matching). Solid circles indicate electrons selected by TRD in addition to LG. The final electron candidates are selected as $\mu \geq -2.5$. The solid circles and solid line are the same as Fig.4-14

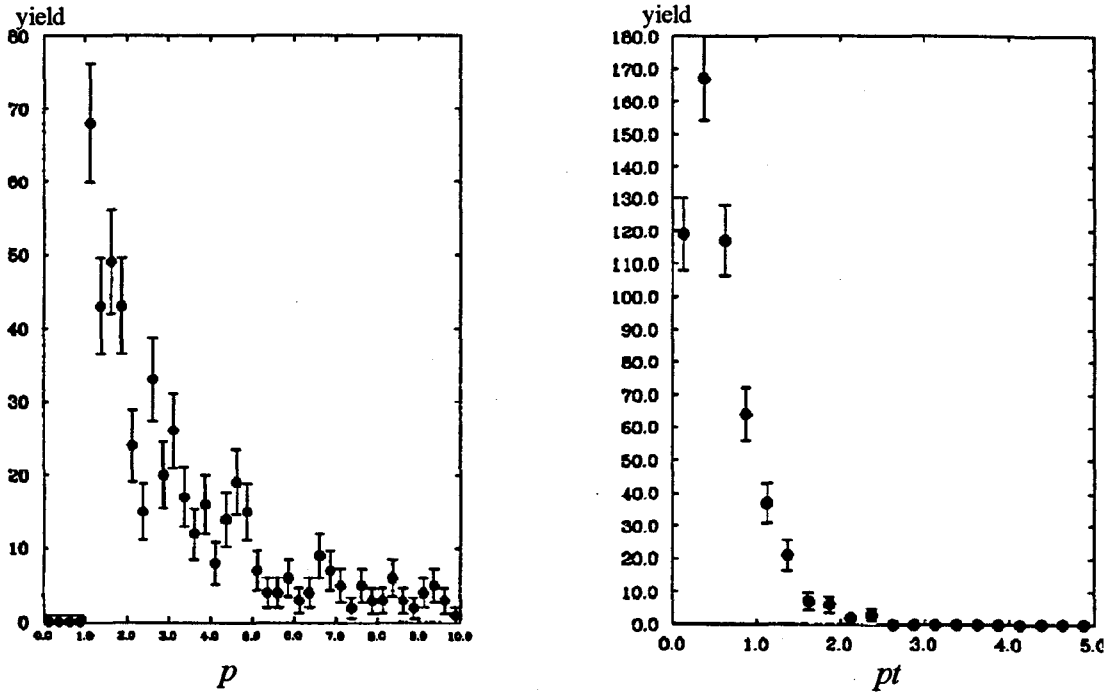

Fig.4-26 p and p_t Spectrum of Electron Candidates

The momentum p and transverse momentum p_t distribution of the final sample of the electron candidates in multihadronic event. The fraction of various electron source and background is discussed in Chapter-5.

References of this Chapter

[1] A.Krüger et al., OULNS-92-07, in preparation for Nuclear Instruments and Methods A

[2] N.Terunuma et al., Nuclear Instruments and Methods A323(1992)471

[3] N.Kanda VENUS TRD group, VENUS Note

Chapter 5

Study of Heavy Quarks

In this Chapter, we discuss heavy quark productions in the e^+e^- annihilation using the inclusive electrons selected in the previous section. In the first section, the composition of the selected electron is estimated. The fraction of prompt electron in the sample which we believe come from semileptonic decay of b and c quarks are determined simultaneously with other source of electrons. In the second section, tagging (= separation) of the quark flavor using p_t spectrum of the prompt electron is reviewed. Then a technique to estimate the number of b and c quarks is developed. Finally, cross section, fragmentation function and asymmetry of b, c quark production are determined.

5.1. Composition of Electron Candidates

5.1.1. Other Backgrounds for Prompt Electron

In addition to purity of electron candidates, composition of electrons from various sources in those should be estimated for a study of heavy quark. Dominant backgrounds of prompt electrons are follows.

γ Conversion

As described in the section 1.2.2, about the $[1-\exp(-\frac{7}{9}\times 7\%)] \simeq 5\%$ of photons will convert to electron-positron pairs in the material before TRD. Most of them have their transverse momentum(p_t) below 1GeV/c. We must reject them while keeping the prompt electrons as much as possible. We use a topological signature of conversion electrons for rejection. The details of the rejection routine is given in the Appendix A-3. The rejection efficiency of the conversion electron $\varepsilon_{\gamma\to ee}^{\gamma\text{-rejectoin}}$ is ~83% (See Table A3-1 in Appendix A-3), with almost 90% of the prompt electrons kept.

π^0 Dalitz Decay

The other background comes from electrons in π^0 Dalitz decay ($\pi^0\to e^+e^-\gamma$), where the branching ratio is less than 1.2%[1] . Since phase space of the electron is similar to that of conversion electrons, the Dalitz decay electrons are suppressed to be about ~40% ($\varepsilon^{\gamma}_{\text{Dalitz}}$), using the same routine for conversion rejection.

Total of 543 events survived after γ-conversion rejection.

5.1.2 Fraction of Prompt Electrons in the Final Sample

Our electron identification process can be divided into three steps, LG selection, TRD selection and γ-conversion rejection. Using the efficiencies of these steps for hadrons, conversion electrons and prompt electrons (Table 4-2,4-3), we can estimate the number of prompt electrons in the final electron candidates. Fig.5-1 shows an outline of electron identification. The relation between efficiencies of each step and numbers of candidates that survive each step is given in the figure.

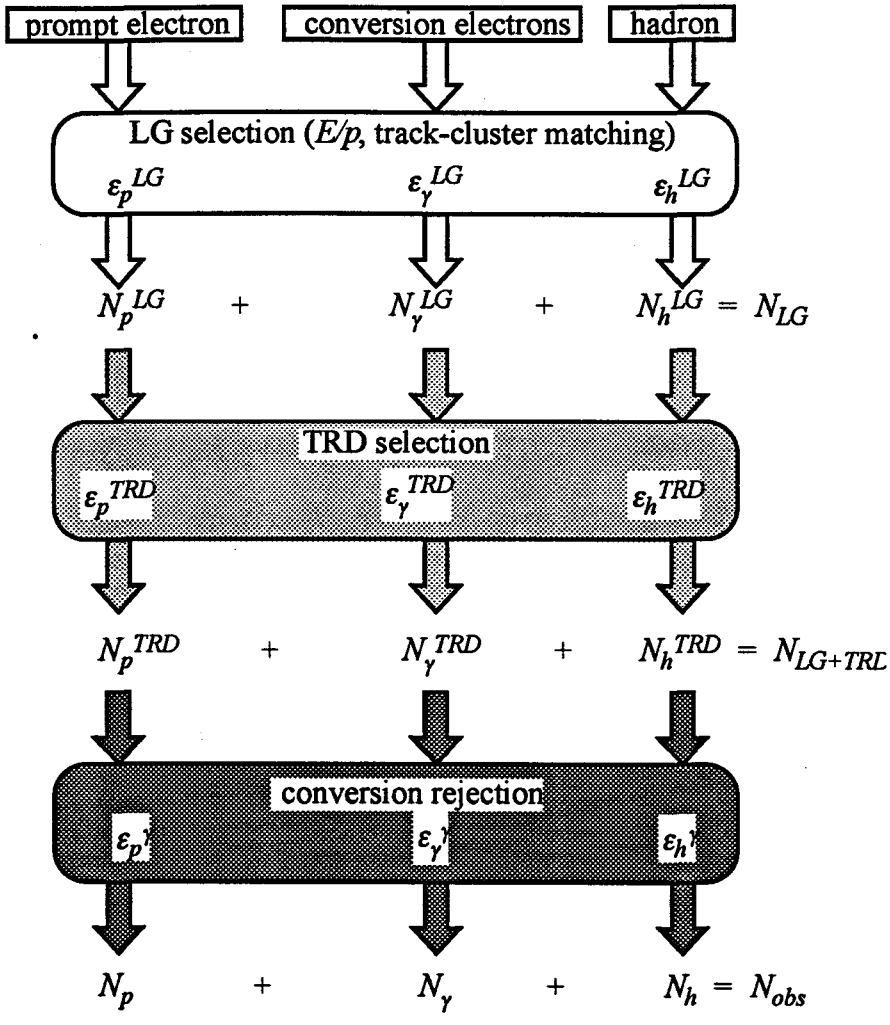

Fig.5-1 Flow chart of electron identification

The figure shows a flow chart of the electron identification. Selection procedure is divided into 3-steps: (1)using LG (*E/p*), (2)using TRD and (3)conversion rejection.

As displayed in the figure, the relation of the number of events at each step are as follows.

$$N_{obs} = N_p + N_\gamma + N_h \qquad \text{...(5-1a)}$$

$$N_{LG+TRD} = N_{obs} + n = N_p^{TRD} + N_\gamma^{TRD} + N_h^{TRD}$$

$$= \frac{N_p}{\varepsilon_p^\gamma} + \frac{N_\gamma}{\varepsilon_\gamma^\gamma} + \frac{N_h}{\varepsilon_h^\gamma} \qquad \text{...(5-1b)}$$

$$N_{LG} = N_{LG+TRD} + m = N_{obs} + n + m$$

$$= N_p^{LG} + N_\gamma^{LG} + N_h^{LG}$$

$$= (N_p^{TRD} + N_\gamma^{TRD}) / \varepsilon_e^{TRD} + (N_h^{TRD}) / \varepsilon_h^{TRD}$$

$$= \left(\frac{N_p}{\varepsilon_p^\gamma} + \frac{N_\gamma}{\varepsilon_\gamma^\gamma}\right) / \varepsilon_e^{TRD} + \left(\frac{N_h}{\varepsilon_h^\gamma}\right) / \varepsilon_h^{TRD} \qquad \text{...(5-1c)}$$

where N_p is the number of prompt electrons, N_γ, that of photon conversion electrons and N_h, that of hadrons in the final sample. $\varepsilon_{p,\gamma,h}^{TRD}$ and $\varepsilon_{p,\gamma,h}^{\gamma}$ represent corresponding efficiencies of TRD selection and conversion rejectionalgorithm respectively. By solving these three equations for N_p, N_γ and N_h, we can estimate the number of prompt electrons in the final sample (N_p). The error of each value is given by statistical error of N_{obs}, N_{LG+TRD} and N_{LG}. In this calculation, only N_{obs}, n and m in equation (5-1a,b,c) are treated as independent variables. Their statistical errors are given as the square root of them. The systematic error of the N_p is calculated using errors in the efficiencies as

$$(\delta N_p(\text{sys.}))^2 = \Sigma \left\{ \frac{\partial N_p}{\partial \varepsilon} \delta\varepsilon^2 \right\} \qquad \text{...(5-2)}$$

where ε represents the efficiencies, $\varepsilon_{p,\gamma,h}^{\gamma}$ and $\varepsilon_{p,\gamma,h}^{TRD}$. Errors for N_γ and N_h are evaluated similarly replacing N_p with N_g or N_h in equation (4-7). Calculation of N_p is carried out separately in two by four bins of p_t and p. Results of the estimation are shown in Table 5-1.

Table 5-1 Number of Each Source in Electron Candidates

p_t [GeV/c]	p [GeV/c]	$N_{observed}$	Prompt electron	conversion	hadron
~0.8	1.0~3.0	254	93.6±18.1±8.4	99.5±5.1±2.5	60.9±2.4±3.6
	3.0~5.0	107	68.1±11.2±3.8	17.6±2.3±1.1	21.4±1.2±2.2
	5.0~10.0	35	19.4±6.6±2.0	2.0±0.8±0.8	3.9±0.5±1.0
	10.0~	18	11.8±4.6±1.2	4.8±1.3±0.5	4.7±0.8±0.2
sum		414	192.9±22.8±15.4	128.9±6.0±4.8	92.2±2.8±7.0
0.8~	1.0~3.0	41	32.4±6.7±0.9	4.2±1.0±0.1	4.5±0.6±0.8
	3.0~5.0	41	35.1±6.7±0.9	2.0±0.8±0.1	3.9±0.5±0.7
	5.0~10.0	30	23.0±5.9±1.1	2.3±0.9±0.3	4.7±0.8±0.6
	10.0~	17	13.1±4.4±1.2	3.0±0.9±0.4	0.9±0.4±0.1
sum		129	103.6±12.0±4.0	11.4±1.8±0.9	14.0±1.2±2.2

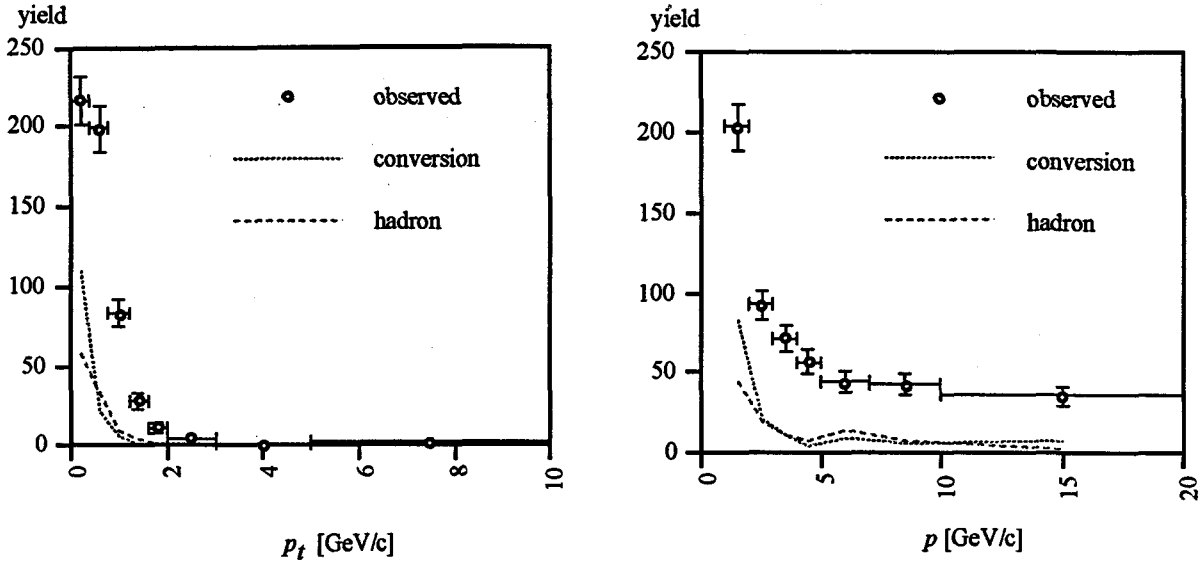

Fig.5-2 Spectrum of Electron Candidates and Estimated Background

Figure shows momentum and transverse momentum spectrum of electron candidates. Circle symbol shows observed number of electron candidates. Each line shows background (conversion electron and hadron). These backgrounds are estimated by the method that is explained in chapter-4.

Fig.5-2 shows p_t and p spectrum of the electron candidates. The fraction of the prompt and γ-conversion electrons and hadrons are calculated according to Table5-1. The number of prompt electrons after background subtraction and correction of LG&TRD efficiency is given as follows.

$$N^{corr} = \frac{N_p}{Eff_{eID}} = \frac{N_p}{\varepsilon_p{}^{LG}\ \varepsilon_p{}^{TRD}\ \varepsilon_p{}^{\gamma}} \tag{5-3}$$

where N_p is the number of prompt electrons which is given in Table 5-1 and Eff_{eID} is the detector (TRD+LG) efficiency of electron identification which is given in Table 4-2. The statistical error of N^{corr} (= δN^{corr})is calculated using the error of N_p in Table 5-1 with error propagation of them in equation (5-3).

5.2. Cross Section & Fragmentation of Heavy Quarks

5.2.1 Electron Spectrum of Semileptonic Decay

Each quark flavor has a characteristic spectrum of its decay electron. In this section, we describe p ,p_t spectrum of prompt electrons.

p_t Spectrum & Quark Flavor

p_t spectrum of the electron from semileptonic decay of heavy quarks is characterized by the mass of parent quark. Since the b quark is more massive (~5.3 GeV/c^2) than c quark (~1.7 GeV/c^2), p_t spectrum of b tends to be harder than that of c quark as shown in Fig.1-7. Fig.5-2 shows p_t spectrum of electron candidates (circles) that were obtained in previous section. The spectra show γ-conversions and hadron backgrounds, too. Comparing Fig.1-7, Fig.5-2 shows enhancement of c flavor for low p_t region and of b flavor for high p_t region. For prompt electrons, b flavor fraction is ~70% for the region of $p_t \geq 0.8$GeV/c and ~30% for that of $p_t < 0.8$GeV/c.

p Spectrum & Fragmentation

Contrary to p_t spectrum, the momentum spectrum of the semi-leptonic decay electron is strongly affected by the energy fraction of the mother hadron that contains primary b or c quark. The energy fraction of the b-hadron ($X_b = \frac{E_b}{E_{beam}}$) or c-hadron ($X_c$) as a function of X_q is called as the fragmentation function. Fig.5-3 shows $X_{b,c,bc}$ distribution that is predicted by Monte-Carlo(JETSET 7.3). The prediction of them in the Monte-Carlo is characteristic to Peterson function (equation(1-22)). X_q distribution of parent quark strongly affects momentum spectrum of semi-leptonic decay electron. In low p region (<5GeV/c), c quark fraction is dominant but b fraction becomes increasingly important at high momentum electron.

Using both p_t and p characteristic, we can obtain enhanced samples and estimate numbers of b or c quark in the electron candidates.

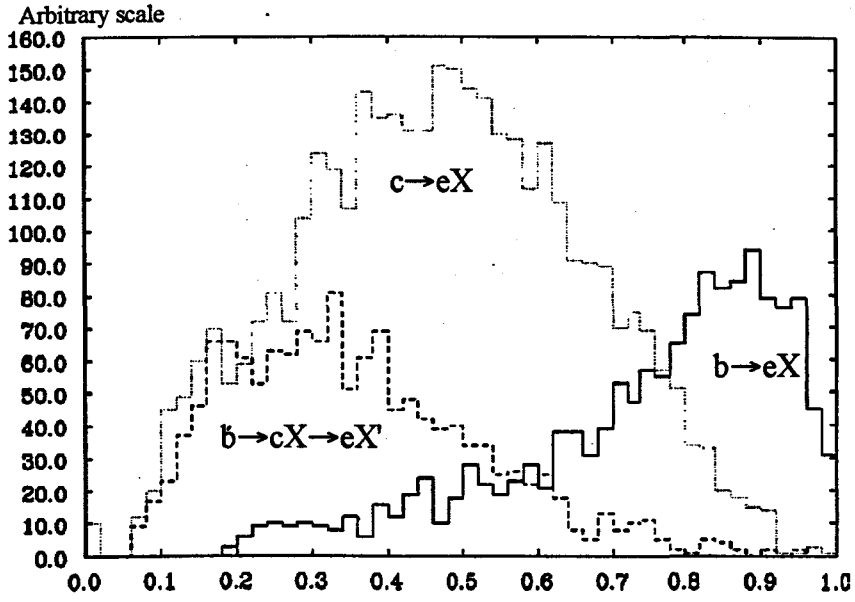

Fig.5-3 X_q Distribution of b-hadron and c-hadron

Figure shows the X_q distribution of b-hadron and c-hadron and c-hadron from b cascade decay in Monte-Carlo simulation.

5.2.2. p-p_t Spectrum Unfold Fitting

The observed number of prompt electrons is sum of the numbers of the b and c semileptonic decay electrons. Using Monte-Carlo prediction of their p-p_t spectrum from b or c quark, we fit the observed p-p_t spectrum of the electron and extract number of produced b and c quarks, Nb and Nc.The contribution of other flavor (u,d,s) is negligible.

Definition of the Fitting Function & Parameters

The observed spectrum is corrected by the detector efficiency of LG and TRD for electron tagging according to eq(5-1).Then the corrected spectrum is compared with one expected from Monte-Carlo. we use JETSET 7.3 + Fujimoto-Shimizu Radiative correction[2]. A contribution of b→e$^-$X in prompt electron spectrum can be written as

$$N_b\ (1+\delta)_b\ 2\ BR_b(1-BR_b)\ P_b(p,p_t,\varepsilon_b)\ A_b \qquad (5\text{-}4a)$$

N_b,is the number of b events produced initially. $(1+\delta)_b$ is radiative correction for the production of b quark. ε_b,is the Peterson fragmentation function parameters. $P_b(p,p_t,\varepsilon_b)$ is probability of decay electrons to have p and p_t with given ε_b. It is normalized in such a way that integration over p and p_t equals to unity. BR is the branching ratio of semileptonic decay. When both quarks of the q $\bar{q}$ pair decay into e$^{+(-)}$+X, there are $N_q \times 2BR$ numbers electrons. Hence we restrict to events with only one electron and use $(1\text{-}BR)$ term to avoid double counting. A_b is the acceptance of b event with one electron. Then the electron spectrum $F(p,p_t)$ can be represented by the sum of contribution flavor as follows.

$$F(p,p_t) =$$
$$N_b\,(1+\delta)_b\,2\,BR_b(1-BR_b)\,P_b(p,p_t,\varepsilon_b)\,A_b$$
$$+\,N_b\,(1+\delta)_b\,2\,BR_{bc}(1-BR_{bc}-BR_b)(1+BR_{c\bar{c}s})\,P_{bc}(p,p_t,\varepsilon_b)\,A_{bc}$$
$$+\,N_b\,(1+\delta)_b\,2\,BR_{b\tau}(1-BR_{b\tau})\,P_{b\tau}(p,p_t,\varepsilon_b)\,A_{b\tau}$$
$$+N_c\,(1+\delta)_c\,2\,BR_c(1-BR_c)\,P_c(p,p_t,\varepsilon_c)\,A_c \qquad (5\text{-}4b)$$

The suffix specifies the processes of b→e+X, b→c+X→e+X'+X, b→τ+X→e+X'+X or c→e+X, respectively. A_q (q=b,bc,bτ,c,) and $1+\delta$ are given in Table 5-2. For BR's, we used their world average taken from the Particle Data Group[3]. ($BR_b=BR$(b→e+X) = 10.8 ±0.5%, $BR_c=BR$(c→e+X) = 9.6 ±0.9%, BR_{bc} = BR(b→c+X) × BR(c→eX)= BR_c , $BR_{c\bar{c}s}=BR$(b→c$\bar{c}$s) = 16%, $BR_{b\tau}$ = BR(b→τ+X) × BR(τ→e+X) = 3% × BR_b.(in CDC acceptance))

Table 5-2 Acceptance of Semileptonic Decay Event

Decay branch	A_q(*), q=b,bc,bτ,c	$1+\delta$
b→e+X	48.1 ±1.8 %	1.13
b→c+X→e+X'+X	33.5 ±1.6%	
b→τ+X→e+X'+X	55.3 ±10.0%	
c→e+X	33.9 ±1.0%	1.33

(*) Requirement of A includes good track in CDC, $|p| \geq 1.0$ GeV/c, $|\cos\theta| < 0.68$ as well as acceptance of the multihadronic event selection.

Though the Peterson fragmentation function is given in equation (1-19), the analytical calculation of $P(p,p_t,\varepsilon)$ is impractical. Instead of varying $\varepsilon_{b,c}$ in Monte-Carlo generation, we use a weighted sum of the $P(p,p_t,i)$ where $P(p,p_t,i)$ is pre-determined probability such that the prompt electron has the momentum p and the transverse momentum p_t with its parent heavy-quark meson having $X_q = 0.125\,i + 0.125$ (i = 1~4). Assuming the Peterson fragmentation function $f(\varepsilon,X_q) = 1/\{X_q(1-\frac{1}{X_q}+\frac{\varepsilon}{1-X_q})^2\}$, we define the weight, $W(\varepsilon,i)$ (i =1~4), as follows.

$$W(\varepsilon,i) = \frac{\int_{X1_i}^{X2_i} f(\varepsilon,X)\,dX}{\int_0^1 f(\varepsilon,X)\,dX} \qquad (5\text{-}5)$$

where $[X1_i, X2_i]$ are chosen as [0.0,0.25], [0.25,0.5], [0.5, 0.75], [0.75,1.0].

$P(p,p_t,\varepsilon)$ are given as

$$P(p,p_t,\varepsilon) = \sum_{i=1\sim4} \{\, P(p,p_t,i)\cdot W(\varepsilon,i) \,\} \qquad (5\text{-}6).$$

We fit the p-p_t spectrum by minimum χ^2 method using the function (5-4b). Free parameters of the fitting are $N_b, N_c, \varepsilon_b, \varepsilon_c$. The spectrum is divided into 4 bins for p and 2 bins for p_t. (p [1.0,3.0],[3.0,5.0],[5.0,10.0],[above 10.0], p_t [0.0, 0.8], [above 0.8] in unit of GeV/c). χ^2 is defined as follows.

$$\chi^2 = \sum_{(\text{all } p\text{-}pt \text{ bins})} \left\{ \frac{N^{corr} - F(p,p_t)}{\delta N^{corr}} \right\}^2 \qquad (5\text{-}7)$$

To estimate the contribution of the systematic error of N^{corr}, we shift the center value of N^{corr} to $N^{corr}\pm$(systematic error). The free parameter $N_b, N_c, \varepsilon_b, \varepsilon_c$ are optimized to minimize χ^2 of the equation (5-1). The fitting result is summarized in Table 5-3 and are shown in Fig.5-4. The systematic error of N^{corr} is given by error propagation of $\varepsilon_{p,\gamma,h}{}^{\gamma}$, $\varepsilon_{p,\gamma,h}{}^{TRD}$ in equation (5-3).

Table 5-3 The p-p_t Fitting Results

N_b=1145.8 $^{+260.3}_{-273.6}$(stat.) $^{+4.7}_{-10.9}$(sys.)
N_c=3149.6 $^{+812.3}_{-743.4}$(stat.) $^{+404.8}_{-351.3}$(sys.)
ε_b=0.135 $^{+0.147}_{-0.125}$(stat.) $^{+0.058}_{-0.061}$(sys.)
ε_c=0.396 $^{+0.443}_{-0.279}$(stat.) $^{+0.086}_{-0.045}$(sys.)

The dominant systematic error comes from the uncertainty of the efficiency in γ-conversion rejection. Since the amount of the subtracted γ-conversion events are large in the lowest p and p_t region. (See Table5-1), the fitting results of N_c, which dominates in this region, has a larger systematic error.

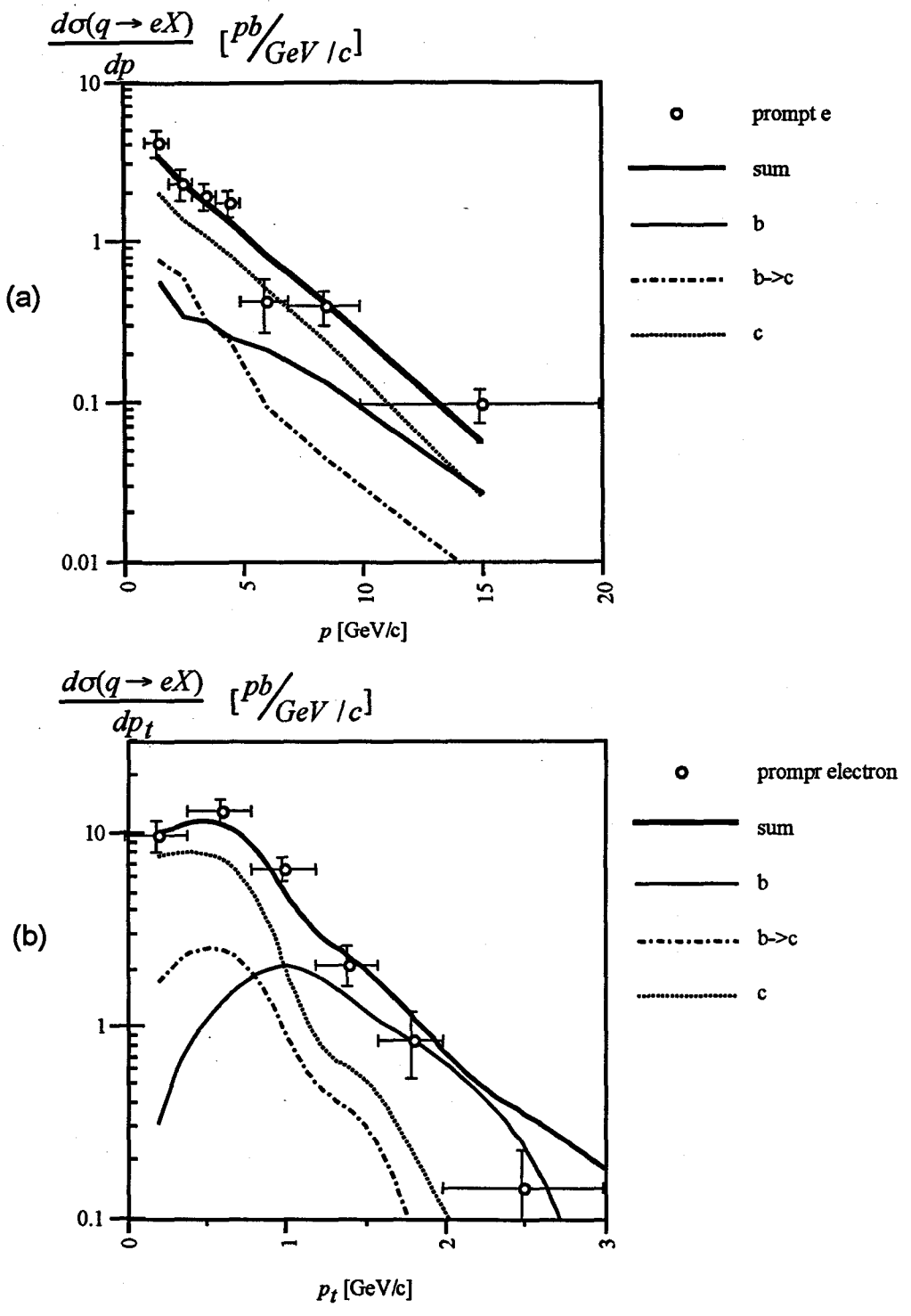

Fig.5-4 Differential Cross Section of $e^+e^- \to q\bar{q}$, $q(\bar{q}) \to e^+(e^-)X$

The differential cross section of $e^+e^- \to q\bar{q}$, $q(\bar{q}) \to e^+(e^-)X$. Circles show observed numbers of prompt electrons. Contribution of b, b cascade and c decay electron which are determined by the fit, are shown.

(a) differential cross section as the function of electron momentum $\frac{d\sigma(q \to eX)}{dp}$ $[\frac{\text{pb}}{\text{GeV/c}}]$, (b) differential cross section as the function of electron transverse momentum $\frac{d\sigma(q \to eX)}{dp_t}[\frac{\text{pb}}{\text{GeV/c}}]$

5.3. Asymmetry of Heavy Quarks

Forward-backward production asymmetry of the heavy quarks can be measured from the angular distribution of jets where the sign of the charge is determined by that of the decay electron.

5.3.1. Angular Distribution

The angular distribution of the quark direction of events which include an electron exhibits forward-backward asymmetry. Firstly, we present results of flavor fractions obtained by fitting p-p_t spectrum in the previous section. Secondly, we give a definition of the quark direction and present the observed angular distribution. Finally, we give acceptance corrected angular distribution and interpret it in terms of the asymmetry of quark production.

Fraction of b/c Quark

The fraction of b and c quark in our electron inclusive sample in the regions of p_t <0.8 or >0.8 GeV/c can be estimated by integrating the spectrum shown in Fig.5-4. Table 5-4 summarize the fraction of the b, b cascade and c decay in our sample.

These fractions are strongly correlated. Hence we did not present the systematic error as the "$x \pm \delta x(sys.)$". The table shows that the c quark forward-backward asymmetry is significant in low p_t region and b asymmetry, high p_t region. This result is consistent with the Monte-Carlo prediction (See Appendix-2).

Table 5-4 Fraction of The Each Flavor

	f_b [%]	f_{bc} [%]	f_c [%]
p_t < 0.8 GeV/c	9.9 ±0.9(stat.)(*)	18.8 ±0.2	71.3 ±0.7
Systematic –	+0.9	+0.6	-2.5
+	-1.0	-1.7	+2.7
p_t > 0.8 GeV/c	58.6 ±2.2	12.1 ±0.7	29.3 ±1.6
Systematic –	+1.7	+0.5	-2.2
+	-2.1	-0.5	+2.6

(*) Errors in the upper row are statistical.

Definition of Quark direction

We use thrust axis of multihadronic event as the quark direction. The definition of the thrust and jet axis is given in Appendix-2. Fig.5-5 is Monte-Carlo prediction of the angle between real quark direction which is generated and reconstructed thrust axis. The average of difference of them is 5.3° (1σ).

The charge of the decay lepton reflects the charge of its parent quark. ($c(+2/3) \rightarrow e^+ s(-1/3)$, $\bar{c}(-2/3) \rightarrow e^- \bar{s}(1/3)$, $b(-1/3) \rightarrow e^- c(+2/3)$ and $\bar{b}(+1/3) \rightarrow e^+ \bar{c}(-2/3)$). We define the quark charge direction as shown in Fig.5-6. Thrust axis has no polarity by definition. We define the direction of the thrust axis toward the hemisphere which includes the electron. The angle between this direction and e^- beam direction is defined

as θ_{thrust}. The quark charge angle $\cos\theta_{q(+)}$ is given as $-Q\cos\theta_{thrust}$ where Q is the charge of tagged lepton. It is noted that the quark charge direction gives the direction of $\bar{c}$-quark (not c-quark) or b-quark. Therefore, the observed charge asymmetry for c-quark should have opposite sign to that for b-quark.

The angular distribution of observed events (N_{obs}) in the definition above is shown in Fig.5-7. The background (N_h, N_γ) is displayed as histograms. These backgrounds are calculated using the fraction and its error obtained Table 5-1.

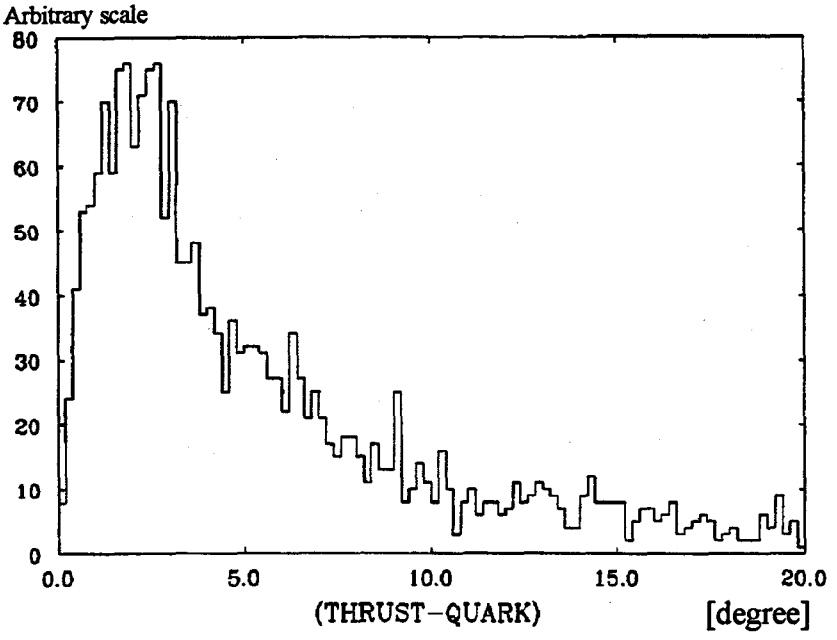

Fig.5-5 Angle between Quark Direction and Thrust Axis

Figure shows the distribution of the angle between thrust axis and quark direction with Monte-Carlo. The quark direction is known in Monte-Carlo generation process, and the thrust axis is reconstructed after simulation of VENUS detector system. The deviation is 5.3 degree in 1σ.

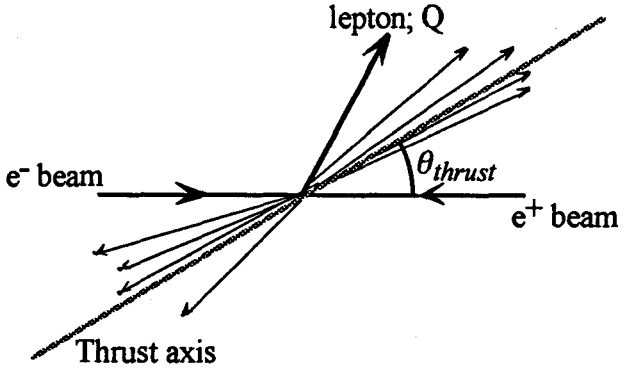

Fig.5-6 Definition of Quark Direction

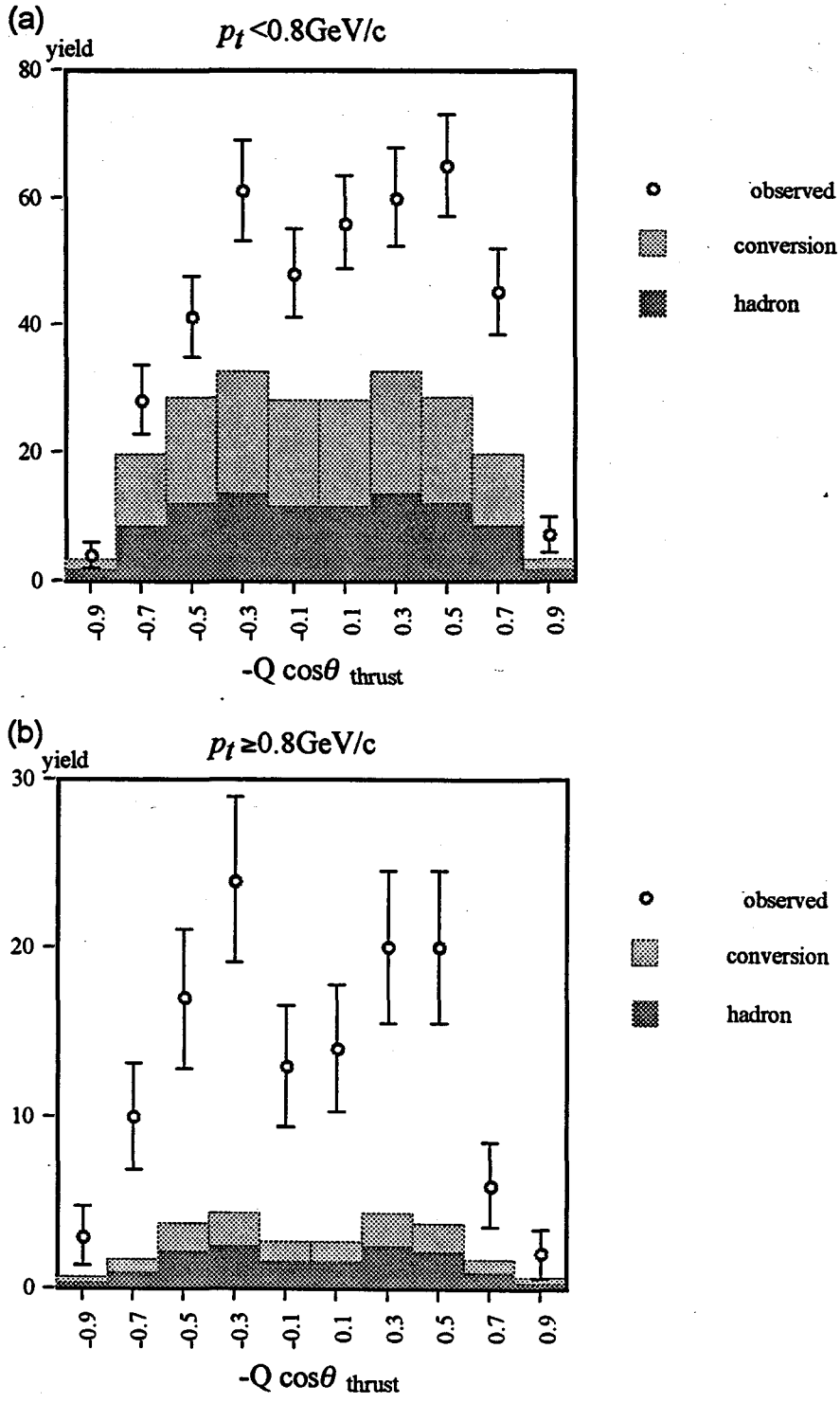

Fig.5-7 Distributions of $-Q\cos\theta_{thrust}$ of Electron Inclusive Event

The angular distribution of -Q $\cos\theta_{thrust}$ of electron inclusive event.. The open circles are observed numbers without background subtraction (N_{obs}). The histogram shows the hadron background (N_h, dark gray) and conversion electron (N_γ, light gray).. The prompt electron is the difference between circles and histograms. (a) with p_t <0.8 GeV/c and (b) with p_t ≥0.8 GeV/c

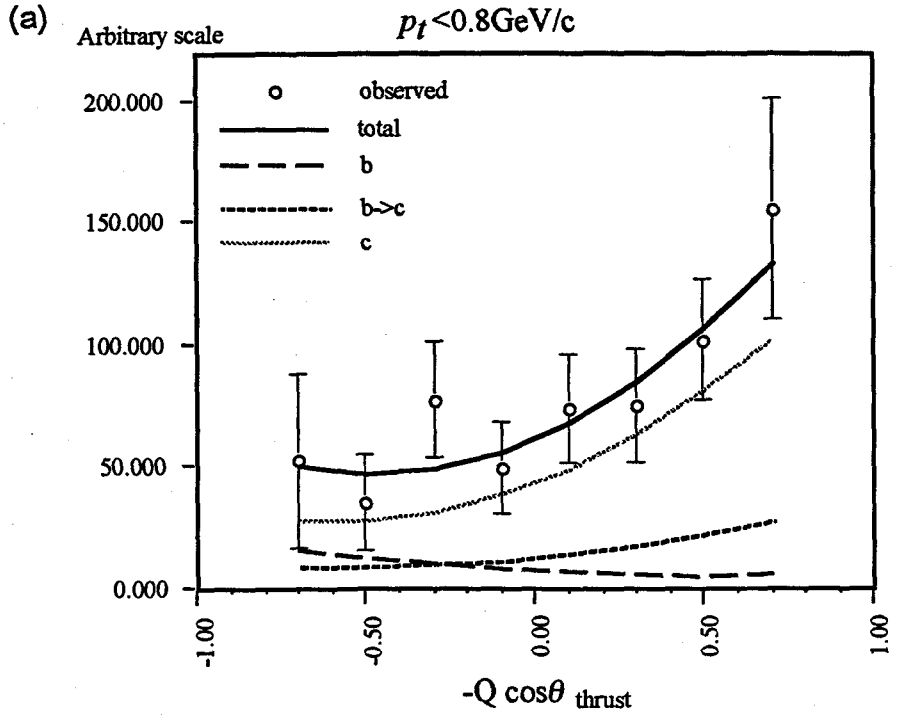

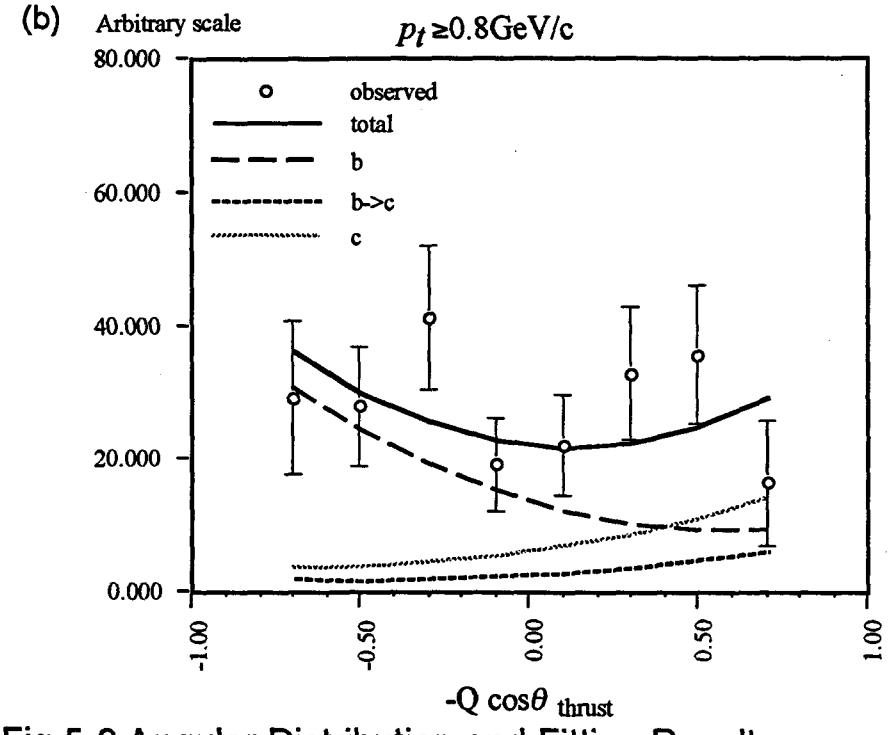

Fig.5-8 Angular Distribution and Fitting Result

Figure presents the angular distribution of prompt electron inclusive events after correction of geometrical acceptance and background subtraction. The fitting results of the distribution with equation (5-7,8) are displayed in the figure. In the distribution of low p_t region, we can see the c-quark asymmetry clearly.

The error bar of Fig.5-7 is statistical only. The angular distribution should be corrected for the detector acceptance as function of quark direction θ. The acceptance corrected distribution is given in Fig.5-8.

5.3.2. Asymmetry Fitting

The angular distribution of the quark is given by equation (1-3,12). The observed distributions in Fig.5-8 can be regarded as a linear combination of b and c quark distribution with known coefficients.

$$A(\cos\theta) = N\{ f_b\,(1+\cos^2\theta + \frac{8}{3} A_{FB}^b \cos\theta) + f_{bc}\,(1+\cos^2\theta - \frac{8}{3} A_{FB}^b \cos\theta)$$

$$+ f_c\,(1+\cos^2\theta - \frac{8}{3} A_{FB}^c \cos\theta)\} \qquad (5\text{-}8)$$

As mentioned in the previous section, the sign of A_{FB} for the charm quark is reversed. We fit the angular distributions shown in Fig.5-8 by χ^2 minimization to the equation (5-8) with f_b, f_c and f_{bc} constrained to the value presented in Table 5-4. χ^2 is defined as follows.

$$\chi^2 = \sum_{(pt<0.8 \text{ and } pt>0.8 \text{ GeV/c})} \left\{ \frac{A_{observed} - A_{expected}}{\delta A_{observed}} \right\}^2 \qquad (5\text{-}9)$$

χ^2 fitting should be done with the distribution of p_t <0.8 and >0.8 GeV/c region simultaneously. Free parameters are b and c quark asymmetry A_{FB}^b, A_{FB}^c and normalization factor of each region $N(p_t<0.8), N(p_t>0.8)$.

Curves in Fig.5-8 show fitting results presenting the contribution of each flavor. Fig.5-9 indicates the amount of the systematic error. The corresponding error in the asymmetry is estimated by varying the data by this amount. The asymmetry is calculated to give.

$$A_{FB}^b = -0.48 \pm 0.28 \text{ (stat.)} \pm 0.03 \text{ (sys.)}$$

$$A_{FB}^c = -0.45 \pm 0.18 \text{ (stat.)} \pm 0.02 \text{ (sys.)}$$

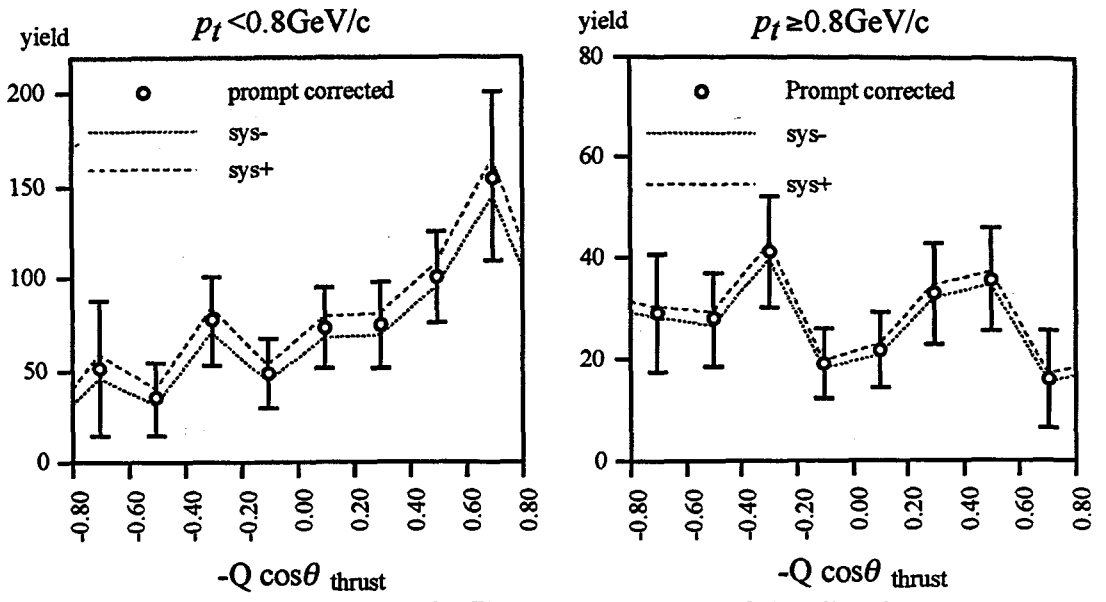

Fig.5-9 Systematic Error of Angular Distribution

Systematic errors of the angular distribution after correction of geometrical acceptance. Circle symbols and their error bar show the center value and statistical error. The dotted and solid line shows the range of systematic error.

References of this Chapter

[1]Particle Data group, Phys.Rev. D45(1992)

[2]J.Fujimoto and Y.Shimizu, Mod. Phys. Lett A3(1988)581

[3]Particle data group, Phys.Rev. D45(1992)

ARGUS collab., H.Albrecht et al., Phys.Lett. **B249**(1990)359

CLEO collab., S.Henderson et al., Phys.Rev. **D45**(1992)2212

Chapter 6
Discussion & Conclusion

In this chapter, we correct the observed values in previous chapter with QED, QCD radiative effect and compare with other experiments. For the forward-backward asymmetry of b qaurk, we must consider about B-$\bar{B}$ Mixing. The present measurement gives the first results of cross section, fragmentation function and asymmetry of c-quark using semileptonic decay electron in TRISTAN energy region.

6.1. Cross Section of Heavy Quarks

The cross section of the b and c quark pair production can be calculated directly from N_b,N_c and integrated luminosity (74.6±0.5±1.9 pb^{-1}). The measured total cross sections are following.

	This experiment	Standard Model
σ_b	$= 15.4\ ^{+3.5}_{-3.7}$(stat.) ±0.4(sys.) [pb]	15.8 [pb]
σc	$= 42.2\ ^{+10.9}_{-10.0}$(stat.) $^{+5.5}_{-4.8}$(sys.)[pb]	41.1 [pb]

$R_{b(c)}$ value is defined as the ratio of the cross sections.

$$R_{b(c)} = \frac{\sigma_{b(c)}}{\sigma(e^+e^- \rightarrow \mu^+\mu^-)} \qquad (6\text{-}1)$$

$\sigma(e^+e^- \rightarrow \mu^+\mu^-)$ is the QED first order cross section of muon pair production (= 25.8pb at $\sqrt{s}$ = 58GeV). Rb and Rc are obtained as

	This experiment	Standard Model
Rb	$= 0.60$ ±0.14(stat.) ±0.02(sys.)	0.61
Rc	$= 1.64\ ^{+0.42}_{-0.39}$(stat.) $^{+0.21}_{-0.19}$(sys.)	1.59

The measured results are consistent with the standard model predictions.

6.2. Fragmentation Function

The fragmentation of the b and c quarks can be expressed as Peterson fragmentation function, $f(X_q, \varepsilon)$, as presented in equation (1-19). The mean of X_q (energy fraction of q-hadron) distribution is also used to present the measurement of the fragmentation function. It is given as follows and presented in Fig.1-5.

$$\langle X_q \rangle = \frac{\int f(X_q, \varepsilon) X_q \, dX_q}{\int f(X_q, \varepsilon) dX_q} \tag{6-2}$$

Using the fitting result of ε_b, ε_c, the $\langle X_b \rangle$, $\langle X_c \rangle$ are calculated as,

$$\langle X_b \rangle = 0.60 \, ^{+0.19}_{-0.07}(\text{stat.}) \, ^{+0.02}_{-0.03}(\text{sys.})$$

$$\langle X_c \rangle = 0.50 \, ^{+0.11}_{-0.08}(\text{stat.}) \, ^{+0.01}_{-0.02}(\text{sys.}).$$

Previously reported values are $\langle Xb \rangle = 0.70 \pm 0.02$ and $\langle Xc \rangle = 0.51 \pm 0.02$ which were measured mainly at low energy ($\sqrt{s}$~30GeV at PEP or PETRA[1]). Our results are consistent with them.

6.3. Forward-Backward Asymmetry

6.3.1. Initial Radiation and QCD Correction

The observed asymmetry should be corrected for the higher order effects in QED (initial photon radiation) and QCD[2]. We already described them in Chapter-1. Now we correct observed data at $\sqrt{s}$ = 58 GeV. Moreover, the b asymmetry will be suppressed by $B^0\bar{B}^0$ mixing. we correct these factors and compare our result with the standard model prediction.

Note: QED radiative correction for cross section was already included in the equation (5-2) using a term $(1+\delta)_{b,bc,b\tau,c}$. However, it has not been done in angular distributions of events. In a measurement of forward-backward asymmetry, the observed value should be correctted with both QED and QCD correction.

Initial Radiation Correction

The effective e^+e^- colliding CM energy is slightly reduced by the photon radiation that was described in Chapter-1. Therefore, the effective CM energy after hadronic event selection is slightly lower than the $2E_{beam}$. The average energy shift is 2.0 GeV for b quark event and 2.6 GeV for c quark event. The asymmetries at these effective CM energy are different from those at $\sqrt{s}$ = 58 GeV. The correction factor is given as $\frac{A_{FB}^{expected}(\text{at } \sqrt{s} = 58 \text{ GeV})}{A_{FB}^{expected}(\text{at effective } E_{CM})}$ in the standard model calculation. This is 1.01 for b and 1.06 for c quark asymmetry.

QCD Correction

A hard gluon emission deflects the quark direction and, therefore, smears the asymmetry. We calculate 1st order QCD effect for asymmetry[3]. The correction factor is 1.05 for b quark and 1.04 for c quark asymmetry.

The QED and QCD corrected value for the asymmetry is shown in Table 6-1.

6.3.2. $B^0\bar{B}^0$ Mixing

The b quark meson B^0 can make a transition to $\bar{B}^0$ through box diagrams shown in Fig.6-1. This transition is called as B^0B^0 mixing. B^0 B^0 mixing changes the observable charge asymmetry of b-quark because the b-quark charge is identified after the transition. The B^0B^0 mixing smears the asymmetry of b quark. The mixing parameter, χ, is defined to show the mixing effect against the charge asymmetry explicitly,

$$\chi = \frac{\Gamma(B^0 \to \bar{B}^0 \to e^- X)}{\Gamma(B^0 \to e^+ X) + \Gamma(B^0 \to \bar{B}^0 \to e^- X)} \qquad (6\text{-}3)$$

χ is different for B_d^0 and B_s^0 mesons. Averaging the mixing parameters for Bd and Bs, the value of 0.129 ± 0.022, is used according to recent results of LEP experiments[4]. The b asymmetry after mixing is calculated as Table 6-1 at $\sqrt{s}$ = 58 GeV.

The present measurements agree well with the standard model prediction. Fig.6-2 shows the prediction and previous results[5] as well as ours.

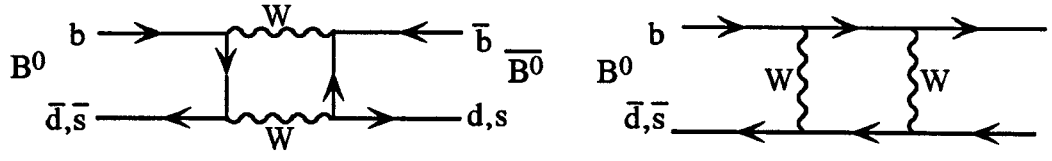

Fig.6-1 Box Diagram for $B^0\bar{B}^0$ Mixing

Table 6-1 Measured & Standard Model Prediction of Asymmetry

	observed	QED,QCD corrected	Standard Model prediction
b asymmetry	-0.48±0.28±0.03	-0.51 ±0.29 ±0.03	-0.42 (with $B^0\bar{B}^0$ mixing. χ=0.129)
c asymmetry	-0.45±0.18±0.02	-0.50 ±0.20 ±0.02	-0.47

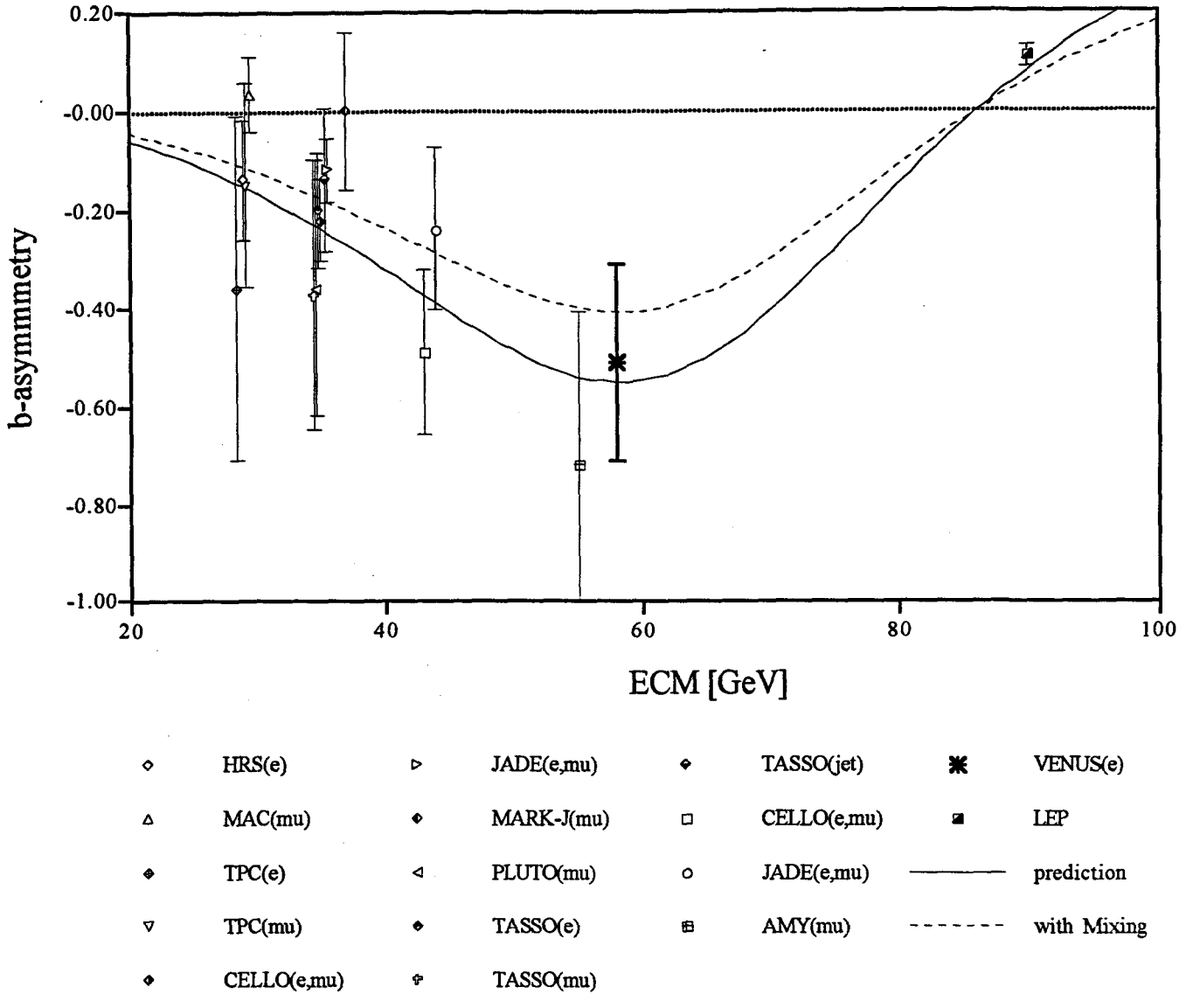

Fig.6-2 FB Asymmetry of b and c quark (a) FB asymmetry of b quark production

Dashed line in Fig.6-2(a) shows the prediction of asymmetry with B^0 $\bar{B}^0$ mixing using parameter χ=0.129.

The signature of b quark asymmetry means that b is not 'isospin singlet' in third generation of quarks. It suggests existence of t (top) quark as an partner of b quark in 'isospin doublet'.

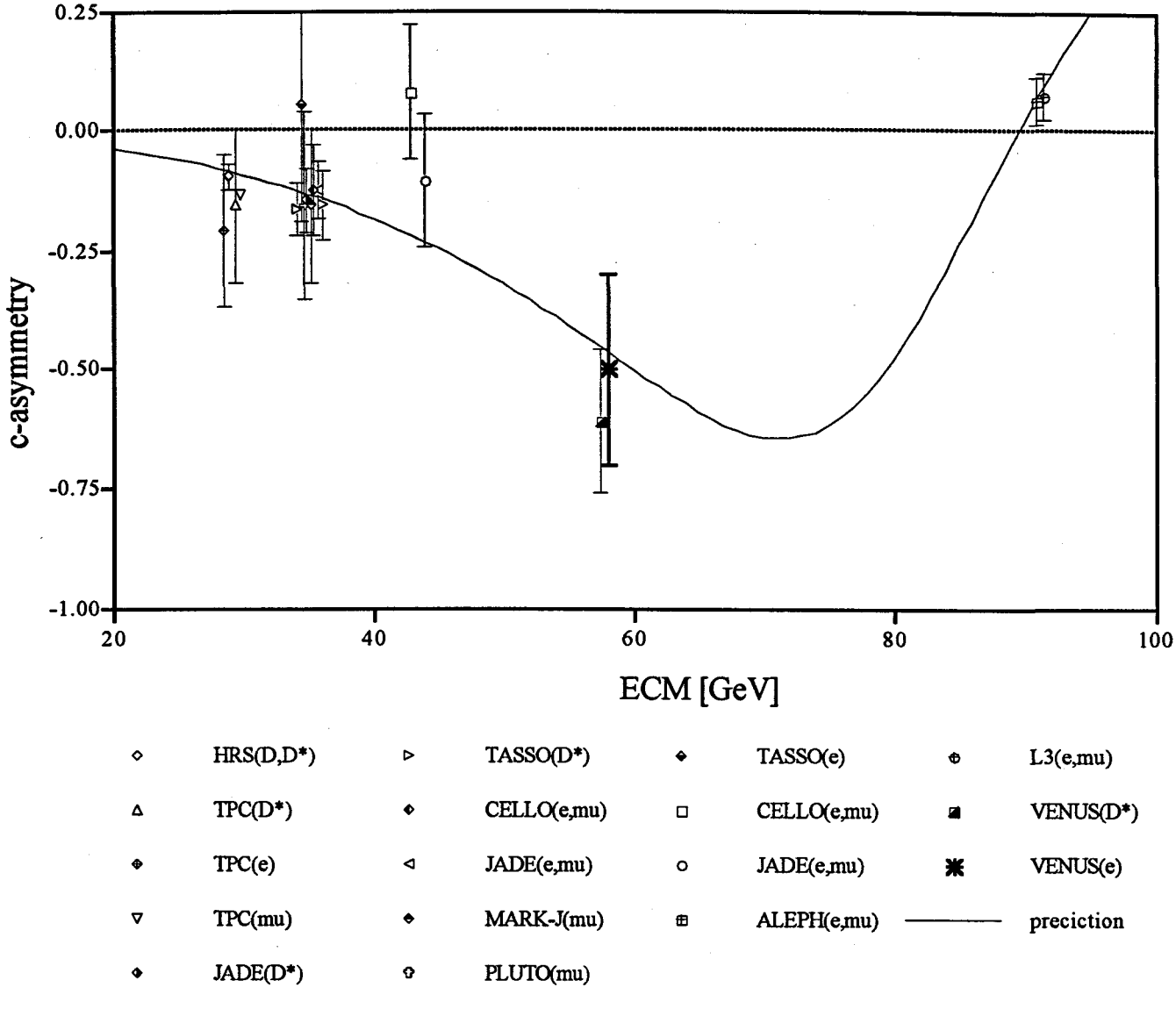

Fig.6-2 FB Asymmetry of b and c quark (b) FB asymmetry of c quark production

The forward backward production asymmetry of b/c quark. The figure displays the measurement of asymmetry with various methods. Our measurement results presented in the text are shown by the symbol (✱).

In Fig.6-2, ▣-symbol shows a result of study with charged D^* production in VENUS experiment[6]. The study use soft (= low p_t) charged π from decay of $D^{*\pm} \rightarrow D^0\pi^\pm$ and mass difference method. Experimental data of it (~153pb^{-1}) contain that of this thesis (~74pb^{-1}). Since about 20% of D^* events are semileptonic decay event, a combination of these results is not trivial. We got consistent results with independent two methods for tagging c quark event.

6.4. Conclusion

We have measured the forward-backward production asymmetry, cross section and fragmentation parameter of b,c quark simultaneously using electrons from semileptonic decay of b or c quark. It is noted that these include the first measurements for c quark using semileptonic decay electron at the TRISTAN energy. VENUS has shown enough power of electron identification to study not only b but also c quark. We summarize the final results of the measurement again.

Cross section & R value

	Standard Model
$\sigma_b = 15.4\ ^{+3.5}_{-3.7}(\text{stat.}) \pm 0.4(\text{sys.})$ [pb]	15.8 [pb]
$\sigma_c = 42.2\ ^{+10.9}_{-10.0}(\text{stat.})\ ^{+5.5}_{-4.8}(\text{sys.})$	41.1 [pb]
$Rb = 0.60 \pm 0.14(\text{stat.}) \pm 0.02(\text{sys.})$	0.61
$Rc = 1.64\ ^{+0.42}_{-0.39}(\text{stat.})\ ^{+0.21}_{-0.19}(\text{sys.})$	1.59

Forward-backward production asymmetry

	Standard Model
A_{FB}^b = -0.51 ±0.29 (stat.)±0.03 (Sys.)	-0.42 (with $B^0\bar{B}^0$ mixing)
A_{FB}^c = -0.50 ±0.20 (stat.)±0.02 (Sys.)	-0.47

These results are consistent with predictions of standard model.

Mean energy fraction of b- or c-hadron $\langle Xq \rangle$

$$\langle X_b \rangle = 0.60\ ^{+0.19}_{-0.07}(\text{stat.})\ ^{+0.02}_{-0.03}(\text{sys.})$$

$$\langle X_c \rangle = 0.50\ ^{+0.11}_{-0.08}(\text{stat.})\ ^{+0.01}_{-0.02}(\text{sys.})$$

The fragmentation of b-quark measured as harder than c-quark. This result is similar to previous experiments[1].

References of this Chapter

[1]DELCO collab., W.Bacino et al., Phys.Rev.Lett 43(1979)1073

MARK-III collab., R.M.Baltrusaitis et al., Phys.rev.Lett 54(1985)1976

ARGUS collab., H.Albrecht et al., Phys.Lett.**B249**(1990)359

CLEO collab., S.Henderson et al., Phys.Rev. **D45**(1992)2212

[2]H.A.Olsen, P.Osland, I.Overbo, Nucl.PhysB171(1980)209

E.Laermann, K.H. Streng, P.M.Zerwas, Z.Phys. C3(1980)289

[3]Applequist T and Politzer D, Phys.rev.**D12**(1975)1404

Pennington M R, "Cornerstones of QCD", Repts.on Progr.in Phys.46(1983)393

Jersàk J et al., Phys.Lett.**98B**(1081)363

[4]OPAL collab., P.D.Acton et al., Phys.Lett. B276(1992)379

ALEPH collab., D.Decamp et al., Phys.Lett. B258(1992)236

L3 collab., B.Adeva et al., Phys.Lett B288(1992)395

[5]H.Kroha, MPI-PAE/Exp.El 227 July 1990

AMY collab., H.Sagawa et al., Phys.Rev.Lett 63(1989)2341

JADE collab., W.Bartel et al., Phys.Lett B 146(1984)437

HRS collab., C.R.Ng et al., ANL-HEP-PR-88-11, Nov.1988

MAC collab., H.R.Band et al., Phys.Lett B218(1989)363

TCP collab., H.Aihara et al., Z.Phys. C27(1985)39

TCP collab., H.Aihara et al., Phys.Rev. D31(1985)2719

CELLO collab., H.J.Behrend et al., DESY 89-125, Sept.1989

JADE collab., E.Elsen et al., Z. Phys.C46(1990)349

MARK-J collab., see compilation in S.L.Wu, Proc. 1987 Int. Symposium on LEpton and Photon Interactions at HIgh energies, Hambrug, Nucl.Phys.B(proc.Suppl.) 3(1988)39

C.Maxeiner, PLUTO collab., Ph.D thesis, DESY PLUTO-85-03, March 1985

TASSO collab., M.Althoff et al., Z.Phys. C22(1984)219

P.Rehders, TASSO collab. Ph.D. thesis, DESY F1-89-02, July 1989

J.M.Pawlak, TASSO collab. Ph.D. thesis, DESY F1-88-01, sept. 1988

ALEPH collab., Phys.Lett B244(1990)551, B263(1991)325

OPAL collab., M.Z.Akrawy et al., Phys.Lett. B241(1990)416; O.Adrian et al., Phys.Lett. B292(1992)454

L3 collab., B.Adeva et al., Phys.Lett. B263(1992)311

DELPHI collab., P.Abreu et al., Phys.Lett. B276(1992)536; Z.Phys. C56(1992)47

[6]VENUS collab. F.Hinode et al.,KEK Preprint 92-194 submitted to Phys.Lett.,B

Appendices

A-1. Sample Events for Electron & Hadron

A-1.1. 'Single Electron' Event

'Single electron' event is taken from the process ($e^+ e^- \rightarrow e^+ e^- \gamma$). When one electron (positron) or the photon in the final state goes in the beam pipe direction, the other electron(s) has a large transverse momentum from the beam direction (See Fig.A1-1). This electron can be accepted by CDC, TRD and LG. In this case, the only one charged track is measured in the detector. We call this event as 'single electron'.
The 'single electron' selection is as follows.

1. Only 1 good track is found in CDC
2. $|p| \geq 1.0$ GeV/c
3. $|\cos\theta_{track}| < 0.68$
4. $E/p \geq 0.8$

The E/P distribution of the 'single electron' event is shown in Fig.A1-3(a)

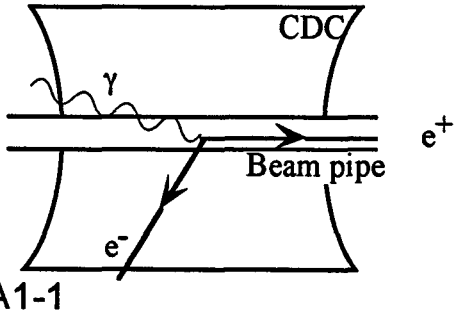

Fig.A1-1
Event Topology of "Single Electron"

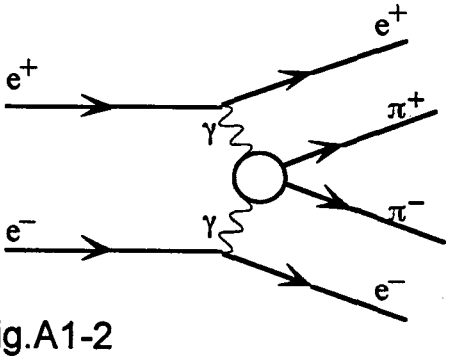

Fig.A1-2
Diagram of $e^+e^- \rightarrow e^+e^-\pi^+\pi^-$

A-1.2. $e^+e^- \rightarrow e^+e^- \pi^+\pi^-$ Event

To obtain pure hadron tracks, the process of $e^+e^- \rightarrow e^+e^- \pi^+\pi^-$ is tagged by following criteria. We select 2-prong events where e^+e^- in the final state go in the beam direction.

1. Only 2 good tracks are found in CDC
2. At least one track momentum should be $|p| \geq 1.0$ GeV/c
3. $|\cos\theta_{track}| < 0.68$
4. $E/p \leq 0.4$

We use the track whose momentum ≥1GeV/c as a sample of hadrons to test the TRD and LG response. The E/P distribution of the π sample is shown in Fig.A1-3(b).

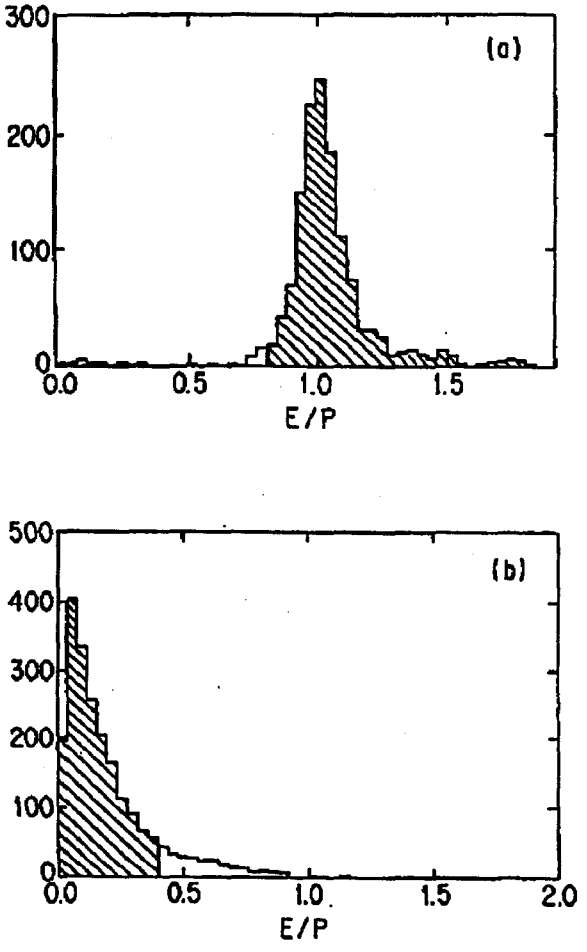

Fig.A1-3 *E/p* Distribution of 'single electron' and Low Multiplicity Event

(a) 'single electron', (b) $e^+e^- \rightarrow e^+e^- \pi^+\pi^-$ event. The hatched region used as is the sample of 'single electron' and low multiplicity π referred in the main text.

A-2. Jet Clustering & p_t Distribution of Electron

We give a definition of jet clustering and thrust axis which are used to recognize a hadron jet. Moreover, enrichment of the b flavor in high p_t region with proper choice of the parameter of jet clustering will be presented.

A-2.1. Definition of Jet Clustering and Thrust axis

Jet Clustering

In order to find the direction of mother quark in semileptonic decay, the jet clustering method was used. The adopted algorithm is the one used by JADE collaboration[1]. In multihadronic events, the scaled invariant mass squared is calculated for all pairs of particle i and j.

$$y_{ij} = \frac{M_{ij}^2}{E_{det}^2} \tag{A2-1}$$

where E_{det} is the total energy of observed particles with assumption that the charged particle is π and neutral one is photon. The particle pair with smallest invariant mass is regarded as a pseudo-particle called cluster with 4-momentum P_i+P_j., where P_i and P_j are 4-momentum of i-th and j-th particle. This procedure is repeated until the scaled invariant mass of all (pseudo-)particles exceed a certain threshold value y_{min} called the jet resolution parameter.

$$y_{ij} \geq y_{min} \tag{A2-2}$$

The remaining pseudo-particles are called as jets. A jet axis is given as the direction of its direction. In this thesis, we choose $y_{min} = 0.05$ for the reason which is given in the next section. The value p_t is given as the transverse momentum from the axis of the jet which the particle belongs to.

Thrust Axis

The thrust(T) is one of popular variables which characterize global shape of the event. They are defined by following equation.

$$T = \max \frac{\Sigma |\boldsymbol{p}_i \cdot \boldsymbol{n}|}{\Sigma |\boldsymbol{p}_i|} \qquad \text{(A2-3)}$$

where $\boldsymbol{n}$ is an unit vector to be determined so as to maximize the value of T. The direction of the resultant **n** is called thrust axis. When the thrust(T) has a value near 1, the event shape is expected to be collinear.

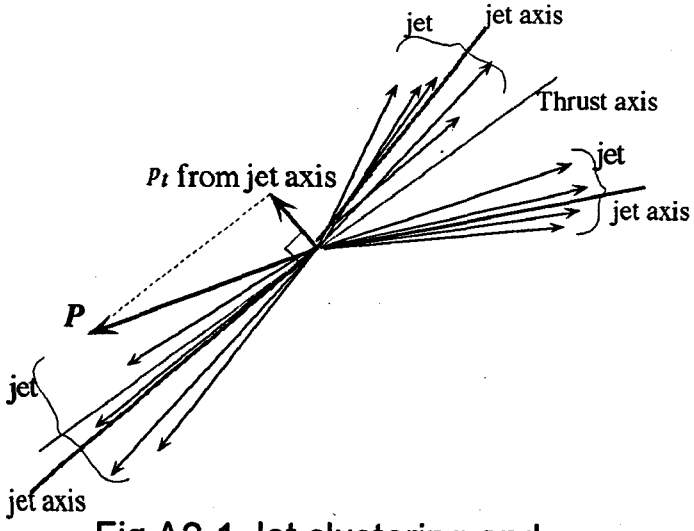

Fig.A2-1 Jet clustering and p_t

Figure shows the idea of jet clustering and thrust axis. p_t from jet axis is defined as the transverse component of the momentum from jet axis which the particle belongs to.

A-2.2. Flavor Enhancement By Jet Clustering

To optimize purity of b quark event sample, we compare the thrust axis and the jet axis determined by the jet clustering as a reference axis in the p_t calculation.We compare results using various clustering methods where

(1) Thrust axis issued as the reference

(2) $y_{min} = 0.02$

(3) $y_{min} = 0.05$ and jet axis is used as the reference

(4) $y_{min} = 0.10$

in calculating p_t.. In general, there are more than jet axis in an event. In sure cases, we choose one which contains an electron. Fig.A2-2 shows the numbers and purity of b in electron sample with $p_t \geq 0.8$ GeV/c .We choose the jet clustering with y_{min} = 0.05 for the analysis of b,c properties in this thesis.

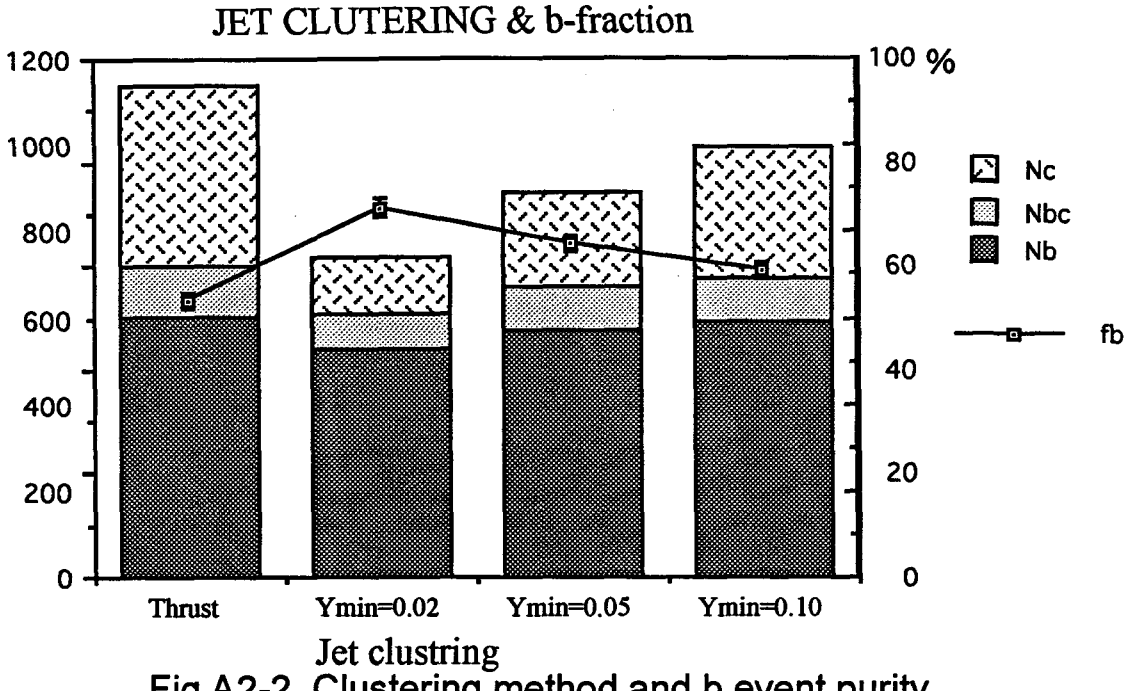

Fig.A2-2 Clustering method and b event purity

Bars show numbers of electrons from b(Nb), b cascade (Nbc) and c(Nc) decay. They depend on the jet clustering method. Names under each bar corresponds to following four clustering methods: thrust, jet clustering choosing y_{min}=0.02, 0.05 and 0.10.

Line shows b fraction with p_t greater than 0.8 GeV/c. These estimation is obtained by Monte-Carlo.

A-3. γ-conversion & Dalitz Decay Rejection

Electrons converted from γ were suppressed by the following method[2] .

A-3.1. Character of Conversion Electrons

Photons would be converted to electron-positron pairs in the material. The probability of conversion is decided by the thickness (= radiation length) of the material the photon traverses. For high energy photon, almost all photon reactions are e^+e^- pair productions. The γ-conversion probability is expressed as

$$I = I_0\,[1\text{-}\exp\,(-\frac{7x}{9X_0})] \qquad \text{(A3-1).}$$

where X_0 is the radiation length, x is the thickness of the material. The length $7/9X_0$ is called as 'conversion length'.

There are some remarkable characteristics of the e^+e^- pair from the γ-conversion. One is small invariant mass of the electron and positron pair, because the photon is a massless particle. The other is that the vertex of the tracks (=γ-conversion point) should be in the material such as wall of the detector. Therefore, e^+ or e^- tracks tend to be separate from the interaction point of the electron-positron collision, while the momentum vector of the e^+e^- pair should be traced back to the interaction point. Fig.A3-2 is an example of the candidate of e^+e^- pair from conversion which is selected by conversion finding algorithm described in the next section. The vertex (= the closest point of 2 tracks) is on CDC inner wall.

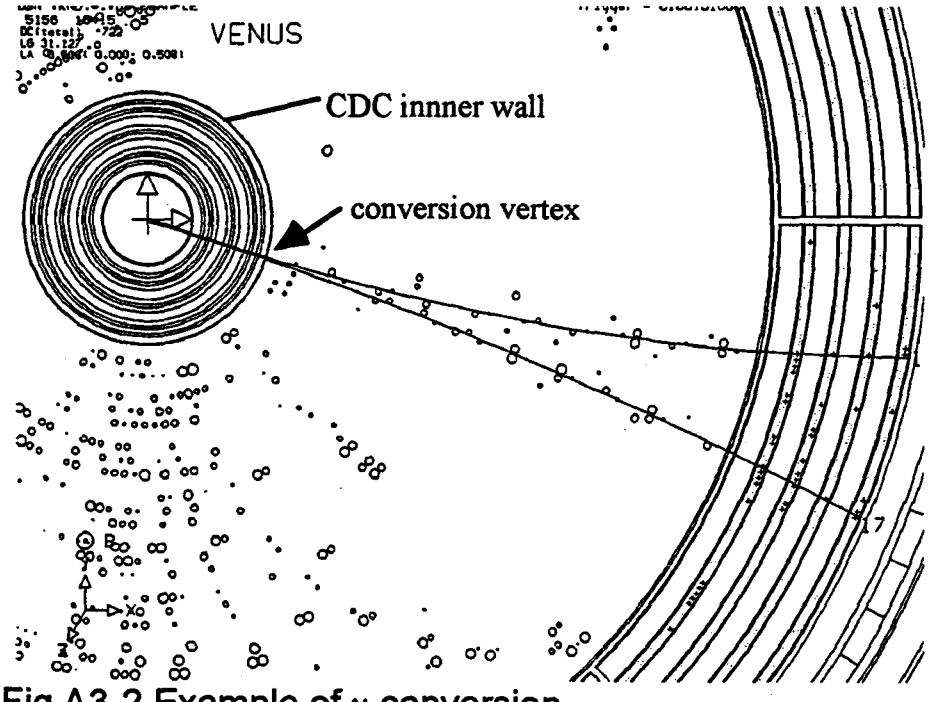

Fig.A3-2 Example of γ-conversion

An example of γ-conversion event which is selected by conversion finding algorithm. Both tracks pass the selection criteria of the electron identification. The conversion vertex (= closest point of two tracks) is on CDC wall.

A-3.2. Finding Algorithm & Performance

The selection parameters are follows.

1. M_{ee}
   Reconstructed invariant mass of the two tracks assuming the electron mass for each track. The vertex is defined as the crossing point of the two tracks or the closest point of the two tracks when they are separated. (See Fig.A3-3b)

2. θ_{conv}
   The angle between the two tracks at the vertex point. It is strongly related to the invariant mass and represents the separation of the two track direction.

3. α
   The angle between the momentum sum of two tracks and the direction vector from interaction point to the conversion point.

4. Δ
   The distance between the two tracks. The distance is defined as negative when the two tracks cross as shown in the right figure of Fig.A3-3(b).

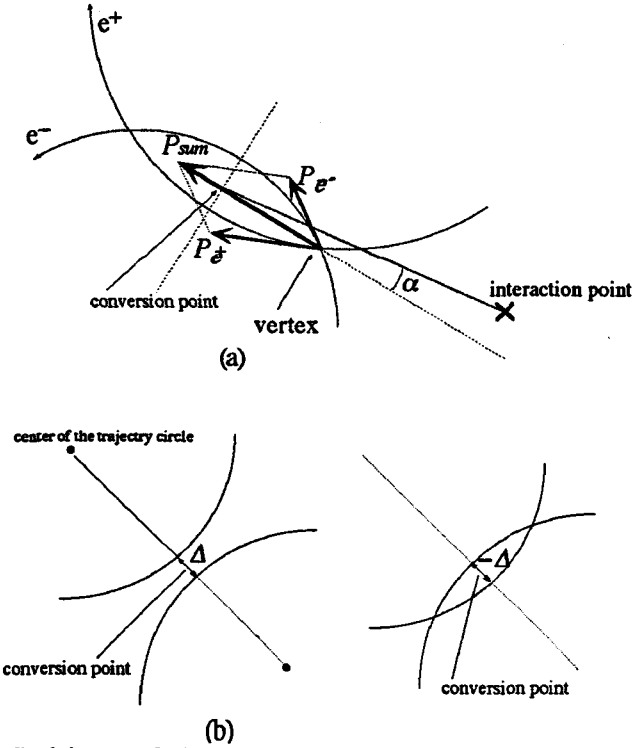

Fig.A3-2 Definition of the Parameters for γ-conversion Finding

Fig.A3-3 shows the definition of the parameters. The conversion point is defined as the mid point between two trajectories when they are in parallel.

When an electron candidate is found, all combinations of electron candidates with opposite charge are tested by the γ-conversion finding algorithm. If at least one combination satisfies the criteria, they are identified as the e^+e^- pair from γ-conversion or Dalitz decay. The algorithm of the γ-conversion finding consists of three categories. The first is for the 3-dimensional reconstructed tracks. If both of the tracks are reconstructed in 3-dimension by CDC, the parameters which are defined below are checked with the following criteria.

1. $\cos\theta_{conv} < 0.85$
2. $\alpha < 0.15$ [rad]
3. $\Delta < 1.5$ [cm]
4. $Mee < 200$ [MeV/c^2]

The track pair which satisfies the above four conditions, is identified as the γ-conversion electrons. The second is the 2-dimensional finding. If the one of the tracks is not reconstructed in 3-dimension, the following criteria are checked.

1. $\cos\theta_{conv} < 0.95$
2. $\alpha < 0.15$ [rad]
3. $\Delta < 1.0$ [cm]
4. $Mee < 200$ [MeV/c^2]

If the pair satisfies all four conditions, it is identified as the γ-conversion electrons.

The third is to use the information of the electron candidate itself. The electron candidates whose R_{min} (the closest approach to the interaction point defined in Chapter-3) are less than –0.3 cm are regarded as the γ-conversion electron (See Fig.A3-3).

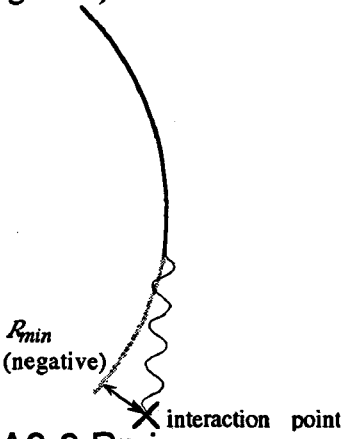

Fig.A3-3 Rmin for Conversion Electron

With the algorithm, the rejection efficiency of the γ-conversion electron (ε_γ) is ~90% while the loss of prompt electrons (ε_p) is ~13% for $|P| > 1$GeV/c and $|\cos\theta| < 0.68$. The efficiencies are summarized in Table A3-1. Fig.A3-4 shows the vertex distribution of conversion candidates in real events (points) and Monte-Carlo prediction (histogram). Peaks of the distribution correspond to beam pipe, trigger chamber and CDC inner wall. This shows that Monte Carlo estimation of the conversion is reliable.

Table A3-1 Efficiency of γ-conversion Finding Algorithm

	p = 1~3 GeV/c	3~5 GeV/c	5 ~ GeV/c
p_t < 0.8 GeV/c	ε_γ = 82.0 ±1.0 % ε_p = 26.4 ±0.3 %	ε_γ = 69.4 ±3.3 % ε_p = 16.7 ±0.4 %	ε_γ = 56.8 ±5.3 % ε_p = 12.7 ±0.5 %
≥ 0.8 GeV/c	ε_γ = 59.8 ±5.4 % ε_p = 8.7 ±0.4 %	ε_γ = 64.2 ±6.6 ε_p = 8.9 ±0.6 %	ε_γ = 61.1 ±8.1 ε_p = 8.8 ±0.6 %

ε_γ; efficiency for conversion electron, ε_p; efficiency for the prompt electron and hadrons. ε_γ is estimated with Monte-Carlo simulation using JETSET7.3 + VENUS detector full simulator. ε_p is calculated from the hadron track in real multihadronic event. ε_p and ε_{hadron} are assumed to be equal. Monte Carlo study shows that the effect of bremsstrahlung of electrons is negligible.

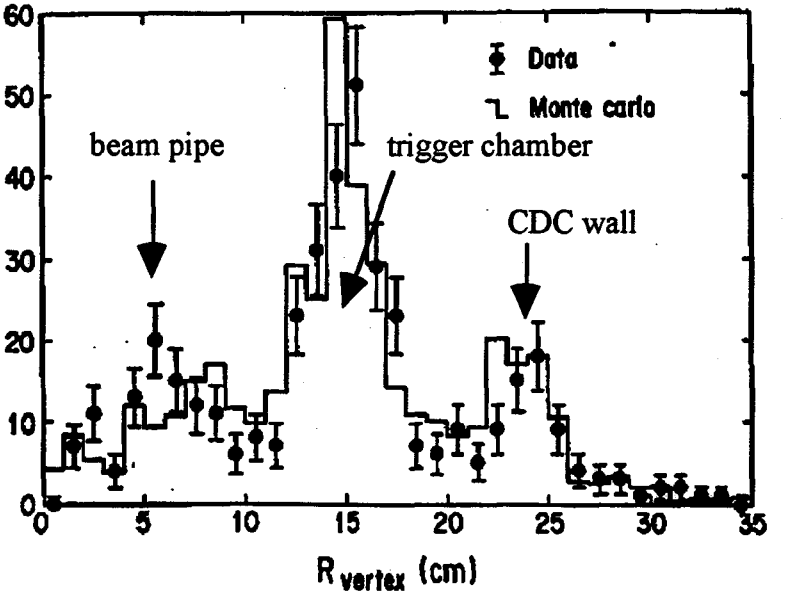

Fig.A3-4 Vertex Distribution of γ-conversion

Vertex distribution of γ-conversion candidates which are selected by the finding algorithm. *Rvertex* is the distance from the interaction point to the conversion vertex. The plots are conversion candidates selected in the real multihadronic events. The histogram is Monte-Carlo prediction using the same selections as for real data. It is normalized with the luminosity. Peaks in the distribution correspond to beam pipe, trigger chamber and CDC inner wall.

References of Appendices

[1] JADE collab., W.Batel et al., Z.Phys. C33(1986)23

[2] D.Tatsumi, VENUS Note.275